



# CHARACTERIZATION OF AGGREGATES FOR SUSTAINABLE FREIGHT TRANSPORTATION INFRASTRUCTURE

University of Wisconsin – Milwaukee  
Paper No. 11-2

National Center for Freight & Infrastructure Research & Education  
College of Engineering  
Department of Civil and Environmental Engineering  
University of Wisconsin, Madison



*Authors:* Hani H. Titi<sup>1</sup>, Andrew Druckrey<sup>1</sup>, and Khalid Alshibli<sup>2</sup>

<sup>1</sup> University of Wisconsin – Milwaukee, Milwaukee, WI

<sup>2</sup> University of Tennessee, Knoxville, TN

*Principal Investigator:* Alan J. Horowitz

Professor, Civil Engineering and Mechanics Department, University of Wisconsin – Milwaukee

## ABSTRACT

A novel method, X-ray computed tomography, has recently emerged as a powerful, non-destructive methodology for material characterization, including geomaterials. This method produces 3D images of the object that can be analyzed in various ways based on the purpose of the scan. The objective of this research is to use X-ray CT technology to investigate the internal structure and porosity of various types of aggregates such as limestone, granite, and quartzite. In addition, this research used X-ray CT technology to investigate the influence of harsh environments such as freezing and thawing on the durability of the aggregate. Virgin and treated aggregate specimens were subjected to X-ray CT to obtain high-resolution 3D images. Aggregate treatments (wetting/drying and freeze-thaw cycles) were conducted using the sodium sulfate soundness test and the actual free-thaw test. The CT scans were carried out using a sector 13-BMD synchrotron microtomography beamline at the Advanced Photon Source of the Argonne National Laboratory, Illinois. Analysis was conducted on the acquired 3D high-resolution images to investigate the pore structure and micro-cracks of these aggregates types. The X-ray CT technology was useful for visualizing the internal structure of aggregate particles with high resolution. This visual inspection provided information on pore space characteristics such as pore shape, connectivity, and distribution. In addition, volumetric quantities such as the volume of aggregate particles and the volume of pore space were identified and measured. These measured quantities were used to calculate porosities of the investigated aggregates, which provided properties of these aggregates using the constructed 3D CT images (non-conventional method). Sodium sulfate soundness test effects on the treated aggregates (degradation, disintegration, and weathering) were significant, as observed in

the 3D CT images of treated aggregate particles. Pore space volume increased as the aggregate particles were treated with wetting/drying cycles of sodium sulfate solution. The sodium sulfate soundness test significantly affected the permeable (connected) pore space and induced degradation/disintegration, which increased the volume of connected pore space with the increase of the number of wetting/drying test cycles. Isolated pore space remained unchanged with the number of sodium sulfate test cycles, since the salt could not penetrate these pores to induce internal force of expansion, which degraded and disintegrated the aggregate structure. The freeze-thaw test induced changes to the pore space of the treated aggregates with a noticeable impact on the connected pore space of the aggregate particle.

## ACKNOWLEDGEMENTS

This research was partly funded by the National Center for Freight and Infrastructure Research (CFIRE). The financial support of CFIRE is appreciated as it was instrumental to the successful accomplishment of the research goals.

Portions of this work were performed at GeoSoilEnviroCARS (Sector 13), Advanced Photon Source (APS), Argonne National Laboratory. GeoSoilEnviroCARS is supported by the National Science Foundation - Earth Sciences (EAR-0622171) and Department of Energy - Geosciences (DE-FG02-94ER14466). Use of the Advanced Photon Source was supported by the U. S. Department of Energy, Office of Science, Office of Basic Energy Sciences, under Contract No. DE-AC02-06CH11357.

The authors would like to acknowledge Dr. Mark Rivers, University of Chicago and GSECARS, for the help, support, and guidance during sample scanning and image gathering and reconstruction at APS.

The authors appreciate the help of Dr. Habib Tabatabai and Dr. Rani El-Hajjar for their comments and suggestions on the research subject and final report.

The help of Mr. Dan Ried, Wisconsin Department of Transportation for providing the rock from the Dane County quarry is greatly appreciated.

Thanks to Dr. Alan Horowitz, UWM and for providing a portion of the funding to purchase the tools necessary to complete this research. The Graduate School and College of Engineering at UWM funded in part the tools necessary to analyze the data.

The research team would like to acknowledge former and current UWM graduate students Ryan English and Emil Bautista for their effort and help during sample scanning at APS.

The help and patience of Ms. Michelle M. Schoenecker, Senior Technical Grant Writer at the College of Engineering & Applied Science, UWM in editing the final report is greatly appreciated.

# TABLE OF CONTENTS

1 INTRODUCTION.....	1
1.1 Research Objective.....	2
1.2 Organization of Report.....	3
2 BACKGROUND.....	4
2.1 Three Dimensional X-ray Computed Tomography.....	4
2.1.1 X-ray Production.....	5
2.1.2 X-ray Absorption.....	10
2.1.3 Image Reconstruction.....	14
2.1.4 Post Processing.....	19
2.2 Aggregate Durability.....	21
2.2.1 Sulfate Soundness Test (ASTM C-88 and AASHTO T104).....	22
2.2.2 Unconfined Freezing and Thawing (AASHTO T103).....	23
2.2.3 Classification of Aggregate Durability.....	24
2.3 Characterization of Aggregate Porosity with Computed Tomography.....	26
2.3.1 Comparison of Computed Tomography to Conventional Methods.....	27
2.3.2 Applications of 3D Computed Tomography.....	27
2.3.3 Three Dimensional Visualization.....	31
3 RESEARCH METHODOLOGY.....	33
3.1 Investigated Aggregates.....	33
3.1.1 Aggregate Sources.....	33
3.1.2 Specific Gravity and Absorption Tests.....	34
3.1.3 Rapid Chloride Permeability Test.....	36
3.2 Aggregate Preparation.....	38
3.2.1 Sodium Sulfate Soundness Test.....	38
3.2.2 Rock Coring.....	39
3.2.3 Soundness of Aggregates by Freezing and Thawing.....	39
3.3 Advanced Photon Source.....	41

3.3.1 Major Components of Advanced Photon Source.....	42
3.3.2 Advanced Photon Source Beamline Overview.....	43
3.3.3 Sector 13 at Advanced Photon Source.....	45
3.3.4 Beamline 13-BM-D.....	46
3.3.5 Computed Tomography Procedure.....	48
3.4 Post Processing.....	55
3.4.1 Post Processing Workstation.....	56
3.4.2 Post Processing Steps.....	56
3.4.3 Pore Measurements.....	72
3.4.4 Three Dimensional Visualization.....	74
4 ANALYSES OF RESULTS.....	76
4.1 Goldberg Aggregate – Limestone.....	76
4.2 Pore Size Analysis.....	98
4.3 Ulland Aggregate – Dolomite.....	107
4.4 New Ulm Aggregate – Quartzite.....	110
4.5 Martin Aggregate – Granite.....	119
4.6 Aggregates Subjected to Freeze/Thaw Cycles.....	123
4.7 Kraemer and Larson Aggregates – Limestone.....	132
5 CONCLUSIONS AND RECOMMENDATIONS.....	136
REFERENCES.....	140

## LIST OF FIGURES

Figure	Page
2.1: Types of X-ray beam arrays (Rivers, 2010).....	6
2.2: Synchrotron radiation facility at Advanced Photon Source (Argonne National Laboratory, 2011).....	8
2.3: Schematic of storage ring and beamlines (HASYLAB, 2009).....	9
2.4: Typical beamline components ( <a href="http://ssg.als.lbl.gov/ssgdirectory/aguilar/BL10homepage.html">http://ssg.als.lbl.gov/ssgdirectory/aguilar/BL10homepage.html</a> ).....	10
2.5: Linear attenuation through a homogeneous sample (after Jenkins, 2000).....	10
2.6: Linear attenuation through a non-homogeneous sample (after Hsieh, 2009).....	13
2.7: Effect of number of projection angles on image quality (Rivers, 2010).....	16
2.8: Edge brightness from beam hardening in the current study.....	17
2.9: Ring artifact from defect with detector in the current study.....	18
2.10: Partial volume effect near phase boundary in the current study.....	18
2.11: Histogram of intensities of X-ray image in this study.....	20
2.12: Noisy CT image of concrete sample from Cnuddle et al. (2008).....	28
2.13: Pore throat of aggregate pore that dictates MIP diameter.....	29
2.14: Increase in interior cracking of a concrete specimen with increasing load as visualized with CT (Landis et al., 2007).....	30
2.15: Two different types of pore distribution within an aggregate.....	32
3.1: Pictures of the investigated aggregates used in this study (after Titi et al., 2005)...	35
3.2: Sodium sulfate soundness test setup with aggregates soaking in solution .....	38
3.3: Rock samples and tool used to extract core specimens for CT scanning .....	39
3.4: Freezing and thawing chamber used in this study.....	41

Figure	Page
3.5: Drying oven used in this study to dry aggregates .....	42
3.6: Aerial photograph of Advanced Photon Source ( <a href="http://acaschool.iit.edu/lectures07/Howard_SynchrRad.ppt">acaschool.iit.edu/lectures07/Howard_SynchrRad.ppt</a> ).....	41
3.7: Schematic of the major components of Advanced Photon Source ( <a href="http://acaschool.iit.edu/lectures07/Howard_SynchrRad.ppt">acaschool.iit.edu/lectures07/Howard_SynchrRad.ppt</a> ).....	44
3.8: Photon Energy and Brilliance of Various Sources ( <a href="http://acaschool.iit.edu/lectures07/Howard_SynchrRad.ppt">acaschool.iit.edu/lectures07/Howard_SynchrRad.ppt</a> ).....	46
3.9: Typical Sector at APS (Borland et al., 2010).....	44
3.10: Entrance to experiment hutch 13-BM-D at GSECARS.....	45
3.11: Schematic of Sector 13 Beamlines.....	46
3.12: Schematic of X-ray path in experiment hutch (Kim et al., 2011).....	47
3.13: Sample on Rotation Stage, Scintillator, Mirror and CCD System.....	48
3.14: Aggregate scanning during various trips to APS .....	49
3.15: Computed tomography scan before and after normalization process .....	51
3.16: Example of different stages of data preprocessing for single detector row (Rivers, 2010).....	52
3.17: Image with rotation center off by 1.5 pixels and cupped feature (a) and image with correct rotation center with no distortion (Rivers, 2010).....	53
Figure 3.18: Optimization of rotation center of a slice based on minimal entropy (Rivers, 2010).....	54
3.19: One slice from scan of an aggregate particle with a resolution of 4.24 $\mu\text{m}$ per voxel .....	55
3.20: Post processing tools used in this study.....	57
3.21: Images that are (a) continuous and (b) poorly merged image from incorrect stitching .....	58

Figure	Page
3.22: Gradient magnitude of a cross section displaying boundaries between contrasting phases.....	60
3.23: Scatterplot with selected clusters.....	61
3.24: Histogram illustrating unassigned voxels that lie near phase boundaries.....	61
3.25: Binary image of aggregate material obtained using the watershed thresholding algorithm.....	62
3.26: Image of void space in and around aggregate created by “logical not” command.	63
3.27: Close up of void space near surface of aggregate.....	64
3.28: Lines from binseparate command created to split pores from background.....	64
3.29: Image resulting from border kill command.....	65
3.30: Material with holes from binseparate separation boundaries.....	66
3.31: Aggregate image with all pores filled.....	67
3.32: Image with isolated pores filled and only pores connected to the aggregate particle surface are present.....	68
3.33: Image showing isolated pores obtained by steps described earlier.....	68
3.34: Image displaying all pores of a cross section within an aggregate particle.....	69
3.35: Cross sectional image displaying pores connected to surface of an aggregate particle.....	70
3.36: Isolated pores separated and labeled for quantification.....	71
3.37: Labeled pores that are connected to the aggregate surface .....	71
3.38: Width and length of a pore determined by Avizo Fire ®.....	73
3.39: Measurements results viewer as outputted by Avizo Fire ®.....	73
3.40: 3D rendering from CT scans on aggregate particles that show two different types of pore distribution within an aggregate particle.....	75

Figure	Page
4.1: CT constructed 3D image of the virgin Goldberg aggregate sample.....	78
4.2: Pore space and crack within cross sections of Goldberg virgin aggregate.....	79
4.3: CT constructed 3D image of Goldberg aggregate subjected to one test of sodium sulfate soundness, 3.1% total porosity.....	85
4.4: Crack and angular pores within cross-sections of Goldberg aggregate subjected to one test cycle of sodium sulfate soundness.....	86
4.5: CT constructed 3D image of Goldberg aggregate with two test cycles of sodium sulfate soundness, 2.9% total porosity.....	88
4.6: Cross-sections of Goldberg aggregate with two test cycles of sodium sulfate soundness showing crack through entire sample and angular pores .....	89
4.7: CT constructed 3D image of Goldberg aggregate with three test cycles of sodium sulfate soundness, 3.5% total porosity.....	91
4.8: Cross-sections of Goldberg aggregate specimen with three test cycles of sodium sulfate soundness showing crack throughout entire particle .....	92
4.9: CT constructed 3D image of Goldberg aggregate with four test cycles of sodium sulfate soundness, 12.4% total porosity.....	93
4.10: Cross-sections of Goldberg aggregate with four test cycles of sodium sulfate soundness showing large highly angular pores.....	94
4.11: CT constructed 3D image of Goldberg aggregate with five test cycles of sodium sulfate soundness, 11.4% total porosity.....	96
4.12: Cross-sections of Goldberg aggregate particle subjected to five test cycles of sodium sulfate soundness showing irregularly shaped angular pores.....	97
4.13: Variation of Goldberg aggregate particle porosity with the number of sodium sulfate soundness test cycles and 3D and 2D images of thin solid material between connected pores .....	100
4.14: Cross-sectional tomographs demonstrating the degradation and increase in pore space near the surface of the aggregate due to wetting/drying test cycles from sodium sulfate soundness test on the same Goldberg aggregate.....	102

Figure	Page
4.15: Cross sectional tomographs demonstrating the increase in pore space intensity and volume due to wetting/drying test cycles from sodium sulfate soundness test on Goldberg aggregates.....	103
4.16: The variation of pore size distribution with the number of wetting/drying cycles from sodium sulfate soundness tests on the same Goldberg aggregate particle.....	105
4.17: The variation of pore size distribution with the number of wetting/drying cycles from sodium sulfate soundness tests on different Goldberg aggregate particle.....	106
4.18: The variation of pore size distribution with the number of wetting/drying cycles from sodium sulfate soundness tests on different Goldberg aggregate particle using pore width measured from 3D CT images.....	107
4.19: CT constructed 3D image of virgin Ulland aggregate, 2.6% total porosity.....	108
4.20: Cross-sections of Ulland virgin aggregate showing small rounded pores.....	109
4.21: CT constructed 3D image of Ulland aggregate with four test cycles of sodium sulfate soundness, 0.7% total porosity.....	111
4.22: Cross-sections of Ulland aggregate particle subjected to four test cycles of sodium sulfate soundness showing cracks within aggregate solid.....	112
4.23: Variation of Ulland aggregate particle porosity with the number of sodium sulfate soundness test cycles on the same aggregate particle.....	113
4.24: CT constructed 3D image of virgin New Ulm aggregate, 3.6% total porosity.....	114
4.25: Cross-sections of New Ulm virgin aggregate particle showing cemented and uncemented grain boundaries.....	115
4.26: CT constructed 3D image of New Ulm aggregate with four test cycles of sodium sulfate soundness, 6.3% total porosity.....	116
4.27: Cross-sections of New Ulm aggregate subjected to four test cycles of sodium sulfate displaying grain boundaries that are not cemented.....	117
4.28: Variation of New Ulm aggregate particle porosity with the number of sodium sulfate soundness test cycles.....	118

Figure	Page
4.29: CT constructed 3D image of Martin virgin aggregate, 1.0% total porosity.....	119
4.30: Cross-sections of Martin virgin aggregate particle showing crack.....	120
4.31: CT constructed 3D image of Martin aggregate with two test cycles of sodium sulfate soundness on the same sample, 3.6% total porosity.....	121
4.32: Cross-sections in Martin aggregate with two cycles of sodium sulfate soundness test showing thin layer of solid over pores connected to the surface of the aggregate....	122
4.33: Variation of Martin aggregate particle porosity with the number of sodium sulfate soundness test cycles.....	123
4.34: Cross-sections of Dane County limestone with 45 freeze/thaw cycles and five test cycles of sodium sulfate soundness.....	124
4.35: Cross-sections of Michigan (light) limestone with 45 freeze/thaw cycles and five test cycles of sodium sulfate soundness.....	125
4.36: Cross-sections of Michigan (dark) limestone with 45 freeze/thaw cycles and five test cycles of sodium sulfate soundness.....	126
4.37: Variation of Dane County limestone aggregate particle porosity with the number of sodium sulfate soundness and unconfined freeze thaw test cycles.....	127
4.38: Comparison of sodium sulfate soundness with unconfined freezing and thawing..	131
4.39: CT constructed 3D image of Kraemer virgin aggregate, 3.6% total porosity.....	132
4.40: CT constructed 3D image of Kraemer aggregate with five cycles of sodium sulfate soundness, 11.5% total porosity.....	133
4.41: Variation of Kraemer aggregate particle porosity with the number of sodium sulfate soundness and unconfined freeze thaw test cycles .....	134
4.42: Variation of Larson aggregate particle porosity with the number of sodium sulfate soundness and unconfined freeze thaw test cycles .....	135

## LIST OF TABLES

Table	Page
3.1: General description of the aggregates used in this study.....	34
3.2: Specific gravity and absorption calculation of different aggregate samples.....	36
3.3: Results of RCPT conducted on concrete specimens at different ages.....	37
4.1: Investigate aggregate property volumes and porosities.....	82
4.2: Volumes and porosities of Goldberg aggregates.....	99

## **Chapter 1**

### **Introduction**

Aggregates are significant components of roadway base courses, asphalt concrete pavements, Portland cement concrete pavements, and bridge/culvert structures. As such, the quality of aggregates has a tremendous influence on the performance and durability of roadways and bridges; therefore, it is important to characterize that the quality of aggregates used in construction. Tests are typically performed to characterize aggregates using the physical parameters of gradation, resistance to abrasion, and resistance to weathering (durability), which are considered conventional methods. The use of conventional methods, such as the sodium sulfate soundness test (AASHTO T104), may not accurately determine aggregate durability.

Rapid and accurate characterization of aggregates is vital to sustaining a safe and functioning transportation infrastructure. For example, transportation infrastructure components, such as reinforced concrete bridge structures, are subjected to harsh environments, and, as a result, susceptible to early deterioration. In regions where deicing salts are applied to the road surface during winter, corrosion of reinforcing steel is mainly attributed to the presence of chloride ions derived from salts. Chloride ions penetrate the concrete, which leads to the corrosion of reinforcing steel, and concrete cracking and spalling. Subsequently, this leads to loss of serviceability and reduces the strength and safety of transportation structures.

A novel method, X-ray Computed Tomography (CT), has recently emerged as a powerful, non-destructive methodology for material characterization, including

geomaterials. In this method, an object is scanned by directing an incident X-ray beam towards the object. The X-ray that passes through the object is collected with an array of detectors. The object is rotated such that the X-ray beam probes from several angles to collect attenuation data and produce the equivalent of a cross-sectional “slice” through the region of interest. This method produces three-dimensional (3D) images (rendering) of the object that can be analyzed in various ways based on the purpose of the scan. Chapter 2 presents some applications of the X-ray CT in material characterization.

### **1.1 Research Objective**

The objective of this research is to use X-ray CT technology to investigate the internal structure and porosity of various types of aggregates such as limestone, granite, and quartzite. In addition, this research will use X-ray CT technology to investigate the influence of harsh environments such as freezing and thawing on the durability of the aggregate. To achieve the research objectives, the following plan was executed:

Virgin and treated aggregate specimens were subjected to X-ray CT to obtain high-resolution 3D images. Aggregate treatments (wetting/drying and freeze-thaw cycles) were conducted using the sodium sulfate soundness test and the actual free-thaw test to simulate the impact of the environment on the aggregate durability. The CT scans were carried out using a sector 13-BMD synchrotron microtomography beamline at the Advanced Photon Source of the Argonne National Laboratory, Illinois. Analysis was conducted on the acquired 3D high-resolution images to investigate the pore structure and micro-cracks of these aggregates types. Aggregate durability and strength is greatly

influenced by size, distribution, and connectivity of pore spaces within aggregate particles. Quantitative analysis was conducted on these images to identify parameters pertaining to aggregate durability.

## **1.2 Organization of Report**

This report is organized in five Chapters. Chapter 1 introduces the research motivation and objectives. Background information on the aggregate durability methods and the X-ray and computed tomography are presented in Chapter 2. Chapter 3 discusses the research methodology in which aggregate samples were prepared and tested, and the methods of CT image analysis. Chapter 4 presents the results of the research with detailed analysis and evaluation. Conclusions and recommendations are presented in Chapter 5.

## **Chapter 2**

### **Background**

This chapter presents background information on synchrotron radiation and the 3D X-ray computed tomography (CT) process. Aggregate durability and test methods used to characterize aggregate durability are presented in the context of resistance to freeze-thaw effects. Lastly, this Chapter discusses applications of X-ray computed tomography to characterize geomaterials and other materials.

#### **2.1 Three-Dimensional X-ray Computed Tomography**

X-ray CT is a non-destructive technique for visualizing and quantifying the internal features of objects. An object is scanned with an X-ray, and volumetric pixels (voxels) are detected and created through a series of image reconstruction algorithms. The images can then be further explored with 3D visualization, analysis, and modeling software.

Image acquisition begins with a source of energy, in which portions of that energy absorb into, bounce off, or penetrate through an object, and some of that energy is detected by a scintillator and camera or other detecting system. The most frequent sources used are within the electromagnetic spectrum. The most well-known type of imaging is within visible wavelengths (photographs), but objects can also be imaged internally with ultraviolet rays, X-rays and Gamma rays. X-rays have been used in the medical field since the early 1970s and are recently becoming a breakthrough in material imaging, including non-destructive imaging of geomaterials.

### **2.1.1 X-ray Production**

Characteristic X-rays are produced from the excitation of atoms by high acceleration (or deceleration). The excitation can be based on electrons, X-rays, Gamma rays, protons, or synchrotron radiation. The particles are often charged using an X-ray vacuum tube with a cathode to produce electrons and an anode to collect electrons, which creates a flow of electrical current. The flow is created by connecting high voltage to the tube to excite the electrons. Some X-rays are produced when particles are accelerated to a high energy and bombard a material (usually a metal such as Tungston). The excited atoms emit characteristic X-rays by creating instability within the atom from electrons in the metal moving from outer shells to inner shells. The energy difference between the initial state and final state after stability is regained and is given off as an X-ray photon.

There are several different X-ray beam arrays that can be used to image the interior of objects:

1) pencil beam (Figure 2.1a), which images a single point; 2) fan beam (Figure 2.1b), which images and magnifies a tiny cross-section of the object; 3) parallel beam (Figure 2.1c), which proportionally images a thicker cross-section of an object; and 4) cone beam (Figure 2.1d), which magnifies a section of an object. Parallel and cone beams are more desirable for volume CT because a larger portion of an object can be scanned in a relatively short amount of time; however, parallel and cone beams require a greater amount of intensity from the source of radiation. Electromagnetic radiation (including X-rays) from synchrotron radiation is produced by charged particles accelerating radially. Margaritondo (1988) stated that “Synchrotron radiation is the electromagnetic radiation

emitted by electrons or positrons moving at relativistic velocities along a curved trajectory with a large radius of curvature.”

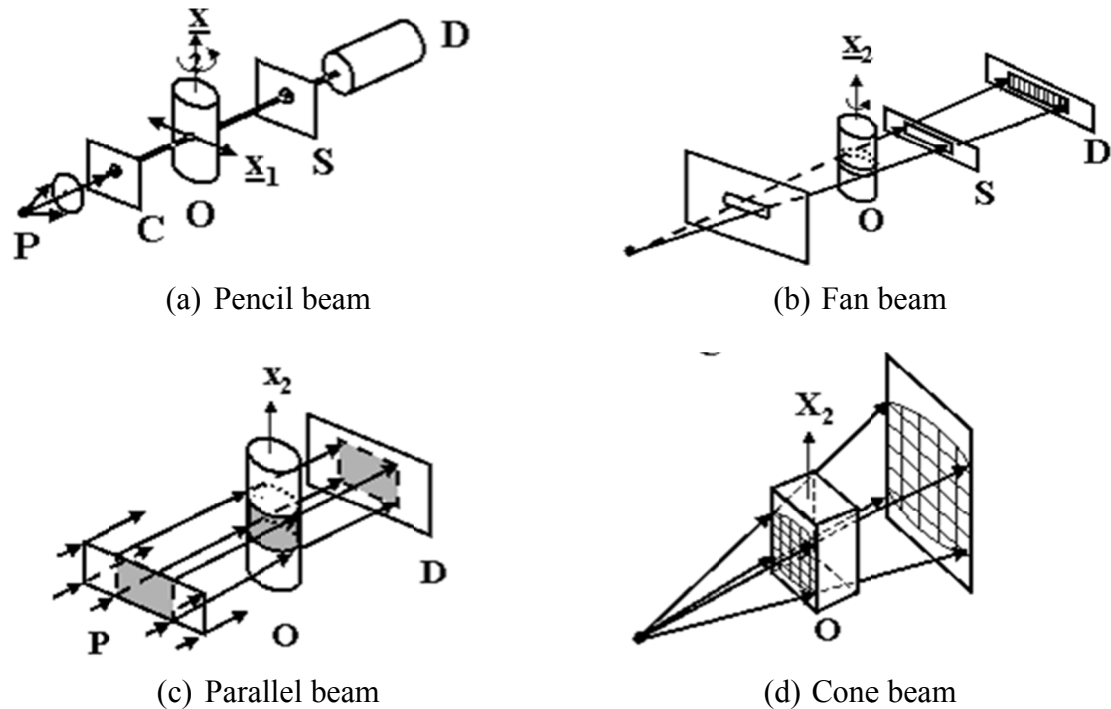


**Figure 2.1: Types of X-ray beam arrays (Rivers, 2010)**

A synchrotron is a circular cyclic particle accelerator that synchronizes the magnetic and electric fields to accelerate the particles and is the most powerful non-destructive scanning technique that can produce a high-resolution 3D of scanned objects (Alshibli and Hasan, 2010). When charged particles (usually electrons in synchrotron use) are moving near the speed of light in a curved path they emit a broad array of radiation, ranging from microwaves to Gamma-rays. This radiation can be used for a variety of types of testing, including using the X-ray photons for computed tomography. Current high-intensity, “third-generation” synchrotron facilities, which are fully dedicated for

synchrotron radiation, are making experiments such as computed tomography quick and easy (Baruchel et al., 2002). The flux and brilliance, both based on a measure of photons per second, are maximized to provide the most out of the facility. Flux is the measure of photons per second in a narrow bandwidth, and brilliance is a measure of the intensity and directionality of an X-ray beam (Advanced Photon Source, 2011). Third-generation synchrotron radiation produces enough intensity to use parallel and cone X-ray beams for tomography, which can be wide enough to cover entire samples.

Synchrotron facilities consist of several components, including an injection system, a storage ring, and beamlines. The injection system generates, accelerates, and injects electrons into the storage ring. Electrons are usually generated with an anode and heated cathode, and then accelerated. The preliminary acceleration is achieved with a linear accelerator (LINAC) that injects the electrons into a booster synchrotron, which uses a series of electromagnets and a radio frequency system that are synchronized to further accelerate the electron to very near the speed of light. The electrons are then injected into the vacuum system of the storage ring where they are circulated by dipole bending magnets and other magnets. Figure 2.2 illustrates an overview of the components involved in the synchrotron radiation process.

Modern storage rings consist of several straight sections connected by bending magnets. The straight sections allow for insertion devices to be added to the storage ring to produce radiation with different properties than with bending magnets that can be used for different applications. Figure 2.3 presents a schematic of a storage ring with bending magnets and insertion devices. The bending magnet is located on the curve of the storage ring and the insertion devices are located on straight sections. The radio frequency system

supplies power to keep the particles in motion. Bending magnets provide a wide spectral range of radiation with high intensity, which allows users to select the appropriate X-ray energy for their experiment. As the radiation exits the storage ring via bending magnet or insertion device, it enters a beamline, at the end of which experiments are conducted.

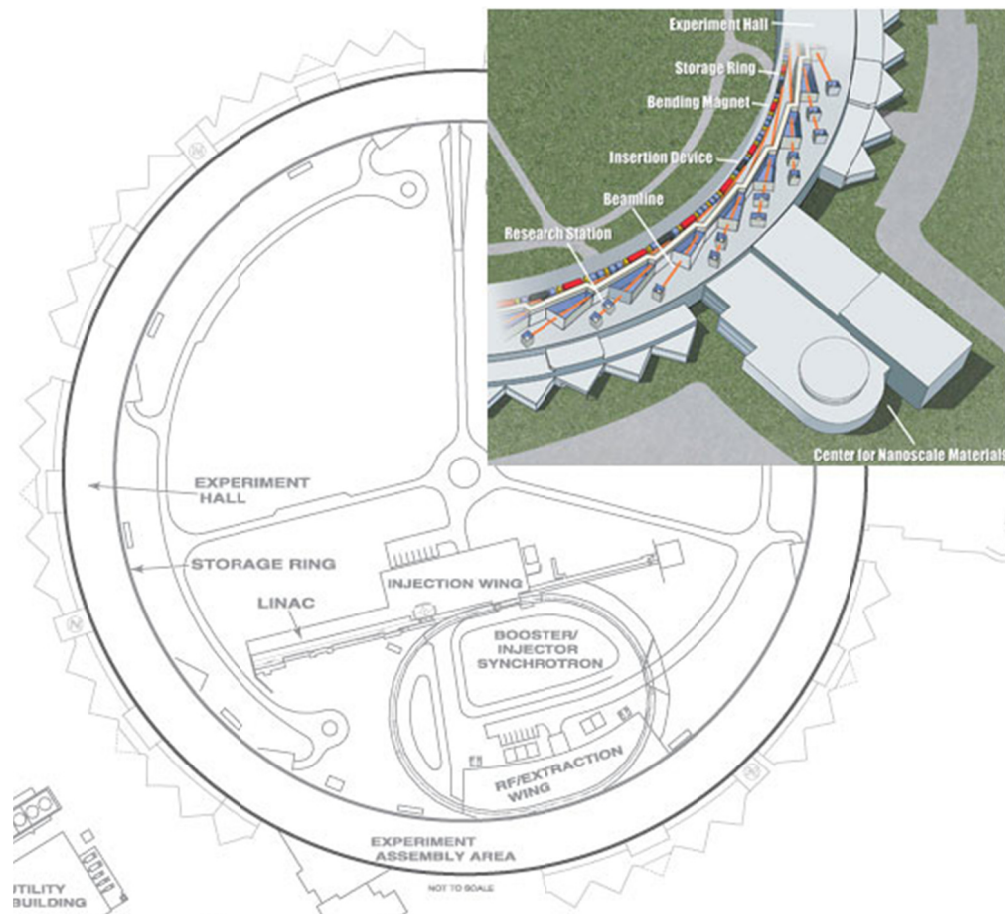
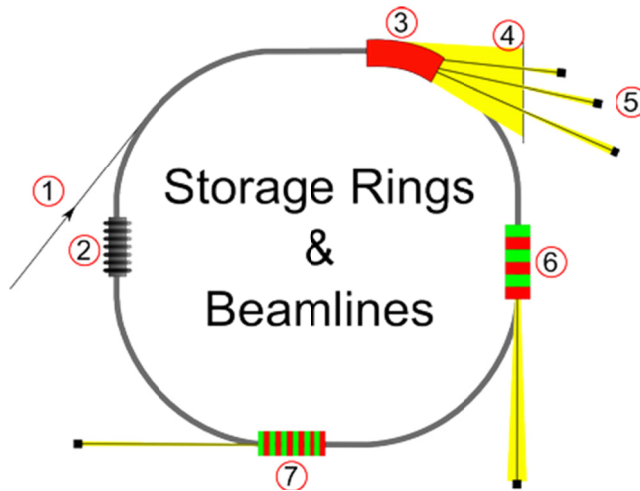


**Figure 2.2: Synchrotron radiation facility at Advanced Photon Source (Argonne National Laboratory, 2011)**



m

**Figure 2.3: Schematic of storage ring and beamlines (HASYLAB, 2009)**

The major components of a beamline include a monochromator, vacuum system, mirrors, control system, experimental chamber, and other miscellaneous items (Margaritondo, 1988). One or more monochromators filter out beam energies that are not needed for an experiment and allow only a small range of energies to pass through. For example, all radiation can be filtered except for a narrow portion of hard X-rays, which have enough energy to penetrate solids and allow imaging. The exact energy level needed for an experiment depends on the sample material. Optimizing the energy level based on that sample provides the best resolution.

The mirrors along a beamline can perform a variety of functions. Mirrors are used to focus the radiation to concentrate its intensity into a small area, such as to the size of the monochromator and produce a parallel beam array. Mirrors can also be used to split the radiation to two or more beamlines, magnify or de-magnify the source, or change the source polarization. Figure 2.4 displays a setup for some typical beamline components. Mirrors are used in the setup of Figure 2.4 to focus, condense and deflect the beam.

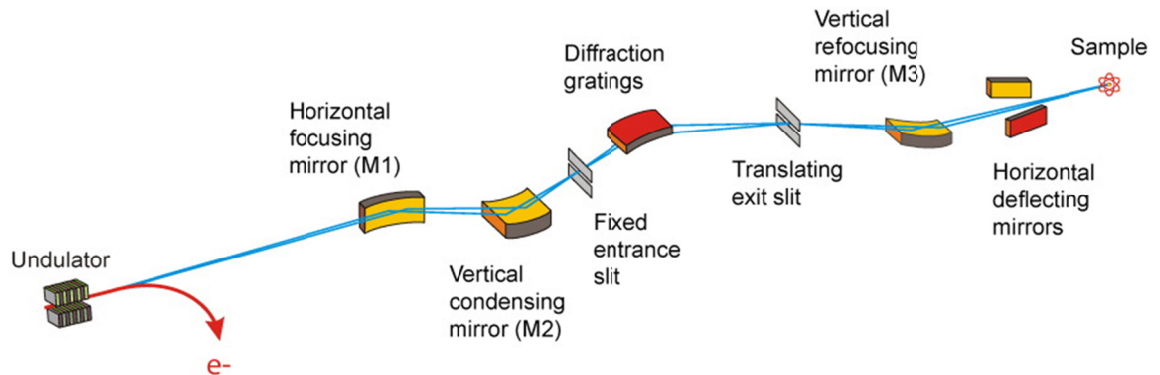


**Figure 2.4: Typical beamline components**  
 (<http://ssg.als.lbl.gov/ssgdirectory/aguilar/BL10homepage.html>)

Beamlines are also fitted with an imaging system that could include a scintillator to convert radiation to visible light, and a detection system, including a charged-coupled device (CCD) camera, to image the light after passing the scintillator and produce gray scale image of energy passing the object.

### 2.1.2 X-ray Absorption

In the energy range commonly used for CT, X-rays mostly interact with matter in three ways: the photoelectric effect, the Compton Effect (incoherent scatter), and coherent scattering, as depicted in Figure 2.5.

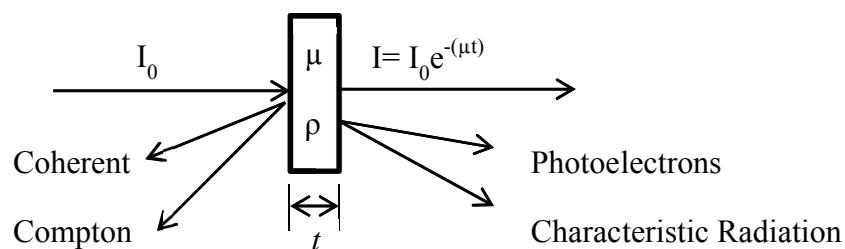


**Figure 2.5: Linear attenuation through a homogeneous sample (Jenkins, 2000)**

The photoelectric effect involves a high energy X-ray photon that gives up all of its energy to release an electron from an interior shell of an atom. The free electron, known as a photoelectron, is emitted. The void from the photoelectron is filled by an outer-shell electron that has more energy than the interior electron that it replaced. This energy difference results in the emission of characteristic radiation. Atoms with higher atomic numbers take more energy to release the electrons. In addition, the probability of photoelectric interaction is proportional to the cube of the atomic number ( $Z$ ) (Hsieh, 2009).

The second interaction, the Compton Effect, involves a photon partially transferring energy to an electron with significantly less energy than the incident photon. The electron is freed and the incident X-ray photon is deflected with some loss of its initial energy, and has a higher wavelength. The deflected photon can be either backscattered (a deflection  $>90^\circ$ , usually low-energy photons) or forward-scattered (a deflection  $<90^\circ$ , usually high-energy photons). Compton scattering occurs throughout the entire sample and depends on the electron density of the material, not on the atomic number.

The third interaction of coherent scatter is simply the deflection of the X-ray photon with no loss of energy. X-ray diffraction is a form of coherent scatter. The incident beam with intensity  $I_0$  is attenuated by the sample and then enters the imaging system as a weakened beam with intensity  $I$ . The ratio of the intensity of the weakened beam and incident beam ( $I/I_0$ ) is related to the attenuation coefficient, density, and thickness of the sample by a form of the Beer-Lambert Law:

$$I = I_0 e^{-(\mu t)} \quad (2.1)$$

where  $\mu$  is the attenuation coefficient and  $t$  is the thickness of the sample. The attenuation coefficient is a function of the atomic number of the elements within the material, the energy of the incoming X-ray beam and density of the sample. Elements with a high atomic number will absorb more energy than elements with a low atomic number, and denser materials will have more atoms to absorb the photons. The interaction of an X-ray beam with a homogeneous sample of thickness  $t$ , density  $\rho$  and attenuation coefficient  $\mu$  is represented by Figure 2.5.

However, samples are usually not homogeneous throughout the entire thickness, such as a material that consists of air and solids made up of different elements. The internal structure of a material will be relatively homogeneous over a very short thickness  $t$ . Every tiny thickness will have a relatively homogeneous attenuation coefficient and add to the attenuation of the beam, as visualized in Figure 2.6. This complication is corrected with CT reconstruction algorithms; however, these algorithms cannot take into account the polychromatic nature of X-ray beams. Even though the monochromators filter out most of the unwanted energies, there is still a range of energies around the one that is desired. Lower-energy X-rays are absorbed easier than the higher-energy photons, which leads to beam hardening and the occurrence of artifacts.

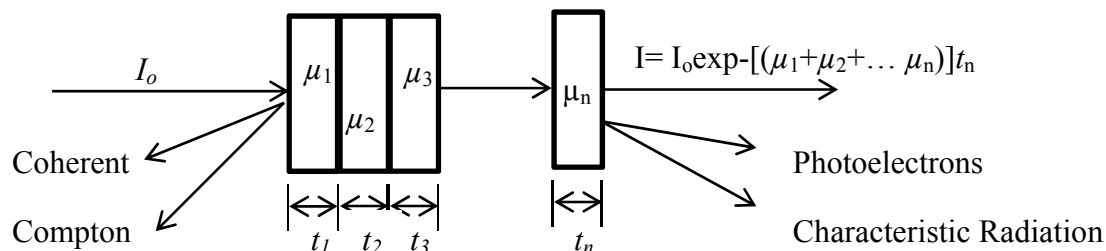


**Figure 2.6: Linear attenuation through a non-homogeneous sample (after Hsieh, 2009)**

After the X-rays pass through a sample they are directed into a detector system. The detector system converts the X-ray photon intensity into an electrical impulse by means of a scintillating material. Detection systems influence the image quality and resolution as well as the efficiency of data collection. Scintillator efficiency depends on the energies of photons that are being detected. High-energy photons pass through materials easier than low-energy photons, which must be considered when processing the images. Also, the size of a detector determines the spatial amount of the energy that is averaged into a single pixel, and the number of detectors determines how fast the data can be collected. To obtain a complete image, detectors are aligned in a grid pattern. A very large number of very small detectors is optimal for higher image resolution, but the cost of processing time increases as the resolution increases. Calibrations are also needed to correct for any discrepancies in the detectors themselves or between the X-rays and detectors. This calibration could be completed in a variety of ways depending on the system. A common calibration method takes scans with no X-ray beam and scans with the X-ray on with no sample in front of it, and normalizes the data with these scans.

A single intensity detection of an object is not enough to view the internal structure; however, as a sample rotates, many views of the object can be obtained at multiple angles. As the number of angles at which views are taken increases, the quality of the image and image acquisition time increases. A balance of projection angles and time should be determined based on the importance of the quality desired. Volume CT usually requires a larger number of projection angles. The sample should be scanned over 180 degrees for complete coverage, and the number of angles scanned determines the quality. If there are large steps in the angle, the resulting image will be noisy. Figure 2.7 illustrates the effect of the number of angle projections on the quality of an image. Figure 2.7 (a) presents 45 projections of the X-ray scan to reconstruct an image that contains heavy noise lines throughout the image. When the number of projections is increased to 90 the reconstructed image contains less noise, as depicted in Figure 2.7 (b). Figure 2.7 (c) is a CT constructed image with 360 projections and displays little noise around the sample; Figure 2.7 (d) presents a clear CT reconstruction of the same image using 720 projections. The drawback of increasing the number of projections is an increase in the amount of time needed for a full scan.

### **2.1.3 Image Reconstruction**

Image reconstruction consists of using mathematical algorithms on image sinograms to create 2-dimensional tomographs for each detector row. The most popular method is the filtered back-projection algorithm (Ketcham and Carlson, 2001 and Hsieh, 2010), in which the data is filtered with a given filter and then backprojected using Fourier transforms. Each scan at each angle is superimposed onto a grid. Each point on the grid, which corresponds to a pixel, is designated a CT number based on the overall intensity of

the pixel. How the points are assigned CT numbers depends on the system being used. Medical systems and some other systems use the Hounsfield Unit to allocate a value to the pixel by relating the attenuation coefficient of the pixel to water and air as follows:

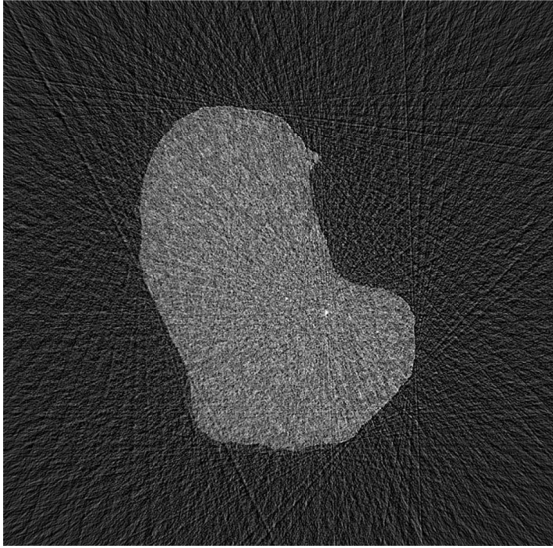
$$\text{HU} = 1000 \frac{(\mu - \mu_w)}{(\mu_w - \mu_a)} \quad (2.2)$$

where HU is the Hounsfield Unit number given to each pixel based on the absorbing material's attenuation coefficient  $\mu$ , the attenuation coefficient of water  $\mu_w$ , and the attenuation coefficient of air  $\mu_a$  (Taina et al., 2007).

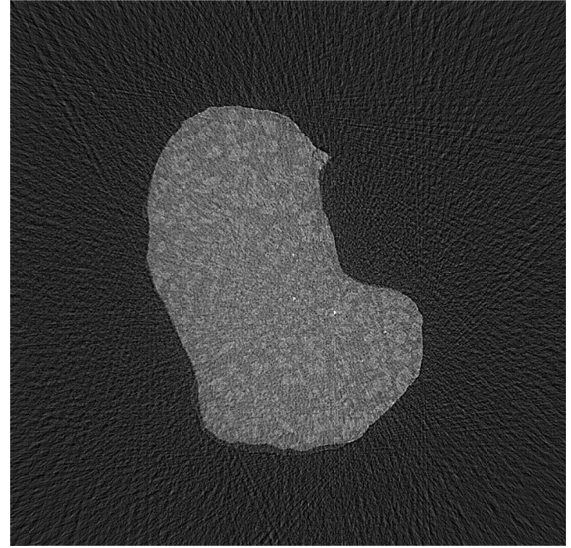
Linking to a reference materials like water and air works well in the medical field, but trying to link objects that vary in chemical makeup to a reference, such as geomaterials, is counterproductive (Ketcham and Carlson, 2001). CT systems used to image objects that are chemically variable usually use a scale based on the individual object. Another step in the reconstruction is the centering of the rotation axis. When the object is placed on the rotation stage it is usually not centered perfectly along all axes; therefore, measures must be taken to optimize image centers to prevent artifacts.

Some problems found in images from CT scans include artifacts and partial volume effects. Common artifacts include beam hardening artifacts, long-axis lines, and ring artifacts. Beam hardening artifacts cause the edge of objects to be brighter than the center, as illustrated in Figure 2.8. Edge illumination from beam hardening occurs because lower-energy X-rays are absorbed easier than higher-energy X-rays. Beam hardening occurs near the edges of the sample because strong X-rays lose very little intensity at the edge, while the softer X-rays are easily absorbed. Beam hardening can be

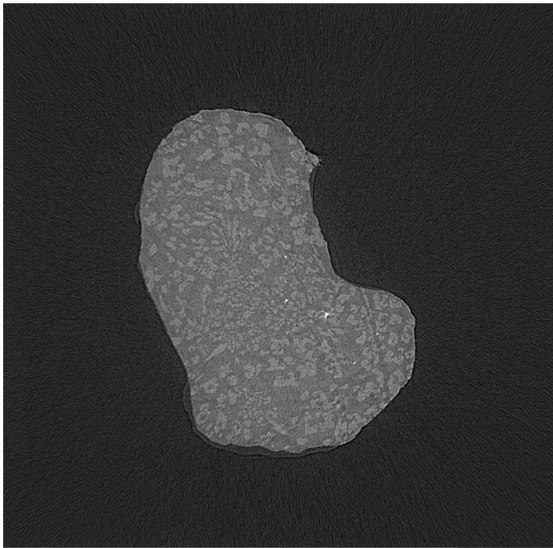
reduced by using higher-energy X-rays that are pre-hardened and with hardening correction algorithms during reconstruction.



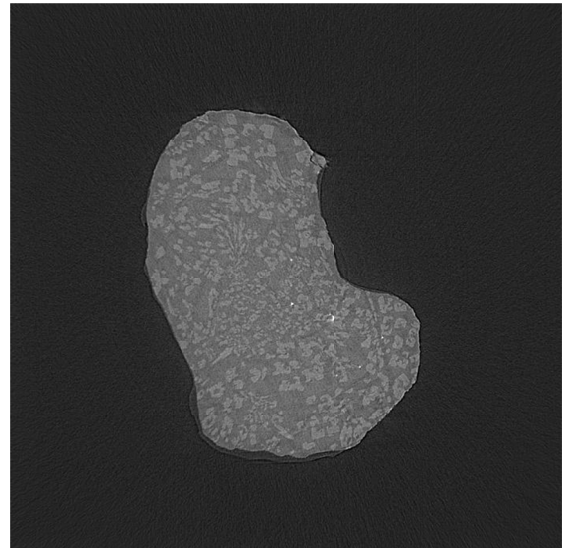
(a) 45 Projections (4 degree steps)



(b) 90 Projections (2 degree steps)



(c) 360 Projections (0.5 degree steps)



(d) 720 Projections (0.25 degree steps)

**Figure 2.7: Effect of number of projection angles on image quality (Rivers, 2010)**

Long-axis lines are artifacts that occur in objects that are largely non-circular. Long-axis lines appear as streaks through an object that parallel the long axis. Artifacts can also result from a slight shift in some of the detectors. Over a single view, a detector shift will show as a streak in the image; over several views, the result will be a ring artifact. Figure 2.9 displays a ring artifact in one slice of an image. Ring artifacts only occur for a few slices, depending on the severity of the detector shift.

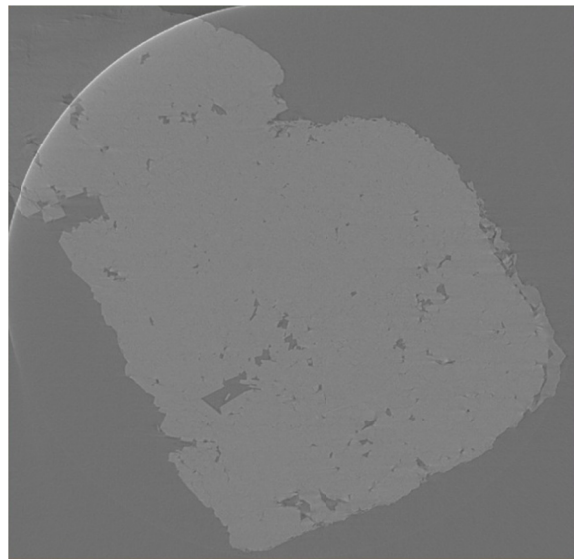


**Figure 2.8: Edge brightness from beam hardening in the current study**

Partial volume effects occur near the boundaries of a region of attenuation (such as solid phase and void phase) that is blurry because of the averaging of pixels in this area during reconstruction. Figure 2.10 shows an example of partial volume effect at a boundary between a pore and solid within an aggregate.

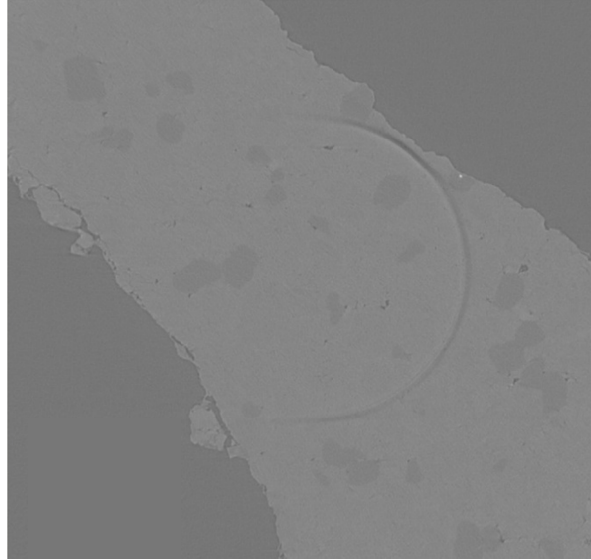


**Figure 2.9: Ring artifact from defect with detector in the current study**

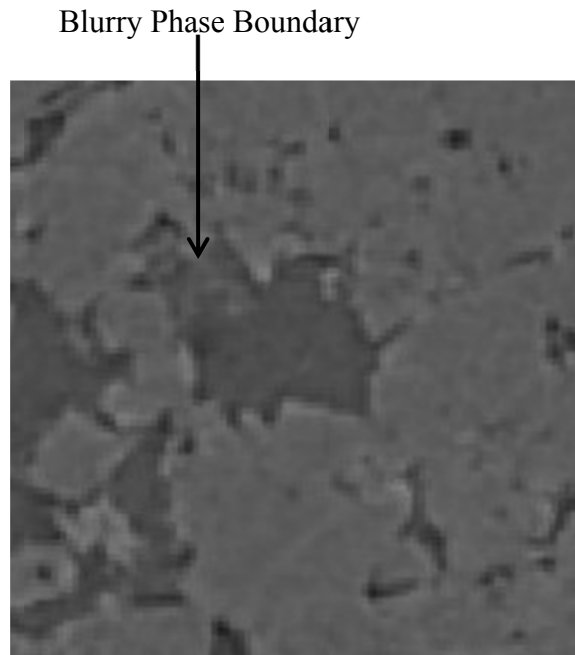


**Figure 2.10: Partial volume effect near phase boundary in the current study**

These effects are minimized when there is a significant difference in the attenuation between the two phases. In this case, the resulting boundary can be accurately determined with post-processing techniques.

#### **2.1.4 Post Processing**

The grey-scale images obtained from CT are useful for visual analysis of each cross-section of an object; however, further analysis, such as 3D visualization and quantification, requires extensive post-processing of the images. The basic steps include image filtering, segmentation, quantification, and visualization. The computed tomography image consists of a grid of pixels based on the attenuation of each pixel space, which includes noise and artifacts. Noise and artifacts may occur within one phase of one material or at boundaries of phases between two materials. Image filtering techniques were developed to correct these deficiencies and are applied during pre-processing and post-processing of images. There are different types of filters for various applications depending on the result desired. For example, Gaussian smoothing filters can correct noise by changing a pixel's intensity based on a weighted average of surrounding pixels—the result is a smooth image with less noise than the original.

Image segmentation is the process of creating a binary image from a grey-scale image in order to distinguish between different phases within a material. The simplest method is global thresholding, a process that includes identifying and selecting a threshold value between the CT numbers for each phase. A histogram of pixel intensity of an image, as shown in Figure 2.11, has peaks corresponding with each phase within the scan. For example, a material consisting of two phases such as an air phase and solid material

phase (with the material being relatively homogeneous) will exhibit two peaks, as shown in Figure 2.11.

Global thresholding consists of choosing a single value at the minimum between the peaks of the histogram as the phase boundary. Voxels above that value are classified as solid phase, and voxels below that value are classified as air phase. This technique ignores the phase boundary problem and often misidentifies phase voxels close to boundaries if the image is noisy and has poor resolution.

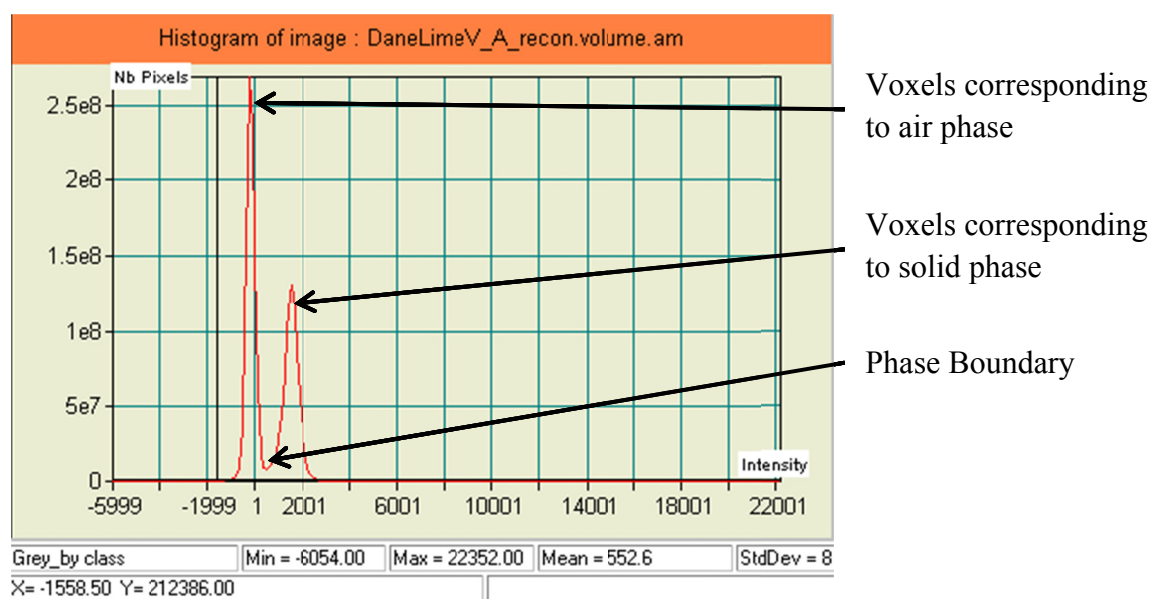


**Figure 2.11: Histogram of intensities of X-ray image in this study**

Other approaches using local thresholding are techniques based on Indicator Kriging and watershed segmentation. Indicator Kriging is a local spatial segmentation method that involves choosing two intensity values. The lower value chosen classifies all voxels with a lower CT number as one material, and the larger value classifies all voxels with a CT

number above that value. Each value lays on its respective side of the phase boundary and leaves a gap of unassigned voxels that could be classified as either material. The voxels between the two values (close to the phase boundary) are assigned to either phase using the maximum likelihood estimate of each phase based on the two-point correlation function (Oh and Lindquist, 1999). The watershed algorithm simulates flooding on the high-gradient areas of an image, which produces a local distinct boundary between two phases of an object. Computer software can then be used to analyze and quantify the properties of air space and solid space and create 3D surfaces of each for visualizing the phases.

## **2.2 Aggregate Durability**

Aggregates are the fundamental building block of transportation infrastructure—they serve as the framework for asphalt concrete, Portland cement concrete pavements, and concrete structures. Aggregates are exposed to physical and chemical degradation forces throughout their life in infrastructure, from extraction, to transportation, to mixing and during their service life. Aggregates must be resistant to the forces they are subjected to throughout their service life. The use of aggregates with poor durability leads to premature distresses such as durability (D) cracking in Portland cement concrete pavements, the most common distress in concrete pavement related to freeze-thaw durability of aggregates (Kevern et al., 2008). Several tests are available for evaluating the quality of aggregates based on absorption, soundness, freezing and thawing, abrasion, and crushing. Some of these tests are related to each other such as absorption, soundness and freeze-thaw tests.

The freezing and thawing of aggregates in cold climates are the most destructive mechanisms for degrading aggregates. Water in the aggregate pores expands when frozen, causing internal stresses. Also, aggregates confined inside asphalt concrete or Portland cement concrete must prevent the extrusion of frozen water into the surrounding cement paste with enough pressure to break the bond (Williamson et al., 2005).

The durability of aggregates is characterized into two categories: durability against aggregate abrasion, and durability against weathering agents. LA Abrasion, micro-deval, aggregate impact value, and aggregate crushing value test the durability of aggregates to resist abrasion. Sulfate soundness and soundness by freezing and thawing are used to characterize durability against weathering agents such as freezing and thawing.

### **2.2.1 Sulfate Soundness Test (ASTM C-88 and AASHTO T104)**

The sulfate soundness test (ASTM C-88 and AASHTO T104) is used to estimate an aggregate's resistance to the weathering processes. Samples of aggregate are placed in a saturated solution of sodium sulfate and then dried in an oven. The salt solution penetrates into the aggregates' permeable pores and upon drying the salt recrystallizes, which produces internal forces that apply pressures inside the aggregate and simulates the expansion of freezing water. This method, coupled with other aggregate properties, is used to evaluate the ability of an aggregate to perform in the field.

The aggregate gradation is designated from specifications, and a sample of aggregates is first washed, dried, sieved to refusal, and weighed. Saturating and drying the sample of aggregates once is considered one cycle. The recrystallization of the salt causes internal pressures within the pores that the solution entered. The internal pressures cause the

aggregates to form micro cracks and other anomalies within the aggregate, and then the aggregates start to degrade and break up from the process. Five cycles is sufficient to evaluate the durability of the aggregate. After the final wetting/drying cycle, the aggregates are washed and sieved to determine the amount of breakage that occurs from the test cycles. The percentage of weight lost is recorded for each of the specified aggregate sizes, totaled, and then compared with other performance measures to determine if the aggregates are suitable for certain uses.

The sulfate soundness test takes a long time and the precision of this test is quite low. Testing five cycles takes a week or more, and the coefficient of variation is 24% for a single operator and 41% between different laboratories. This test does not determine whether aggregates are durable, it only provides an unreliable basis for rejection. Sulfate soundness is especially unreliable when assessing the durability of recycled concrete for use of an aggregate because the chemical reaction between the sodium sulfate and concrete leads to very high loss of mass (Williamson et al., 2005).

### **2.2.2 Unconfined Freezing and Thawing (AASHTO T103)**

Compared with the sulfate soundness test, a better representation of the freeze-thaw process in the field is the soundness of aggregates by unconfined freezing and thawing (AASHTO T103), which may provide better insight into an aggregate's ability to resist degradation/disintegration from actual freezing and thawing. The test involves three procedures:

- Procedure A: Total immersion – Aggregates are soaked in water for 24 hours before the test begins and then subjected to freeze-thaw cycles while remaining completely immersed in water.
- Procedure B: Partial immersion – Aggregates are saturated in a 0.5% ethyl-alcohol solution in a vacuum with an air pressure that does not exceed 3.4 kPa and left in the solution for 15 minutes. The samples are then frozen in the surface-wet condition until suitably frozen and then thawed in the alcohol solution.
- Procedure C: Partial immersion – This is the same as Procedure B, except water is used in place of the ethyl-alcohol solution.

The aggregates and water or solution are put in a freezing and thawing chamber for up to 50 cycles as designated by local standards. After the freeze-thaw cycles, the aggregates are dried and sieved to determine the loss of mass. This method can more accurately quantify disintegration from physical freezing and thawing than the sulfate soundness test; however, it does not account for environmental factors affecting the aggregates and it takes a significant amount of time to complete.

### **2.2.3 Classification of Aggregate Durability**

The uncertainty and the time intensive nature of these tests warrant new types of testing. Kaneuji (1978) and Williamson et al. (2005), showed that the pore characteristics of coarse aggregates play an important role in the freeze-thaw resistance of aggregates.

Kaneuji (1978) investigated the relationship between coarse aggregate porosity and freeze-thaw durability of concrete made with that aggregate. After finding that many

other researchers concluded the porosity of aggregates affect durability, Kaneuji (1978) used 24-hour soaking and vacuum absorption measurements and pore size distribution measurements through mercury intrusion on 27 different aggregate types, and conducted rapid freezing and thawing tests on concrete made with those aggregates. Kaneuji (1978) calculated a durability factor based on the rapid freezing and thawing tests for each of the investigated specimens and concluded that there was a good correlation among pore volume and median pore diameter and aggregate durability. He quantitatively estimated the expected durability factor of concrete made with certain aggregates as:

$$\text{EDF} = \frac{0.579}{\text{PV}} + 6.12 \times (\text{MD}) + 3.04 \quad (2.3)$$

where:

EDF = expected durability factor,

PV = intruded pore volume of pores  $>45 \text{ \AA}$  ( $\text{\AA} = \text{Angstrom} = 10^{-10} \text{ m}$ ), cc/g, and

MD = median diameter of pores  $>45 \text{ \AA}$ , in  $\mu\text{m}$  as measured by mercury intrusion.

Kaneuji (1978) also compared the expected durability factor with concrete pavements that exhibited durability cracking (D-cracking). Two methods were used: extracting aggregates from the concrete and calculating the EDF, and using information available for the aggregates that were used for the concrete. Based on the age of the concrete and the severity of cracking, Kaneuji concluded that aggregates with an EDF up to 40 were not durable; aggregates with an EDF between 40 and 50 were marginal; and aggregates with an EDF above 50 resulted in a durable aggregate.

The research of Williamson et al. (2005) assessed the Wisconsin Department of Transportation's (WisDOT) durability testing methods and correlated laboratory tests to the field performance of aggregates, and concluded that absorption tests can be used as a preliminary indicator of durability. Williamson et al. (2005) showed that aggregates with vacuum-saturated absorption of less than 2% met the durability requirements of the LA abrasion test, micro-deval test, sodium sulfate soundness test, and unconfined freezing and thawing test. They concluded the sodium sulfate soundness test was able to correctly identify two poor aggregates without rejecting any intermediate or good aggregates. Also, the unconfined freezing and thawing test had no correlation with any other test, and identified only one WisDOT-classified poor aggregate.

### **2.3 Characterization of Aggregate Porosity Using Computed Tomography**

The characterization of aggregate porosity using three-dimensional computed tomography is becoming increasingly popular in the geosciences and material science fields. Pore properties have been historically difficult to visualize and measure, especially the tortuosity and connectivity of the pores. Laboratory tests, such as absorption, cannot give quantitative measures of pore characteristics, and mercury intrusion porosimetry can only give accurate data for cylindrical pores. Other conventional methods used to quantify pore space are gas absorption, scanning electron microscope, and optical microscopy, each of which has drawbacks. Methods using CT were found to accurately quantify the pore space characteristics that are difficult to measure.

### **2.3.1 Comparison of Computed Tomography to Conventional Methods**

A conventional method of measuring pore characteristics with 2D thin section and optical imagery was compared with CT by Elliot and Heck (2007) for void analysis in thin sections of soil samples. This, along with other conventional methods, is initially inefficient because it is destructive to the sample, difficult, and time consuming. CT requires no sample preparation or destruction, which makes it appealing to researchers. Elliot and Heck (2007) compared 2D thin sections and optical imagery of soils with a spatial resolution of 33.9  $\mu\text{m}$  per pixel with CT imagery of the same soil samples at a resolution of 34  $\mu\text{m}$  per pixel. They reported a difference in the voids detected by optical and CT methods, which is attributed to the selected values of thresholding for segmenting the CT images. The histograms of the images in Elliot and Heck's (2007) research did not show distinct peaks of material and void space, which lead to errors. They suggest the accuracy of either method is of further debate and a combined approach is beneficial to analyzing 2D thin sections; however, CT is much more advantageous in 3D analysis. Other researchers have used CT as an alternative to 2D thin sections, such as Birgul (2008), who used X-ray CT to monitor macro voids in ageing mortar.

### **2.3.2 Applications of 3D Computed Tomography**

Three-dimensional CT has been used extensively to determine the porosity of many types of samples including concrete, rocks, and soils. Cnuddle et al. (2008) used 3D CT, mercury intrusion porosimetry (MIP), and water absorption under a vacuum to characterize porosity and the microstructure of building stones and concretes. The acquired CT images with a resolution of 10  $\mu\text{m}$  were fairly noisy, as seen in Figure 2.12.

Features within the image streak and there is no clear boundary between features of the image. The noise is from the quality of CT acquisition and reconstruction used in the research of Cnuddle et al. (2007).

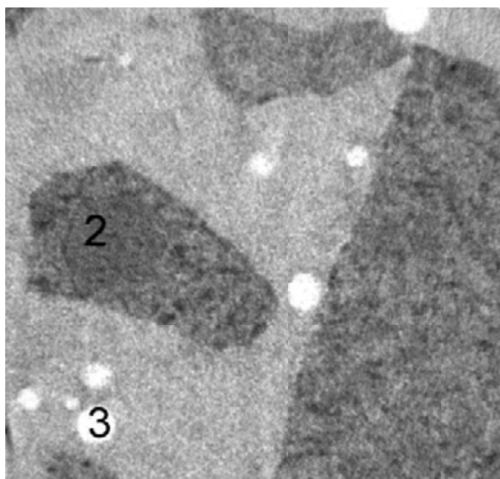


**Figure 2.12: Noisy CT image of concrete sample from Cnuddle et al. (2008)**

Cnuddle et al. (2008) stated that mercury intrusion porosimetry has several drawbacks, including only detecting the diameter of the throat of a pore. For example, a pore that comes to a throat for a short distance and opens into a larger void space has diameter readout from MIP of the throat, as seen in Figure 2.13. Also, MIP pore volume and diameter data can deviate from the actual pore, because MIP assumes straight cylindrical pores. Actual pores located in materials such as rocks or aggregates are a structure of highly tortuous and interconnected pores, as shown in Figure 2.13.

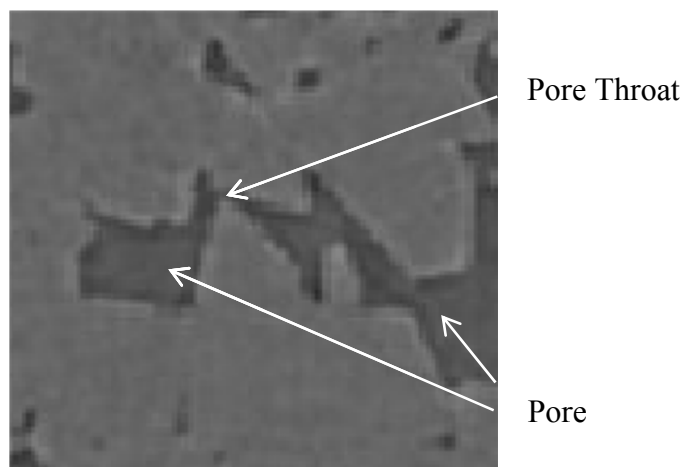


**Figure 2.13: Pore throat of aggregate pore that dictates MIP diameter**

With its drawbacks, MIP can detect pores with a diameter of  $0.0055\mu\text{m}$  (Cnuddle et al., 2008), while the smallest diameter of a pore detectable by CT is dictated by the resolution. Cnuddle et al. (2008) establish that MIP produced a higher overall porosity than CT. Cnuddle et al. (2008) also found that vacuum absorption produced fairly close porosities to that of CT. When considering only pore ranges above the minimum resolution of the CT, MIP and CT porosities were fairly close for the building stones under consideration. Even with somewhat noisy images, CT can produce accurate porosities, provided the pore size is larger than the resolution of the image.

Another advantage of 3D CT is the ability to visualize and quantify the development of micro-cracks within a sample. As micro-cracks develop in concrete or aggregates, the strength of the material decreases because the micro-cracks create fracture planes of weakness. As the material develops more micro-cracks under the same loading conditions, failure is more likely to occur, such as durability cracking or aggregate pop-outs in a concrete pavement. Micro-cracks develop from forces on or inside the materials,

such as compression loads on the material or the cyclic pressures from water freezing and thawing inside the pores of the material. Researchers, including Landis et al. (2007) and Alshibli and Hasan (2010), conducted their work with a CT by scanning objects during loading. Test devices were created with transparent casing to scan specimens under an increasing load, where microstructural changes can be monitored at each loading step by taking a complete X-ray scan. Landis et al. (2007) used this method to monitor the development of micro-cracks in a concrete specimen under increasing loads. They expected and found that as the load increased, the cracking of the specimen increased, as presented in Figure 2.14.

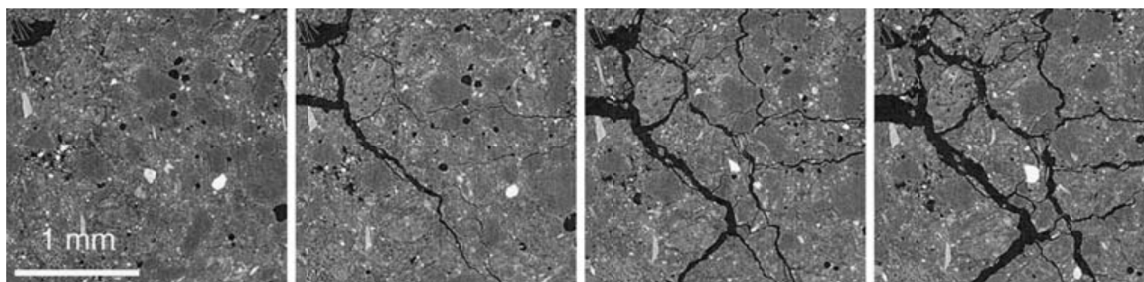


**Figure 2.14: Increase in interior cracking of a concrete specimen with increasing load as visualized with CT (Landis et al., 2007)**

Cnuddle et al. (2007) research effort included measuring the total number of voids and volume and surface area of each void within the specimen. The increase in void volume and surface area was contributed to the growth of cracks. The researchers also noted the total number of voids decreased as the volume and surface area increased, contributing this phenomenon to the isolated voids becoming increasingly connected by cracks.

Landis et al. (2007) attempted to correlate crack properties with measurements of bulk properties of the concrete tested.

### **2.3.3 Three-Dimensional Visualization**

Another benefit of 3D CT is the ability to create volume renderings of the 3D images or certain portions of the images. Three-dimensional images of a material and the void space within the material can be viewed separately. Three-dimensional volumes allow researchers to visualize the complexity of pore networks within an object. It has been established that visualization using 3D CT is more accurate than alternative 2D methods, and can give much insight about the interior of an object. Materials such as concrete and aggregates are visually like a black box, hard to visualize the interior based on conventional pore characteristic methods. CT makes it possible to visually differentiate between two different samples, as shown in Figure 2.15.

Figure 2.15 presents the pore space within two aggregates. The 3D view of pore space in Figure 2.15 (b) is determined to be many small isolated pores, while the pores in Figure 2.15 (d) are a system of highly interconnected pores. This visualization can provide useful information on the pore distribution in a material and can be used with quantitative measurements of the pores to make preliminary assessments of the material.



(a) 3D volume rendering of an aggregate



(b) 3D volume rendering of pores within the aggregate



(c) 3D volume rendering of an aggregate



(d) 3D volume rendering of pores within the aggregate

**Figure 2.15: Two different types of pore distribution within an aggregate**

## Chapter 3

### Research Methodology

This chapter presents the research methodologies utilized to investigate pore space distribution and connectivity in aggregate particles. Methods of testing aggregates to simulate freeze-thaw effects on aggregate durability are also presented. The computed tomography process to acquire high resolution images of virgin and treated aggregate particles is described in detail, along with the post-processing steps to characterize the porosity of the investigated aggregates.

#### 3.1 Investigated Aggregates

##### 3.1.1 Aggregate Sources

The coarse aggregates used in this study were collected for another research project conducted by Titi et al. (2005) for the Minnesota Department of Transportation (Mn/DOT). These aggregates represent a wide range of types and sources used in Mn/DOT highway construction projects. In addition, an aggregate type was obtained from Dane County, WI, which is used in Wisconsin Department of Transportation construction projects. A general description of each aggregate type is presented in Table 3.1. The aggregate types are of sedimentary, igneous, and metamorphic rock origin. The aggregate types include crushed limestone (calcium carbonates), crushed granite, and quartzite. Figure 3.1 depicts pictures of the coarse aggregates selected for this study.

**Table 3.1: General description of the aggregates used in this study (after Titi et al., 2005)**

<b>Aggregate Source</b>	<b>General Description and Predominant Constituents</b>
Michigan Limestone, Cedarville Plant	Crushed limestone particles of angular shape, rough surface and light color
Martin Marietta, St. Cloud	Crushed granite particles of angular shape and dark color
Ulland, Northwood, IA	Crushed dolomitic limestone particles of angular shape, rough surface and dark color
New Ulm	Crushed quartzite particles of angular shape and dark color
Goldberg, Rochester	Crushed limestone particles of angular shape, rough surface and light color
Kraemer, Burnsville	Crushed limestone particles of angular shape, rough surface and light color
Shirley (Larson), Grey Cloud	Crushed limestone particles of angular shape, rough surface and light color
Dane County, WI	Crushed dolomitic limestone particles of angular shape and rough surface

### 3.1.2 Specific Gravity and Absorption Tests

Titi et al. (2005) tested the aggregates to determine their bulk specific gravity, saturated surface dry (SSD) bulk specific gravity, and the apparent specific gravity, and determined the absorption values of the aggregates. Specific gravity and absorption of aggregate samples were determined using ASTM C 127: Standard Test Method for Specific Gravity and Absorption of Coarse Aggregates. Table 3.2 presents the results of the specific gravity and absorption tests of the investigated coarse aggregates. Specific gravity values of the investigated coarse aggregates range from 2.62 to 2.76.



(a) Kraemer



(b) Michigan Limestone



(c) New Ulm



(d) Larson



(e) Martin Marietta



(f) Goldberg



(g) Ulland



(h) Dane County, WI

**Figure 3.1: Pictures of the investigated aggregates used in this study (after Titi et al., 2005)**

The coarse aggregate from New Ulm possessed the lowest specific gravity with bulk specific gravity of 2.62. The highest bulk specific gravity was obtained for Michigan limestone with a value of 2.76. Absorption of the aggregate samples varied from 0.5% for Martin granite to 2.2% for the limestone from the Larson pit.

**Table 3.2: Specific gravity and absorption calculation of different aggregate samples (after Titi et al., 2005)**

Aggregate Type	Bulk Specific Gravity	Bulk Specific Gravity (SSD)	Apparent Specific Gravity	Absorption (%)
Shirley, Grey Cloud (Larson)	2.64	2.69	2.80	2.20
Ulland, Northwood, IA	2.70	2.72	2.78	1.10
St. Cloud (Martin-Marietta)	2.71	2.72	2.75	0.50
Goldberg, Rochester	2.66	2.70	2.78	1.70
Kraemer, Burnsville	2.63	2.69	2.79	2.10
New Ulm	2.62	2.63	2.66	0.70
Michigan Limestone	2.76	2.78	2.81	0.60

### 3.1.3 Rapid Chloride Permeability Test

Titi et al. (2005) used the investigated aggregates to prepare fresh Portland cement concrete according to Mn/DOT specifications. Concrete cylinders were cast and kept in a moist curing room until they were subjected to the laboratory-testing program.

Concrete specimens were subjected to Rapid Chloride Permeability Test (RCPT) to evaluate the ability of the concrete made from different aggregate types to resisting the penetration of chloride ions. RCPT was performed on the specimens according to the AASHTO T 277 standard procedure. The RCPT was conducted on concrete specimens at ages of 28, 56, and 91 days. RCPT results are presented in Table 3.3.

**Table 3.3: Results of RCPT conducted on concrete specimens at different ages (after Titi, et al., 2005)**

Sample Type	Trial Mix #	Sample Position	Total Charge Passed (Coulomb)		
			28-Day	56-Day	91-Day
Michigan	1	Top	1,878	1,122	732
Limestone	3	Top	1,519	829	584
Martin Marietta	1	Top	1,589	912	644
	2	Top	1,769	933	647
	3	Top	1,559	984	588
Ulland	1	Top	2,096	1,175	974
	2	Top	1,941	1,174	827
	3	Top	2,004	1,113	814
New Ulm	1	Top	1,782	925	701
	2	Top	1,351	740	514
	3	Top	1,565	949	587
Goldberg	1	Top	2,432	1,074 <sup>(61)*</sup>	984
	2	Top	2,065	1,104	899
	3	Top	2,140	1,096 <sup>(60)*</sup>	896
Kraemer	1	Top	2,648	1,463	1,195
	2	Top	2,713	1,695	1,269
	3	Top	2,457	1,460	1,194
Larson	1	Top	2,598	1,668	1,206
	2	Top	2,332	1,163	1,110
	3	Top	2,666	1,757	1,393

## 3.2 Aggregate Preparation

### 3.2.1 Sodium Sulfate Soundness Test

All investigated coarse aggregates were subjected to the sodium sulfate soundness test according to AASHTO T104. A saturated solution of sodium sulfate was prepared from sodium sulfate anhydrous and distilled water. A sample of each type of aggregate was soaked in the solution at room temperature for 17 hours in a covered container (Figure 3.2). The samples were then drained and dried in an oven at 110° C for six hours. This wetting and drying is considered one cycle of the sodium sulfate soundness test. A portion of each aggregate sample was set aside and another cycle was performed. Five cycles were performed and a small portion of each sample was set aside at the completion of each cycle for further CT evaluation.

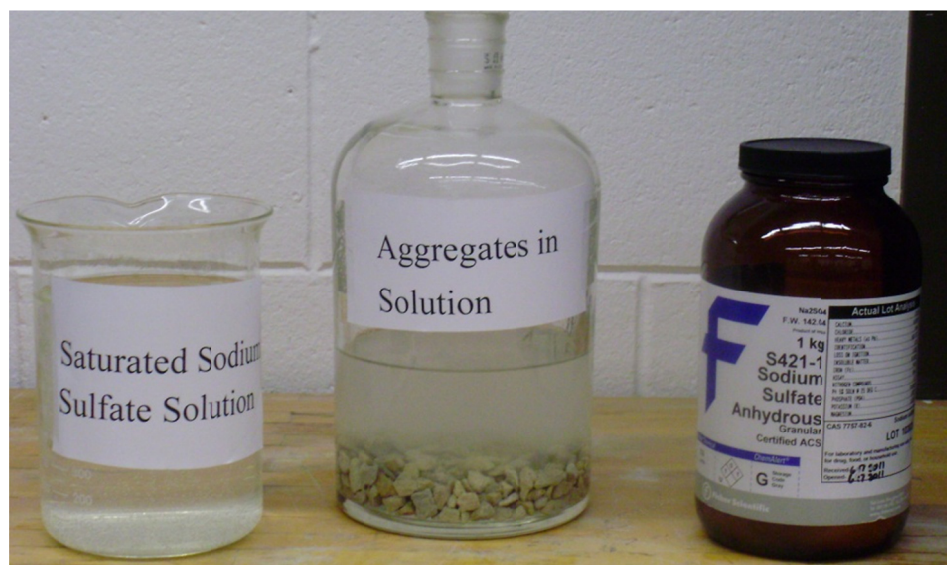


**Figure 3.2: Sodium sulfate soundness test setup with aggregates soaking in solution**

### 3.2.2 Rock Corings

Large pieces of rock from three aggregate quarry sources were acquired. Core specimens measuring approximately 4 mm in diameter and 15 mm in height were obtained from these rocks using an electric hand drill and coring bit, as depicted in Figure 3.3. Cores were drilled from the same area of each rock to assure similar internal structure before treatment. Enough specimens were cored to examine one virgin specimen and two specimens for each of the five sulfate soundness test cycles. In addition, two specimens were obtained to examine the effects of 30 and 45 cycles of unconfined freeze-thaw tests. Figure 3.3 (b) shows aggregate core samples drilled from the three aggregate sources.



(a) Rock samples and drill

(b) Cores extracted from rock samples

**Figure 3.3: Rock samples and tool used to extract core specimens for CT scanning**

### 3.2.3 Soundness of Aggregates by Freezing and Thawing

The rock cores from the three aggregate quarry sources were subjected to unconfined freezing and thawing following the AASHTO T103 procedure A. The cores were first soaked in water for 24 hours and then placed in a cyclic freeze-thaw chamber. The

freeze-thaw chamber, shown in Figure 3.4, can perform five freezing and thawing cycles within a 24 hour period. The freezer reached  $-60^{\circ}\text{C}$  during freezing and  $+10^{\circ}\text{C}$  during thawing. Freezing specimens to  $-60^{\circ}\text{C}$  is much more severe than the maximum freezing temperature of  $-26^{\circ}\text{C}$  as specified by AASHTO T103. Two cores of each rock sample were removed from the freezer after 30 and 45 freeze thaw cycles and were dried at  $110^{\circ}\text{C}$  for six hours in the drying oven shown in Figure 3.5.



**Figure 3.4: Freezing and thawing chamber used in this study**



**Figure 3.5: Drying oven used in this study to dry aggregates**

### **3.3 Advanced Photon Source**

Advanced Photon Source is part of the Argonne National Laboratory (ANL) of the U.S. Department of Energy. ANL is located on 1500 acres southwest of Chicago and has several science and engineering research facilities. Advanced Photon Source (APS) is one of the world's most brilliant sources for synchrotron light. An aerial photograph of APS is shown in Figure 3.6.



**Figure 3.6: Aerial photograph of Advanced Photon Source**  
([acaschool.iit.edu/lectures07/Howard\\_SynchrRad.ppt](http://acaschool.iit.edu/lectures07/Howard_SynchrRad.ppt))

### 3.3.1 Major Components of the Advanced Photon Source

The starting point of creating X-rays at APS is the linear accelerator (LINAC), where electrons are created by heating a cathode to about 1100° C and accelerating those electrons with high voltage alternating electric fields. The electrons are accelerated to 99.999% of the speed of light and 450 MeV, making them relativistic (moving at a high enough velocity to cause a significant change in properties). The LINAC then injects the electrons into the booster synchrotron, which further accelerates the electrons to 99.999999% the speed of light and to 7 GeV. The electrons are accelerated in the booster synchrotron by electrical fields in four radio frequency (RF) cavities and circulated by bending and focusing magnets. The electrical acceleration and magnet circulation are synchronized to retain the circular path. Figure 3.7 illustrates the major components of APS, including the LINAC, booster synchrotron, and storage ring.

The electrons are then injected from the synchrotron booster into the storage ring, which is 1,104 m in circumference. The electrons are kept in circulation in an aluminum-alloy vacuum tube by electromagnets, which focus the electrons into a very small and powerful beam. Electrons are replenished every 12 hours from the LINAC to account for the energy lost during experimentation. There are 40 straight sections (sectors) integrated into the storage ring that allow for beam injection, radio frequency equipment and experimentation. Each sector has at least two X-ray beamlines, one from the bending magnet and one from the insertion device. The insertion devices (ID) and bending magnets (BM) at APS provide powerful and brilliant X-rays for a variety of experiments. Figure 3.8 compares the spectral brilliance of the IDs and BMs of APS with other sources.

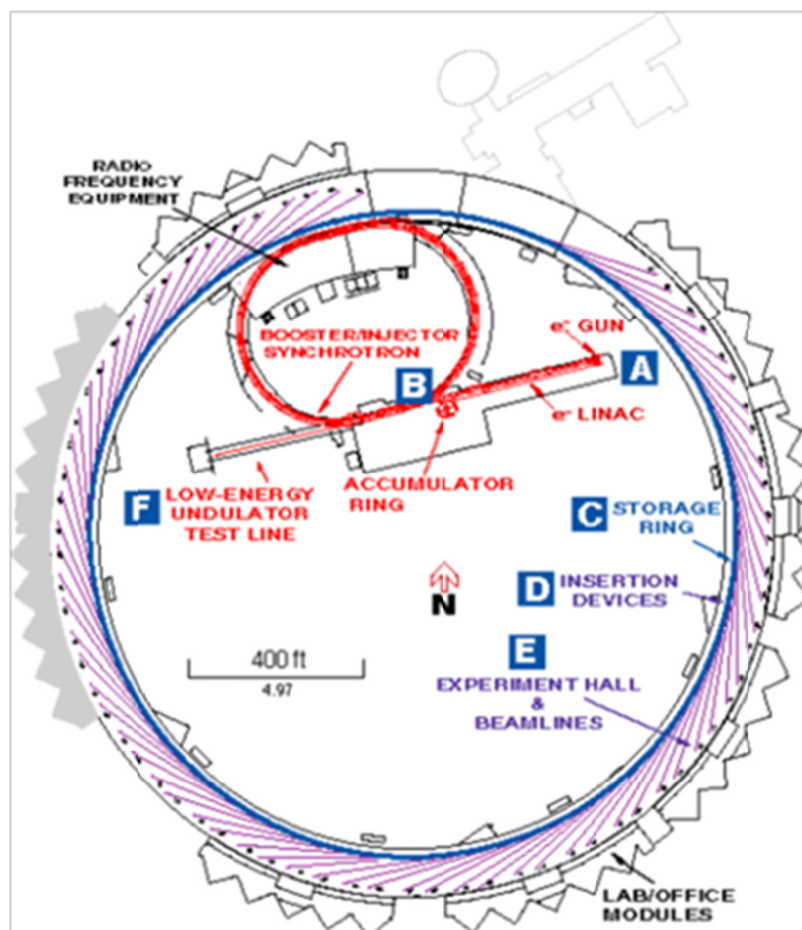


**Figure 3.7: Schematic of the major components of Advanced Photon Source** ([acaschool.iit.edu/lectures07/Howard\\_SynchrRad.ppt](https://acaschool.iit.edu/lectures07/Howard_SynchrRad.ppt))

### 3.3.2 Advanced Photon Source Beamline Overview

Each beamline has optics (monochromaters, crystals and/or mirrors) designed to optimize the beam for specific use, which is a very small portion of the original beamline. At the end of each beamline is a radiation proof experiment hutch customized for performing various types of experiments. Figure 3.9 depicts the insertion device and bending magnet sources for a beamline at APS.

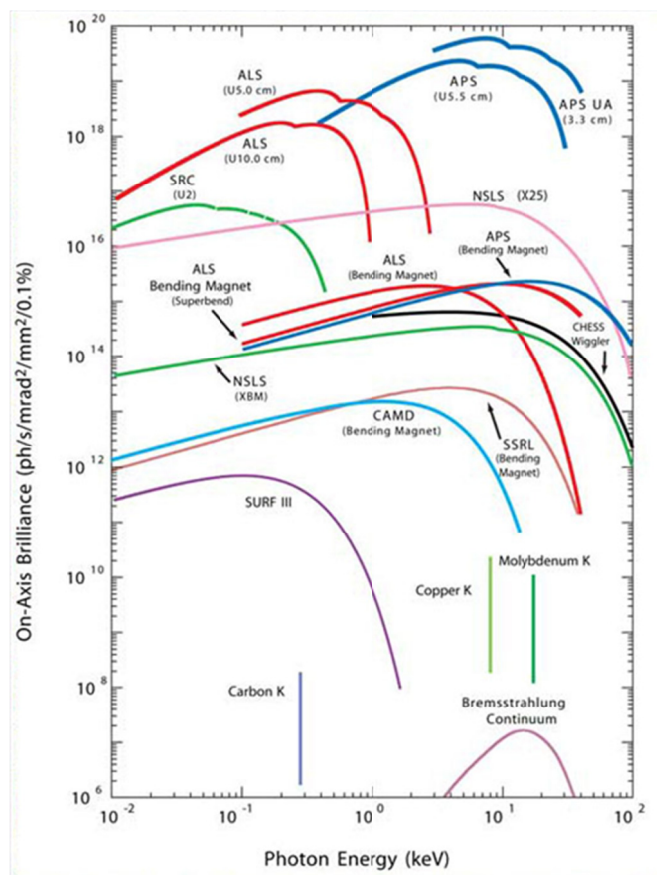


Figure 3.8: Photon Energy and Brilliance of Various Sources (Bunker, [acaschool.iit.edu/lectures07/Howard\\_SynchrRad.ppt](http://acaschool.iit.edu/lectures07/Howard_SynchrRad.ppt).)

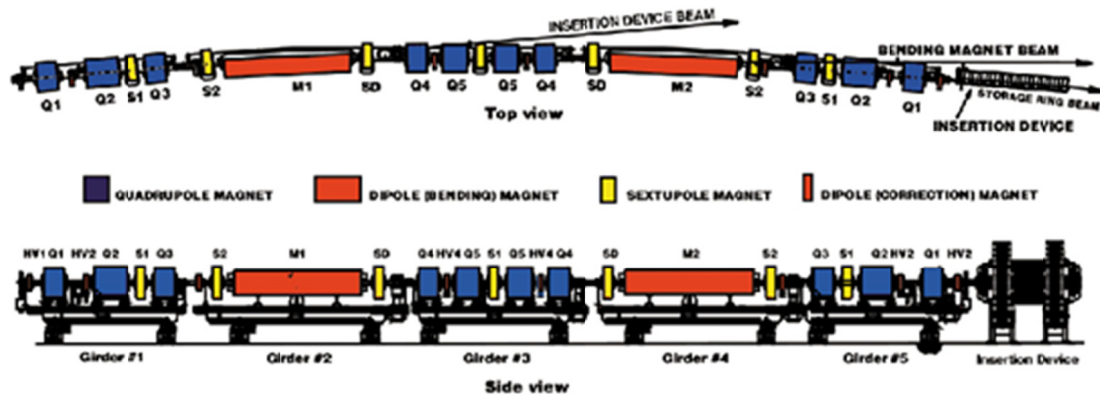


Figure 3.9: Typical Sector at APS (Borland et al., 2010)

### 3.3.3 Sector 13 at Advanced Photon Source

Sectors 13, 14, and 15 at APS are managed by the Center for Advanced Radiation Sources (CARS), which is a department-level center with the University of Chicago. Sector 13 is managed by a subdivision of CARS, GeoSoilEnviroCARS, which is dedicated to research on earth materials and is open to the scientific community. Sector 13 includes a bending magnet beamline and an insertion device beamline, each of which has two optics enclosures and two experiment stations. The bending magnet beamline is split in one of the optic enclosures into two experimental stations. Proposals for beam time at Sector 13 are accepted on a three-month cycle. The computed tomography for the current research was conducted at Sector 13 on the bending magnet beamline in experiment hutch D, which is denoted 13-BM-D. The radiation-proof hutch door is shown in Figure 3.10. Beam time at station 13-BM-D was applied for and awarded for this tomography research on three separate occasions.



**Figure 3.10: Entrance to experiment hutch 13-BM-D at GSECARS**

### 3.3.4 Beamline 13-BM-D

Beamline 13-BM-D is the end-station at the bending magnet of Sector 13 and is specialized for earth and environmental science research. 13-BM-D has a water-cooled dual-crystal silicon monochromator 25.5 meters from the source that operates from 4.5-70 keV. Another component along the beamline is a vertical focusing mirror 49.3 meters from the source. The beam size of 13-BM-D is  $10\ \mu\text{m} \times 30\ \mu\text{m}$  when focused and  $50\ \text{mm} \times 4\ \text{mm}$  when unfocused. Figure 3.11 shows a schematic of Sector 13.

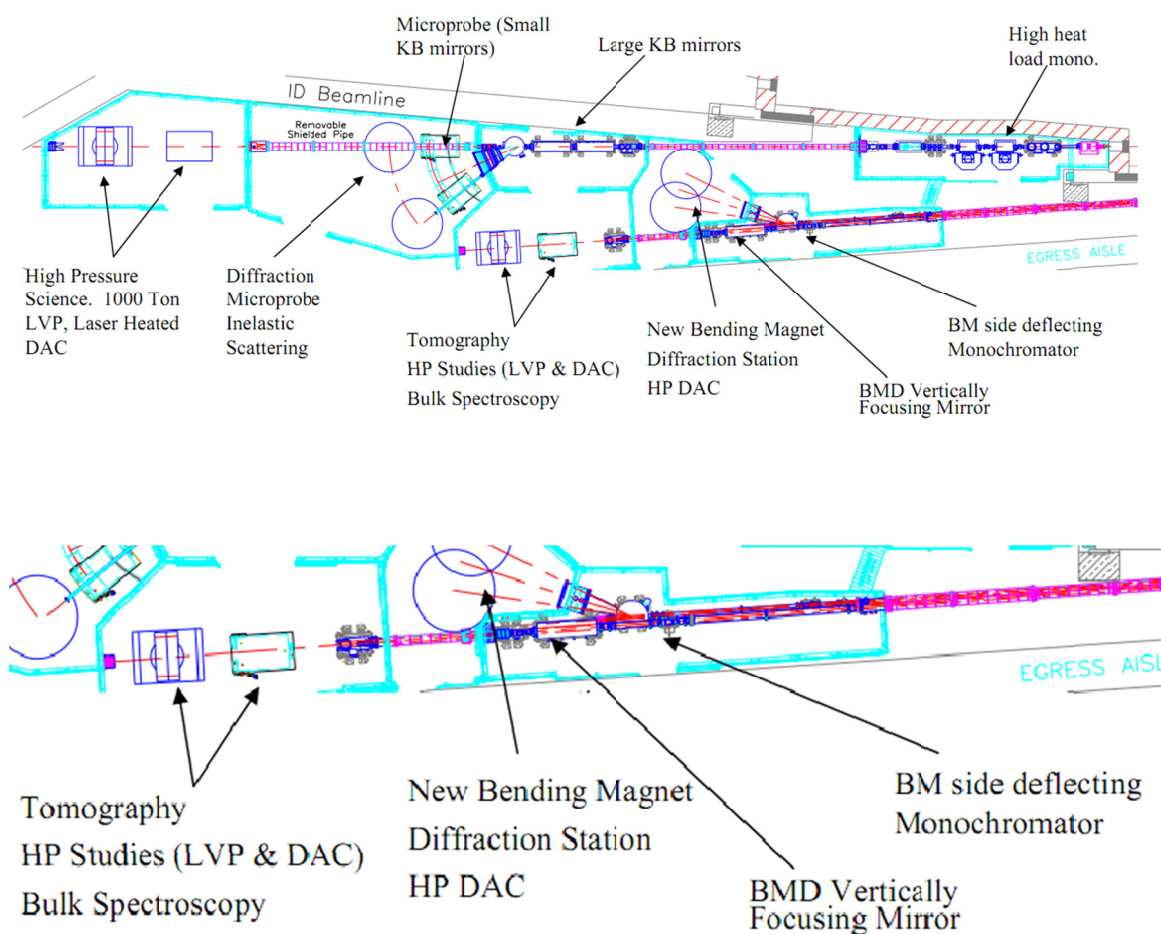


**Figure 3.11: Schematic of Sector 13 Beamlines (Advanced Photon Source, 2011)**

The X-ray source is filtered by the monochromators and focused with the focusing mirror before it is trimmed with horizontal and vertical slits and sent to the sample. The beam is attenuated through the sample and through a scintillator that turns the X-ray photons into flashes of light, which are reflected off of a mirror into a CCD detection system. Figure 3.12 depicts a setup inside the hutch of a typical beamline end-station. The experimental setup of the beamline end in sector 13-BM-D at APS is shown in Figure 3.13. The detection system used in the imaging was a CoolSNAP HQ<sup>2</sup> and a Nikon Macro 37 mm lens with a 5 mm tube at minimum focus. The CoolSNAP HQ<sup>2</sup> has a 1,392×1,040 pixel imaging array of 6.45 μm each. The detector also can be binned up to 8×8 pixels. Binning the images involves combining pixels in the detector to create a ‘super pixel’ by averaging adjacent pixels into one. If pixels are binned together and averaged as one pixel, the image resolution and imaging time decreases.

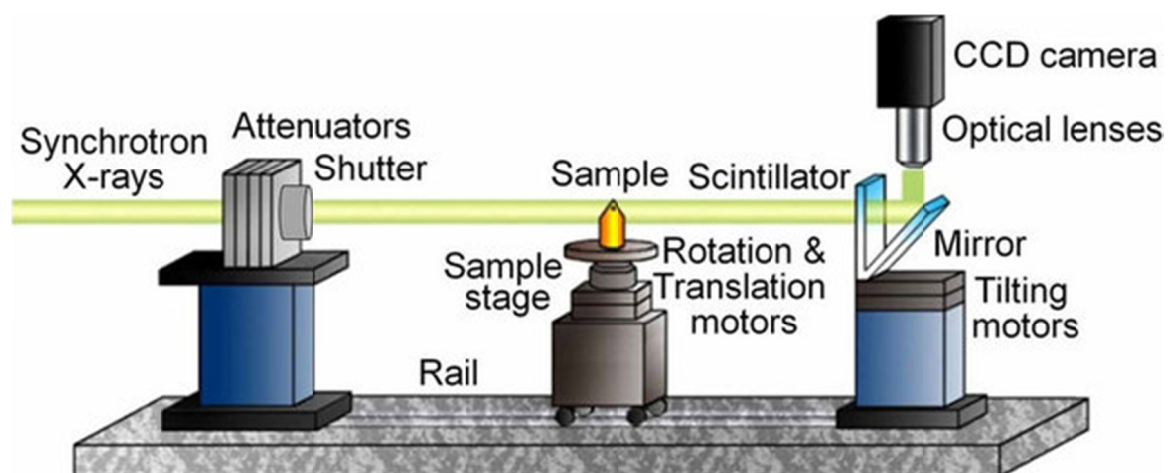


**Figure 3.12: Schematic of X-ray path in experiment hutch (Kim et al., 2011)**



**Figure 3.13: Sample on rotation stage, scintillator, mirror and CCD system**

### **3.3.5 Computed Tomography Procedure**

Computed tomography scans were conducted at beamline 13-BM-D of APS for this 3D CT research during three separate visits. To acquire high resolution images for this research, aggregate samples must be small enough to fit in the beam (<5 mm wide). The first step is to place a sample on the translation/rotation stage, then set up the X-ray intensity and resolution. Figure 3.14 shows the placement of the aggregate sample in putty on the stage as vertically as possible to help prevent any imaging artifacts, as well as other CT image acquiring steps. The experiment hutch was then searched and the door was closed and magnetically locked. The lights inside the hutch were turned off and the slit shutters were opened to allow X-rays to travel along the designated path through the sample and scintillator and into the camera.



**Figure 3.14: Aggregate scanning during various trips to APS**

The setup process involved zooming and focusing the camera to capture the entire sample clearly, with some air on each side, and selecting the optimal energy to capture all aspects of the sample. The X-ray source was filtered to a single energy optimal for the aggregate by rotating the crystal monochromators, which were kept parallel. Unwanted X-ray

energies were reflected by the crystalline structure in the monochromators according to Bragg's Law and based on the angle of rotation, allowed only a very narrow band of energy (very close to a single energy) through them. The exposure time for a sample was balanced with the energy to achieve a clear image. An increase in exposure time will increase the intensity detected by the camera. If the camera is exposed for too long, it will become oversaturated with X-rays and the image will not be clear. The exposure time is selected based on the saturation of the camera, which is determined by the energy of the X-ray without the sample in view. The setup process had to be completed only once at the beginning of testing and the settings remained the same throughout the rest of the scans.

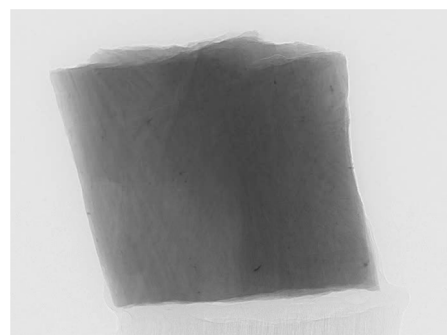
The scans acquired on the first occasion were binned by a factor of 2 in each direction. The camera field of view was 2.95 mm wide  $\times$  2.20 mm high with an intensity of 28 keV resulted in a binned resolution of 4.24  $\mu\text{m}$  per voxel. To cover the entire height, two vertical scans were taken of each sample and stitched together. The scans acquired on the second occasion were unbinned with a field of view of 4.96 mm wide  $\times$  3.71 mm high with an exposure time of 1.93 seconds and energy of 28 keV per scan, which resulted in a resolution of 3.56  $\mu\text{m}$  per voxel. The scans of the third occasion were also unbinned with a field of view of 6.44 mm wide  $\times$  4.82 mm high, exposure time of one second, 28 keV energy and resulting resolution of 4.63  $\mu\text{m}$  per voxel. The field of view along with the exposure time and resulting resolution were the only variables changed between the three scanning occasions because binning of the pixels was chosen on the first occasion and the average size of the sample was different on the second and third occasions. After the setup, scanning followed the same procedure for every sample. A new sample was placed

on the rotation stage and the experiment hutch was evacuated. The beam was turned on and the sample was aligned with the translation/rotation stage via computer software. A file name was given to each sample and scanning was started.

For each sample, scans were acquired at every 0.2 degrees over 180 degrees rotation, resulting in 900 scans. The sample was constantly rotating and scans were taken “on the fly” instead of stopping the sample for every scan, which decreases the scanning time. For every 100 angles, 10 dark current and 10 white field images were taken to calibrate the images and help reduce image artifacts. White field normalization, scanning in the absence of a sample, corrected possible defects in the X-ray, scintillator, or detection system. Dark fields were taken with the shutters closed, which corrects for the signal measured without X-rays. Without normalization a blank image will appear, as depicted in Figure 3.15 (a). Normalizing the images with the dark currents and white fields produce an image as shown in Figure 3.15 (b). The dark current is subtracted and the image is divided by the average of all flat fields. Pixels in the detector that are hit by X-rays directly are removed along with any other imperfections.



(a) Image That has not been normalized



(b) Normalized image

**Figure 3.15: Computed tomography scan before and after normalization process**

To create a 3D image that can be examined internally, the normalized data must be further preprocessed. First a filtered back-projection algorithm is applied to the data. A Shepp-Logan filter is applied to the sinogram and then the sinogram was back-projected using a Fourier transform. Figure 3.16 presents data for a single detector of the normalized data, sinogram of data and sinogram after the Shepp-Logan filter is applied

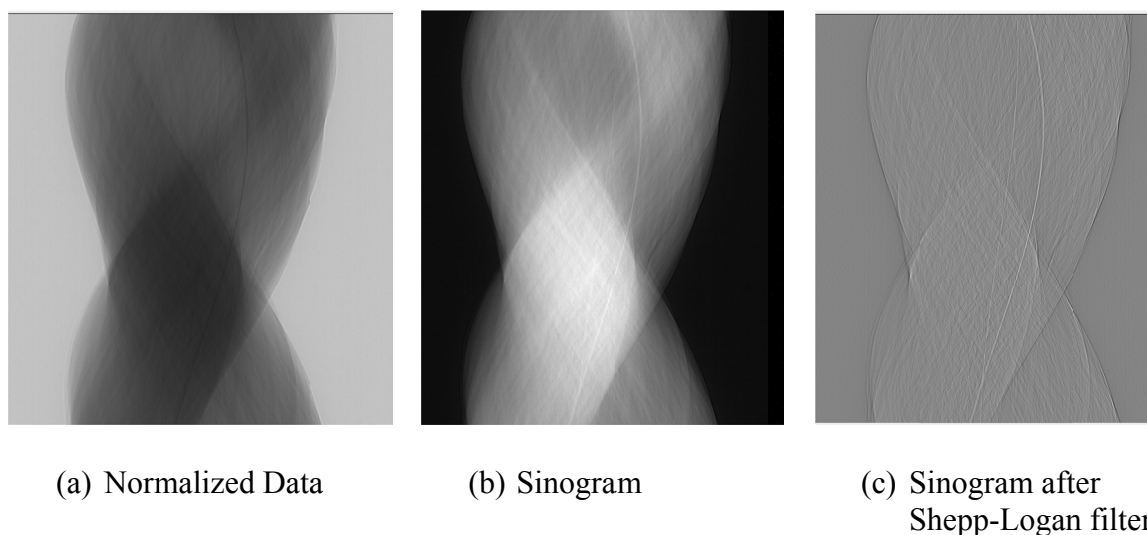
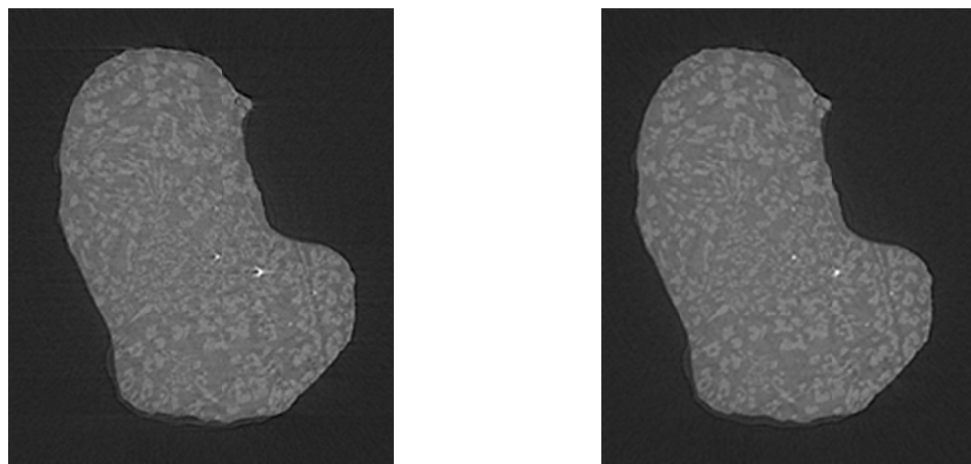


**Figure 3.16: Example of different stages of data preprocessing for single detector row (Rivers, 2010)**

Since it is difficult to place the samples perfectly vertical to rotate in the center of the beam, a correction for the center of rotation was performed. Optimizing the center of rotation reduces artifacts in the images. Figure 3.17 illustrates the effect of the center of rotation on the quality of the image. Although off by only 1.5 pixels to the left in Figure 3.17 (a), features in the image are distorted. For example, the bright spot in the image in Figure 3.17 (a) is cupped opening to the left. If the cup was in the other direction, the rotation center is to the right of the optimum. The feature is not cupped in Figure 3.17 (b).



(a) Cupped feature within image

(b) Feature not cupped

**Figure 3.17: Image with rotation center off by 1.5 pixels and cupped feature (a) and image with correct rotation center with no distortion (Rivers, 2010)**

GSECARS uses IDL programs to optimize the rotation center. For center optimization, one slice is chosen near the bottom and one slice is chosen near the top. For each of those slices, the entropy, which is the measure of the sharpness of the image histogram, is computed and the optimal rotation center occurs when the entropy is minimized. Figure 3.18 presents an example of the IDL graph used to find the minimal entropy of a slice. The minimal entropy is determined with IDL for one slice near the top of the image and one slice near the bottom of the image. The rest of the slices in the image are then reconstructed based on the two rotation center values found near the top and bottom.

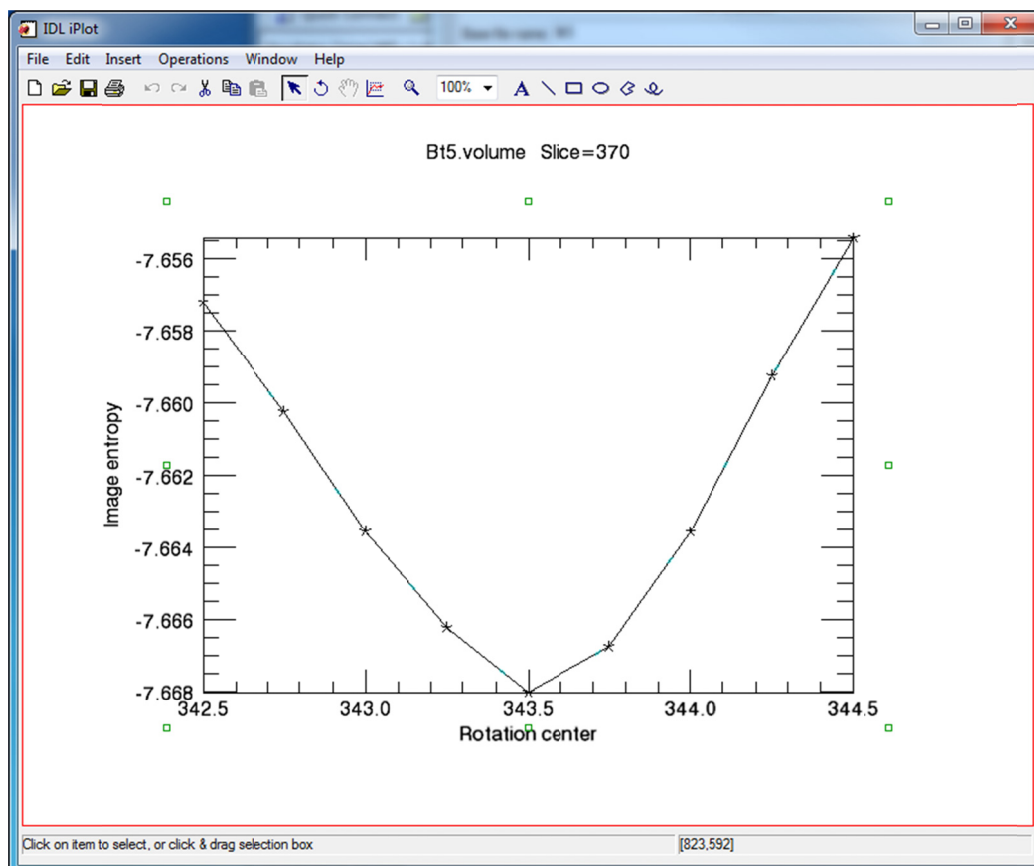


**Figure 3.18: Optimization of rotation center of a slice based on minimal entropy (Rivers, 2010)**

The resulting images were almost artifact-free and relatively free of noise, as shown in Figure 3.19. This image is one of 1,390 slices obtained in the XY plane. Between the three trips to APS, 35 aggregate samples were scanned at least twice to cover the full height of the specimen. The scan time ranged from 45 minutes to 1.5 hours for each aggregate, with an additional 15 to 30 minutes of reconstruction time. Each of the scans was converted into a stack of .tiff images, and each set of images were approximately 3 Gb in size. Up to this point, the CT data was gathered and processed at Sector 13 of APS and then transferred to an external hard drive to be analyzed at the University of Wisconsin-Milwaukee.

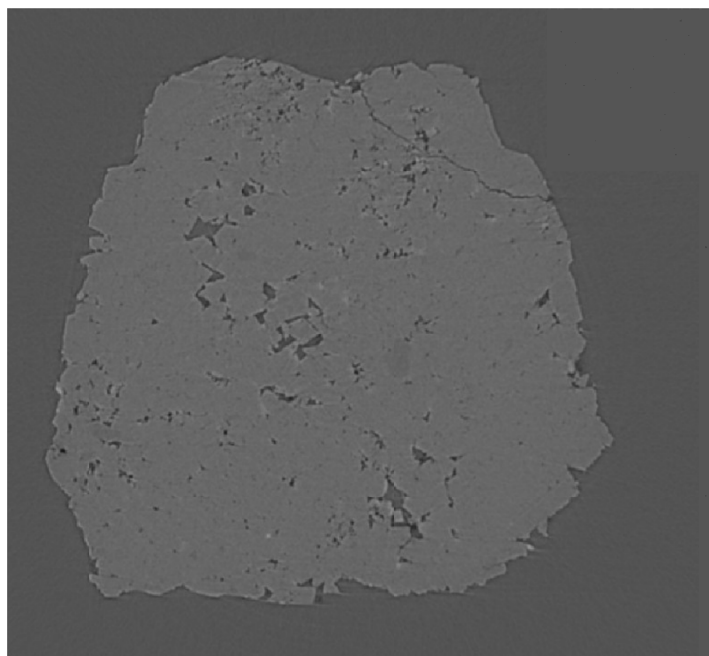


**Figure 3.19: One slice from scan of an aggregate particle with a resolution of 4.24  $\mu\text{m}$  per voxel**

### **3.4 Post Processing**

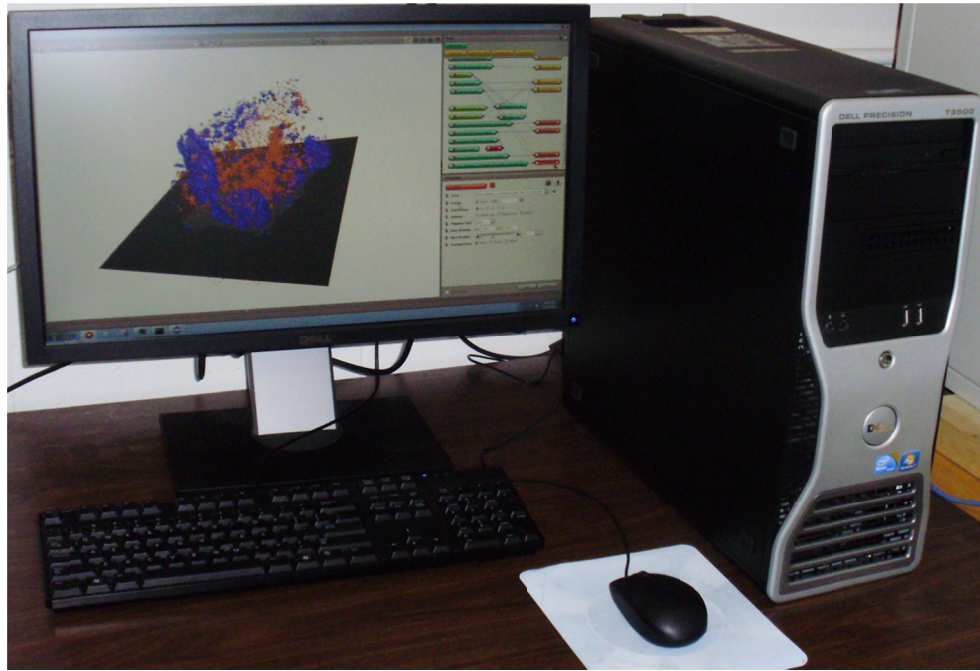
The objective of this study is to characterize pore space and pore space distribution and connectivity in aggregate particles using X-ray CT. Furthermore, analysis of pore space growth due to cycles of sodium sulfate and freeze-thaw soundness tests is of interest; therefore, post-processing will be conducted to support achieving the goals of the research. From 3D CT constructed images the pore structure can be visualized in 2D by the slices and can also be visualized and accurately quantified in 3D. Individual pores can be quantified in terms of their size. Moreover, pores connected to the surface of the aggregate and pores isolated within the aggregate particle can be differentiated. Before any quantification can occur, post-processing of the images must be completed.

### 3.4.1 Post-Processing Workstation

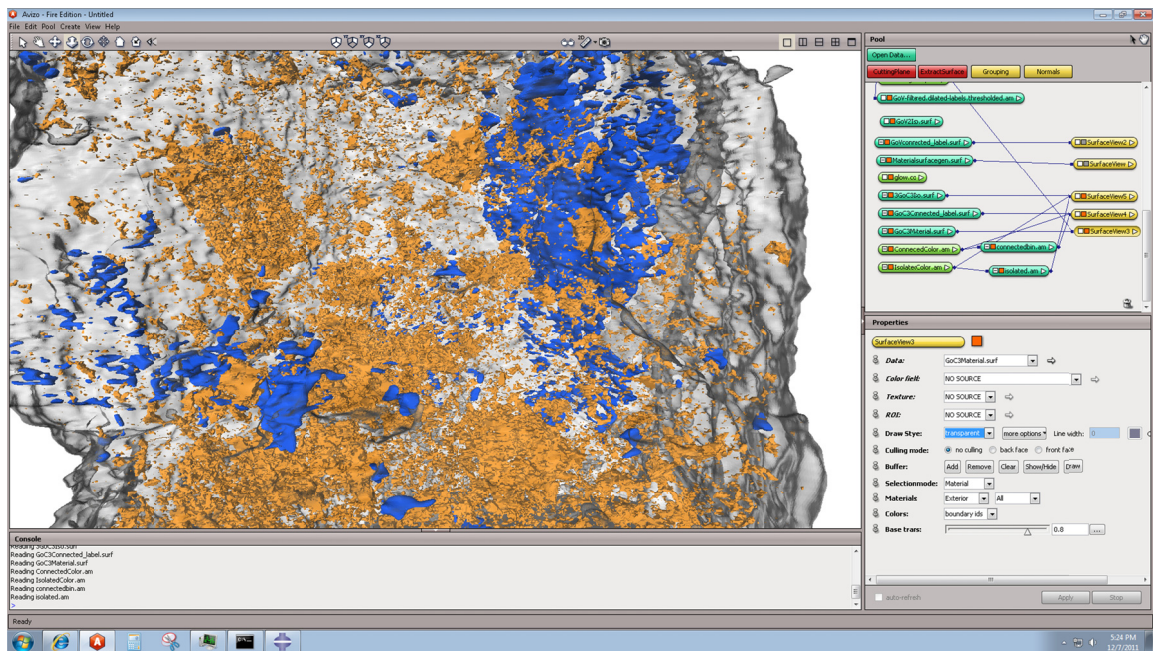
The workstation used for post processing is a Dell Precision T3500 with a Quad Core Intel® Xeon® Processor E5630 with 24 GB of memory and a 2GB NVIDIA® Quadro® 4000 graphics card. The workstation is shown in Figure 3.20 (a). The analysis program, Avizo® Fire version 6.3.1 from Visualization Sciences Group, was used. Avizo Fire® has a broad range of software tools for obtaining and visualizing advanced qualitative and quantitative information on material structure images. A display of the Avizo Fire® interface is displayed in Figure 3.20 (b).

### 3.4.2 Post-Processing Steps

The main post-processing steps for quantifying pore space within the aggregate include segmenting the image through thresholding, isolating the image from the background, isolating each pore, and quantifying the characteristics of each pore. The first step was to load top and bottom scans of the aggregate into the software and merge them together. The height of the scans and the amount of overlap from scanning was known, and there is a 0.1 mm overlap for each scans on the first visit to APS and a 100  $\mu\text{m}$  overlap on the second and third trips. The first scan was loaded normally and the value in the  $z$  direction for the second scan was increased by the height of the sample minus the overlap.



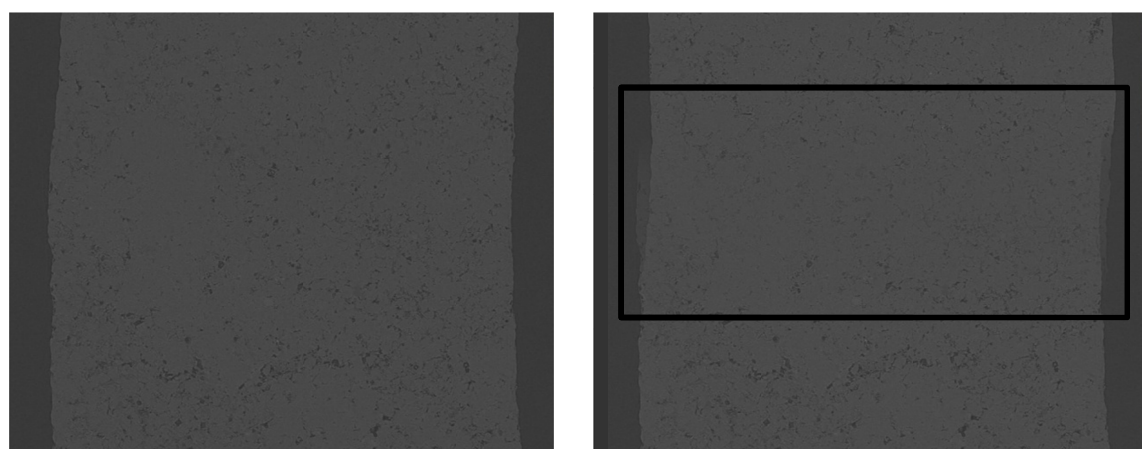
(a) Dell T3500 workstation used for post-processing analysis



(b) Avizo Fire® software interface used for post processing data

**Figure 3.20: Post-processing tools used in this study**

This loading situates both scans into the software and creates a continuous image (Figure 3.21). If the images are merged incorrectly features within the image will be distorted, eliminated or added, leading to error in analysis. Figure 3.21 contains a correctly merged image (a) and incorrectly stitched image (b). The poorly merged image contains distortions around the center where its two data sets were merged.



(a) Continuous image

(b) Poorly merged image

**Figure 3.21: Images that are (a) continuous and (b) poorly merged image from incorrect stitching**

The scans must be merged together into one for quantification and Avizo Fire® has a merging algorithm for combining these images. The intensity value of the pixels in the same location will vary. The algorithm averages the value of the surrounding pixels of both scans, linearly interpolates the pixel values at a single point in the image or approximates a low pass filter. The nearest neighbor method interpolation was used to merge the scans together because it produced accurate results and was not as time consuming as the more accurate method.

The samples were held in place with putty, and during scanning some of it showed in the lower part of some of the images. The images were noisy within the bounds of the putty, which lead to error in quantifying the pore space; therefore, the images that contained putty were cropped to remove it.

One step that applies to many CT images is filtering, which is usually used to reduce noise; however, the CT images acquired in this research were not noisy. Filtering also smoothes pixels in an image, thereby omitting some very small voids and micro-cracks. For these reasons, no filter was applied to the images in this research.

The next step was to segment the image. Each pixel has an intensity value from the imaging process, and the intensities of the pixels corresponding to material solid are much higher than the intensities of those corresponding with air. Segmentation is grouping all the solid material pixel intensities-and assigning them one value, and grouping all the air intensities and assigning them another value, such as 1 for material and 0 for air. This can be done in a variety of ways, including global thresholding, indicator kriging, or watershed segmentation. The trouble zone for segmentation is at the phase boundaries, where it is difficult to determine which phase a pixel belongs to. The CT images in this research consisted of fairly well-defined boundaries in most places. The boundary segmentation issue was addressed by a method in Avizo Fire® using gradient magnitude and the intensity of the voxels in the image. In an image, the gradient magnitude shows the places in the image where there is a high rate of change of voxel intensity, as shown in Figure 3.22.

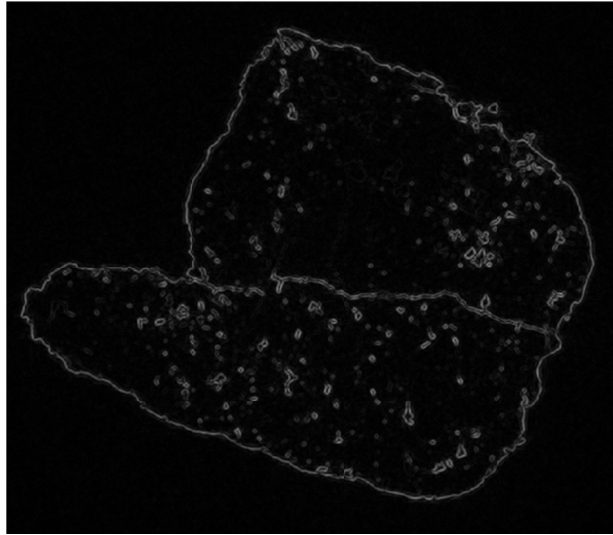


**Figure 3.22: Gradient magnitude of a cross section displaying boundaries between contrasting phases**

Initial classification of the voxels is achieved by interactively choosing intensities that definitely belong to pores and choosing intensities that definitely belong to solid material. The phases are chosen based on a scatterplot of pixel intensity versus gradient magnitude, as illustrated in Figure 3.23. The bright grouping of clusters represents a large number of pixels at certain intensity, which correspond with one of the regions of interest, with air space corresponding with the cluster on the left; the solid material space is the cluster on the right. Both clusters lie close to the X-axis, which corresponds with a low gradient magnitude. The resulting image is binary with a gap of unassigned voxels at areas of high gradient magnitude. Figure 3.24 illustrates the gap of pixels in the histogram of the image left unassigned from the scatterplot selection.

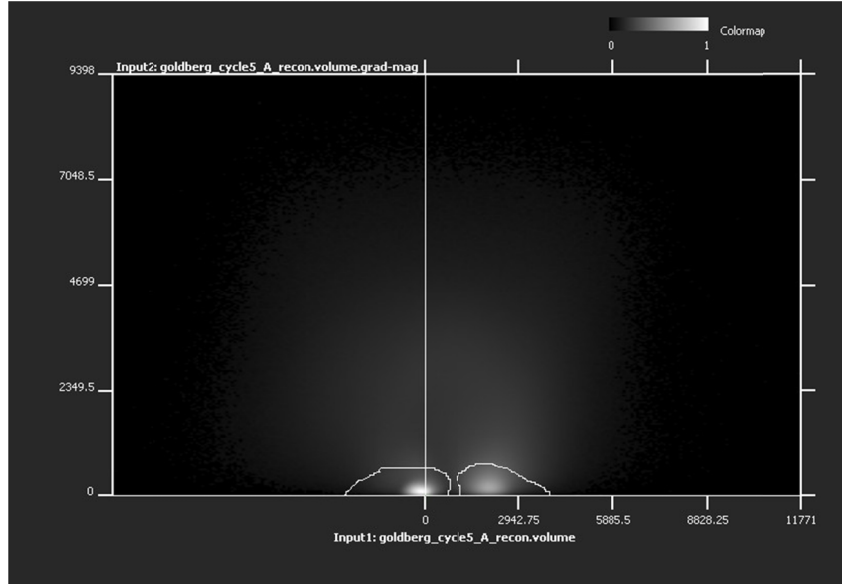


Figure 3.23: Scatterplot with selected clusters

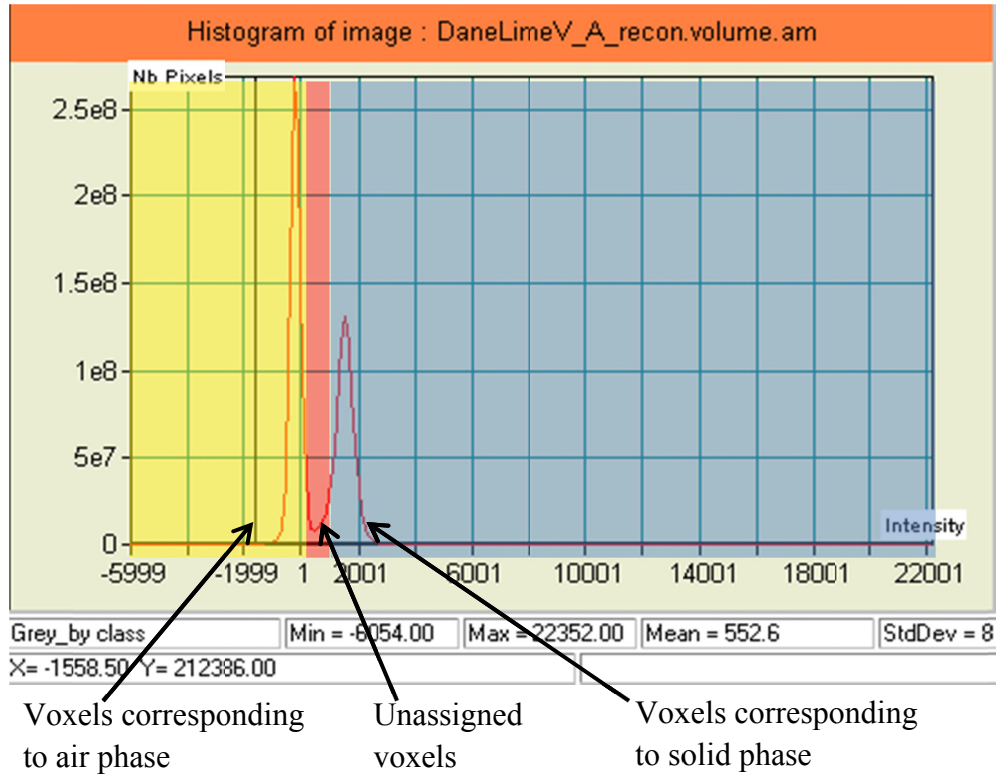
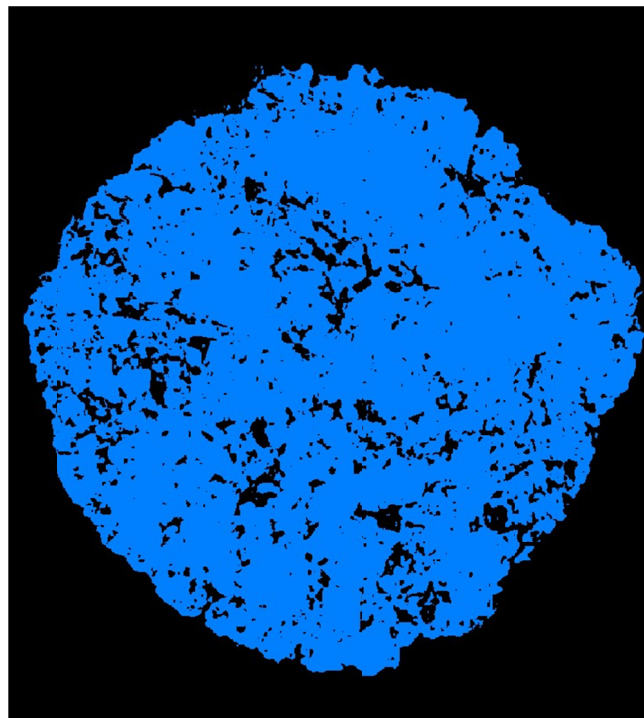


Figure 3.24: Histogram illustrating unassigned voxels that lie near phase boundaries

The unassigned voxels between the chosen thresholding values are given a value based on a watershed algorithm (Roerdink and Meijster, 2001). This algorithm is a local segmentation approach that requires a gradient magnitude map based on the original image (Figure 3.22) and the image with unassigned voxels from the histogram segmentation discussed earlier. Watershed lines are formed based on simulating flooding of a topographic relief of the image, with the watershed lines serving as the dividing lines. Using markers, Avizo Fire® remedies the over-segmentation issue with watershed segmentation (Roerdink and Meijster, 2001 Avizo® 6 User's Guide, 2010). Figure 3.25 depicts the resulting binary image of the material of an aggregate. The original gray scale images and the binary images were visually inspected ensure accurate segmentation.



**Figure 3.25: Binary image of aggregate material obtained using the watershed thresholding algorithm**

The rest of the processing occurs on the binary image resulting from the segmentation. The data was segmented so that a value of one was given to the material solid, and a value of zero was given to all void space so that only the material solid is present—all void space is black and part of the background. An image of the void space (including the background) was created using a “logical not” command (Figure 3.26), which produces an image with all the void space with a value of 1 and the material solid with a value of 0, as shown in Figure 3.26. Some of these voids are isolated completely by material solid, and some are connected to the surface of the aggregate. Voids connected to the surface of an aggregate allow water and other materials to flow into the aggregate. If cracks are formed within the aggregate from loading, the isolated voids might eventually connect to the surface with the cracks; therefore both types of voids are important and analyzed separately.

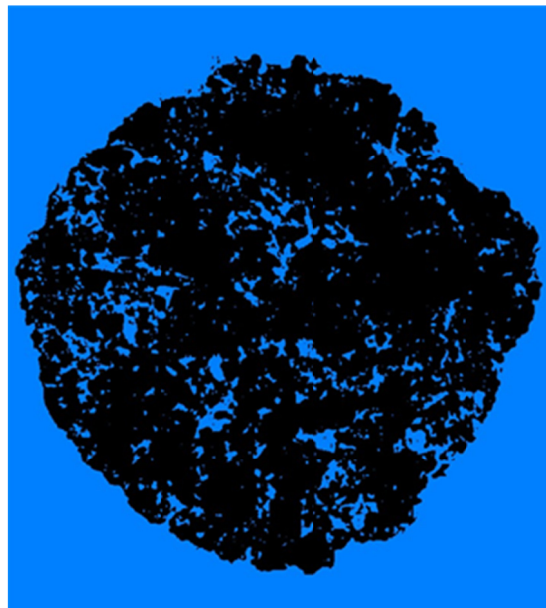


**Figure 3.26: Image of void space in and around aggregate created by “logical not” command**

The material solid and pores within the aggregate must be isolated from the image background, isolation was achieved by starting with a “binseparate” command in Avizo Fire®, which is applied to the binary image of the void space (Figure 3.27 and close-up in Figure 3.28). The “binseparate” command creates a line that splits the voids and separates the connected pores from the background. An example of the lines that the “binseparate” command uses is shown in Figure 3.28. The lines cut off the pores from the exterior space.

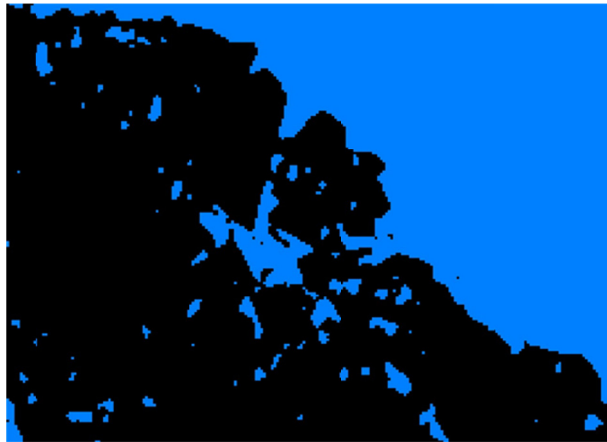


**Figure 3.27: Close-up of void space near surface of aggregate particle**



**Figure 3.28: Lines from “binseparate” command created to split pores from background**

Next, a command was applied to remove the background of the image while keeping the pores. The “border kill” command eliminates all objects that touch the frame of the image, including the background. The pores were separated from the background with a line in the previous step and will not be removed by the command. Figure 3.29 shows the image after the “border kill” command is applied to the image with separated pores.

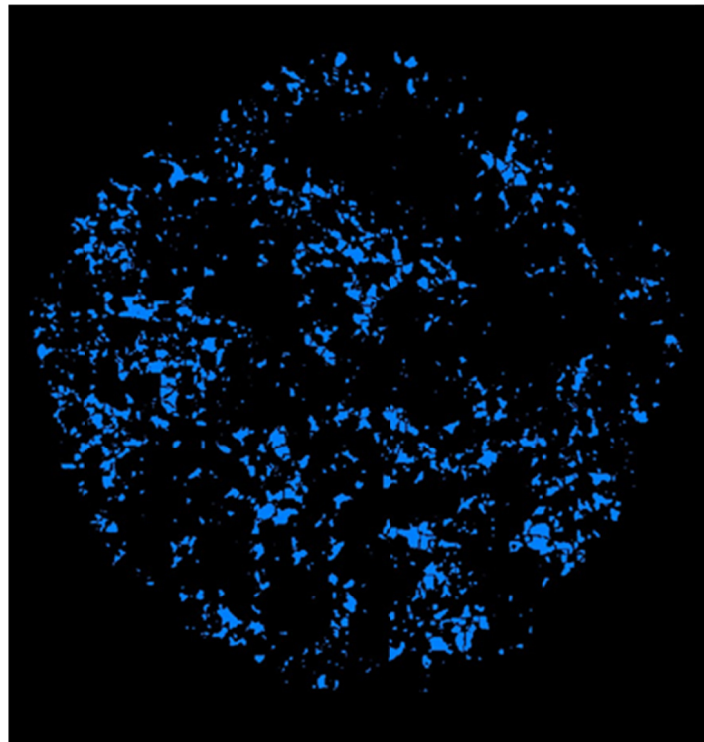


**Figure 3.29: Image resulting from “border kill” command**

The separation lines created in the “binseparate” command must be eliminated because they show up as part of the material solid, but are actually part of the pores. A “logical or” command is applied with two inputs, the binary image of the material and the image separated from the background with “border kill”. This command computes the union of the two images and produces an image of the material plus voids minus the separation

lines that were created with the “binseparate” command, shown in Figure 3.30. Holes in the material show where the “binseparate” command created boundaries and they will be removed in the subsequent steps.

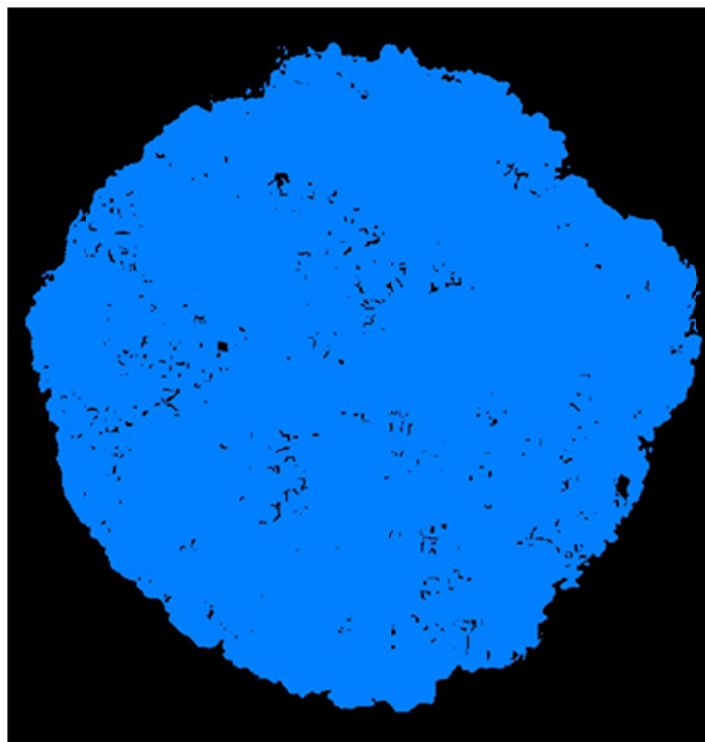


**Figure 3.30: Material with holes from “binseparate” command separation boundaries**

The holes left in the material solid from the separation lines are filled with a command “hole fill.” This command was applied to the image in Figure 3.30 and filled the holes in the image that are completely surrounded by material solid (Figure 3.31). This step finishes a mask that will be used to completely separate the entire aggregate from the background and will allow for analysis of the pores. The “hole fill” command was also applied to the binary image of the solid material, filling all the pores completely surrounded by material solid, but not the pores connected to the surface of the aggregate

particle (Figure 3.32). All the dark holes left within the image are somehow connected to the surface of the aggregate particle. Figure 3.32 is a 2D cross-sectional view, but the pores are 3D and protrude to the surface in a location different than in the slice being viewed.

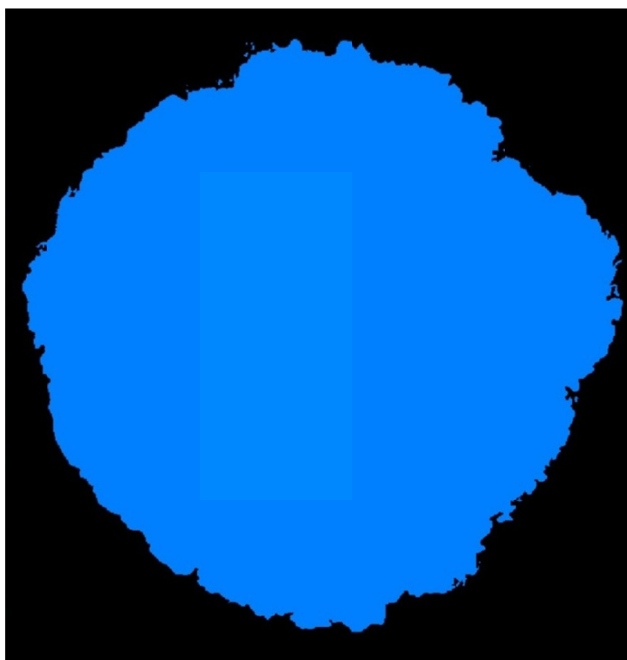


**Figure 3.31: Image of aggregate with all pores filled used for masking**

The binary image of the material (Figure 3.25) can then be subtracted from the image with the isolated holes filled (Figure 3.32) using a “logical sub” command to produce an image of only the isolated voids (Figure 3.33).

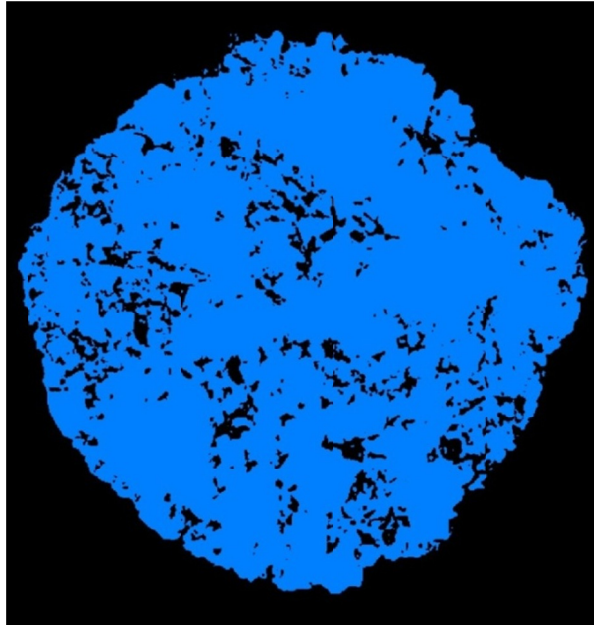


**Figure 3.32:** Image with isolated pores filled and only pores connected to the aggregate particle surface are present

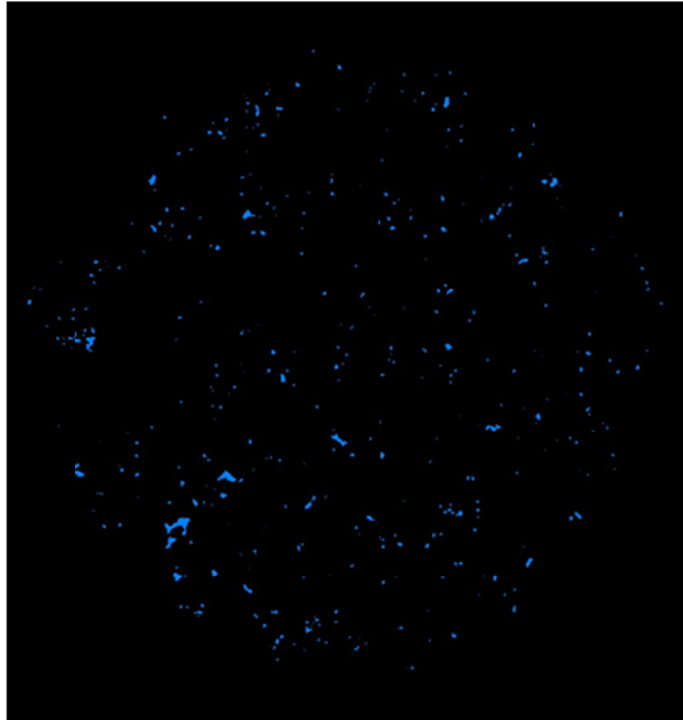


**Figure 3.33:** Image showing isolated pores obtained by steps described earlier

A masking command was used to isolate all of the pores within the image. Figure 3.26 (all pores plus background) was masked by the image in which all pores are filled (Figure 3.31) to separate the pores from the background. An image is created with only pores-no material or background is included (Figure 3.34). The isolated pores (Figure 3.33) are then subtracted from all the pores (Figure 3.34) to obtain the pores connected to the surface of the aggregate particle (Figure 3.35).

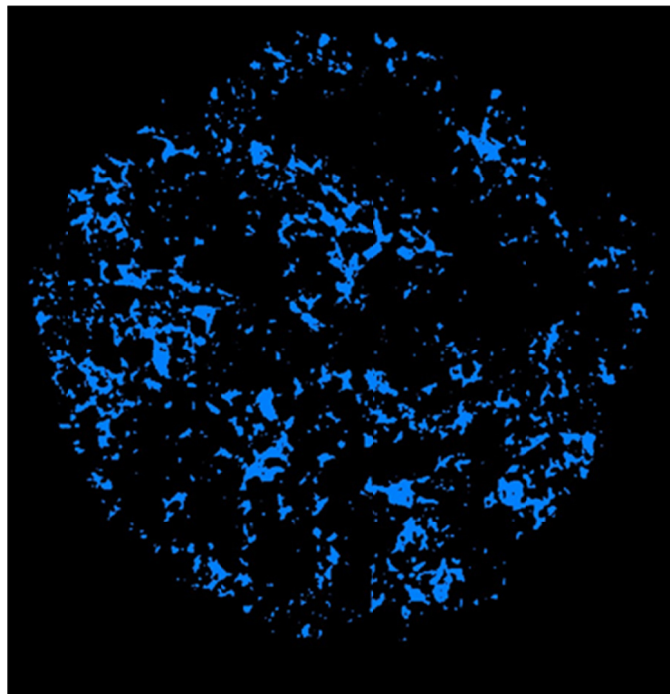


**Figure 3.34: Image displaying all pores of a cross section within an aggregate particle**

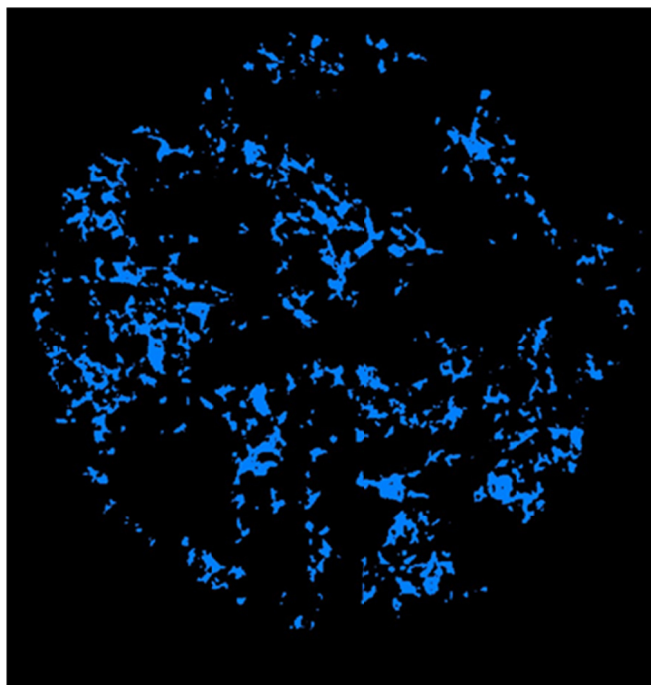


**Figure 3.35: Cross-sectional image displaying pores connected to surface of an aggregate particle**

There are three images that are of concern: the material solid (Figure 3.25), the isolated pores (Figure 3.33), and the pores connected to the surface (Figure 3.35). The images must be labeled before quantification. Labeling the image identifies each connected group of voxels and considers each group as one object. Avizo Fire® scans the image from top to bottom and left to right and each object is numbered. The objects are given one of nine colors in order of their numeration; once the ninth color is assigned, the next object in the list is given the first color again. Figure 3.36 shows the labeled isolated pores with different colors. Figure 3.37 shows an example of labeled pores which are connected to the surface. The majority of the pores are a single color, indicating they are connected somewhere within the aggregate particle.

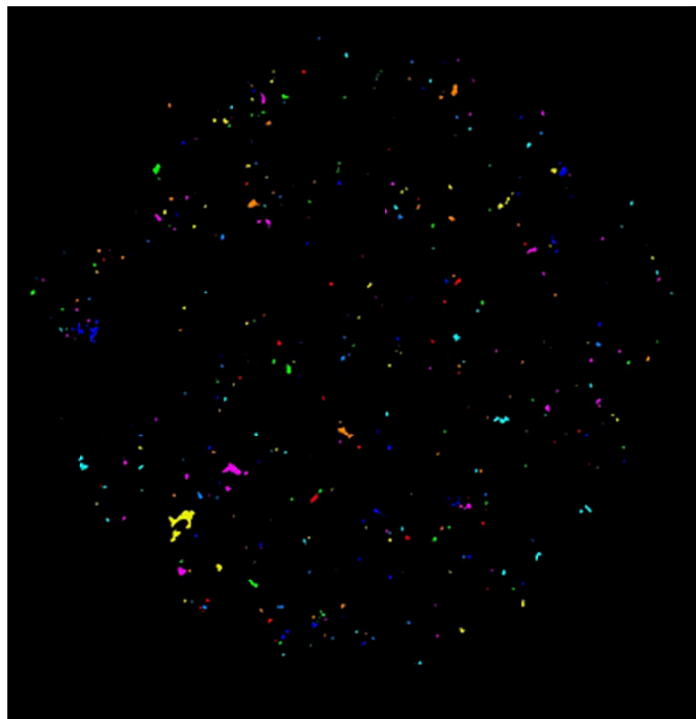


**Figure 3.36: Isolated pores separated and labeled for quantification**

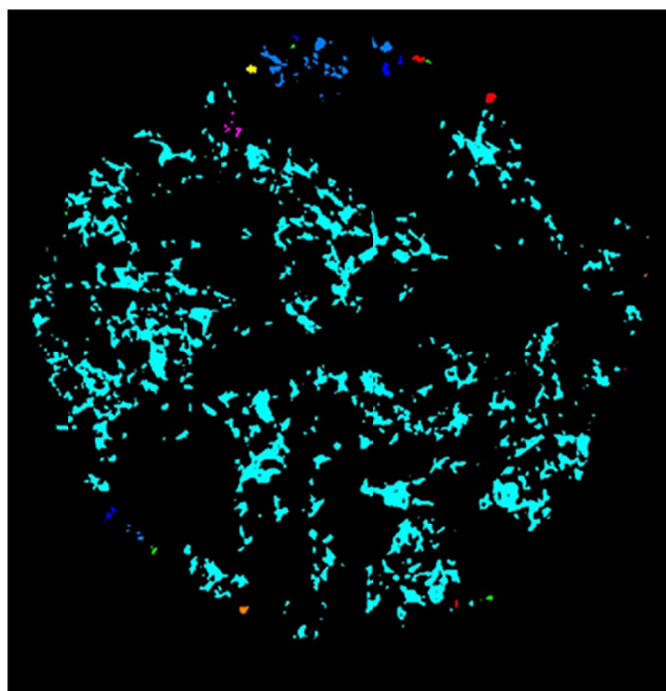


**Figure 3.37: Labeled pores that are connected to the aggregate surface**

### 3.4.3 Pore Space Measurements

The measurements of each individual object can be obtained. The Avizo Fire® program scans through the image and calculates measurements based on the properties of the binary images. The measurements include the volume, surface area, centroid of each object, length (in 3D), width (in 3D), and equivalent diameter. The volume is the sum of the volume of all of the voxels contained in the object. The surface area is that of the object boundary. The centroid is where the object is located within the XYZ space in Avizo Fire®. The length is the maximum Feret diameter of a circle that fits around the object. Length might not be a true representation of the actual pore length unless the pore is straight. The width is the minimum Feret diameter that fits around the object. Figure 3.38 shows the width and length of a pore. Equivalent diameter is the object's equivalent diameter of a circle. With these measures selected, the "I-Analyze" command in Avizo Fire® takes the measurements of all the individual objects within the image and provides the results in a table format, such as the one shown in Figure 3.39.

The porosity from the pores connected to the surface of an aggregate particle and the total porosity of the particle is calculated from the total volume of connected and isolated pores and total volume of solid aggregate material. The other measures also provide insight into pore geometry and structure.

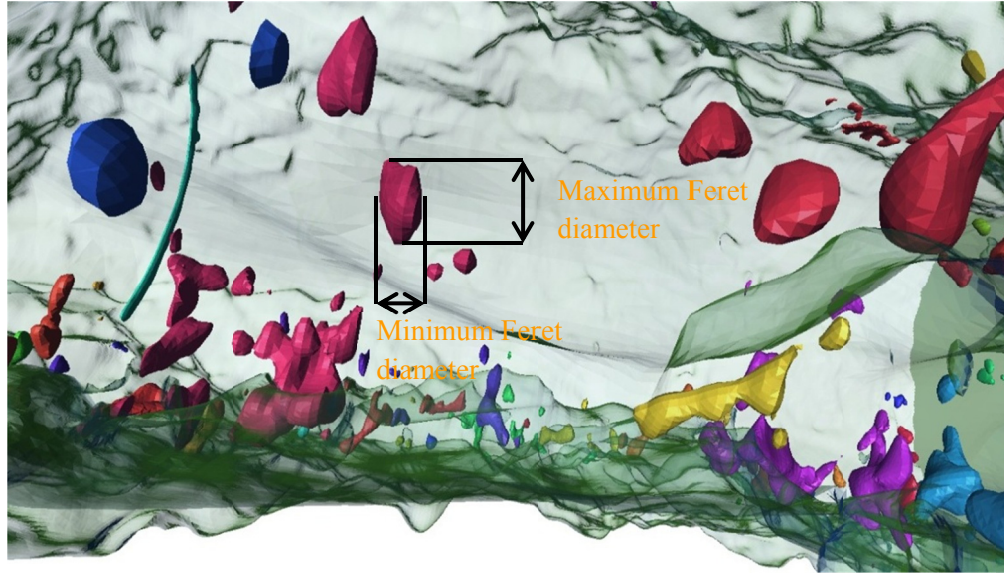


Figure 3.38: Width and length of a pore determined by Avizo Fire ®

Result Viewer - [Analysis GoC5Siso]

File Edit View Format Window ?

Nb objects : 28108

	B	C	D	K	L	M	N
1							
2		Volume3d (pixel^3)	Area3d (pixel^2)	Length3d (pixel)	Width3d (pixel)	EqDiameter 3d	index
3	1	686.0251	421.8548	24.09308	8.480001	10.94243	1
4	2	76.22501	54.00805	5.996265	5.996265	5.260573	2
5	3	228.675	145.0737	11.84493	4.24	7.587059	3
6	4	152.45	101.4212	8.47999	5.996265	6.627907	4
7	5	304.9001	182.1312	11.8449	4.24	8.350639	5
8	6	76.22501	54.00805	5.996265	5.996265	5.260573	6
9	7	76.22501	54.00805	5.996265	5.996265	5.260573	7
10	8	381.1251	228.618	12.71998	4.24	8.995454	8
11	9	457.3501	262.8413	14.71789	4.24	9.559096	9
12	10	914.7001	522.4372	25.44007	13.6239	12.04371	10

NUM

Figure 3.39: Measurements results viewer as outputted by Avizo Fire ®

### 3.4.4 Three Dimensional Visualization

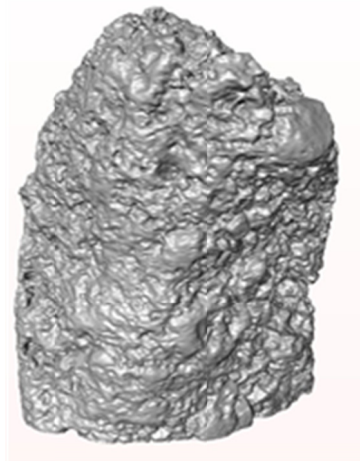
Lastly, a volume rendering of the pores and solid material is used to visually inspect the pore structure. An Avizo Fire® module computes a triangular approximation of the surfaces of objects. The “SurfaceGen” module is attached to the binary images of material and pores and creates their surfaces. Figure 3.40 shows the surfaces of two aggregates and the pores within the aggregates. The pore geometry can be viewed in 3D and provides useful insight on the internal structure of the aggregate particle. In Figure 3.40, aggregate (a) has many small isolated pores while, aggregate (c) has a highly interconnected tortuous pore structure. The 3D visualization provides useful information on pore connectivity, tortuosity, distribution, and size, which can be used to characterize aggregate behavior with respect to durability and ability to resist external forces from environmental impact and loading.



(a) 3D surface generation of an aggregate



(b) 3D surface generation of pores within the aggregate



(c) 3D surface generation of an aggregate



(d) 3D surface generation of pores within the aggregate

**Figure 3.40: 3D rendering from CT scans on aggregate particles that show two different types of pore distribution within an aggregate particle**

## Chapter 4

### Analyses of Results

This chapter presents the results of the 3D computed tomography imaging analysis of the investigated aggregates. The construction of 3D images of virgin aggregates and aggregates subjected to sodium sulfate soundness and freeze-thaw tests is presented, along with the quantitative analysis of pore space within the investigated aggregates, including total, connected, and isolated pores. Computed tomography imaging analysis results for treated aggregates are also explained in terms of physical characteristics of aggregates and durability against degradation/disintegration.

#### **4.1 Goldberg Aggregate – Limestone**

Seven Goldberg aggregate samples were scanned during the first trip to the Advanced Photon Source. One virgin sample was scanned and then subjected to two test cycles of sodium sulfate soundness, and then scanned again. In addition, this sample was subjected to three more test cycles of sodium sulfate soundness before scanning for the third time. Due to the limited time available for scanning at the Advanced Photon Source facility, wetting/drying cycles were limited to two hours each. This aggregate sample is termed as “scan on the same.” Furthermore, aggregates with one, two, three, four, and five test cycles of sodium sulfate soundness, conducted according to the AASHTO T104 procedure, were scanned. The resolution of the images was 4.24  $\mu\text{m}/\text{voxel}$ .

Virgin aggregate samples were scanned and analyzed to obtain reference information on pore space distribution on non-treated aggregates. Sodium sulfate soundness and freeze-thaw tests induced changes to the aggregate particles, including breakdown and degradation of the aggregate structure. Three-dimensional images of aggregate samples subjected to sodium sulfate soundness or freeze-thaw tests are analyzed and compared with the virgin aggregate of each type.

Figures 4.1-4.12 show CT constructed 3D images and slices for Goldberg aggregate samples subjected to zero (virgin), one, two, three, four and five test cycles of sodium sulfate soundness, as described by AASHTO T104 procedure. Figure 4.1 shows the 3D view of the pore space within a Goldberg virgin aggregate. The 3D image shows two types of pore space: isolated pores within aggregate solid that are not connected to the external surface, and pores that are connected to other pores and to the external surface of the aggregate particle. The virgin Goldberg limestone aggregate possesses a pore structure that is uniformly distributed within the aggregate mass, and the size of the pores are relatively small. Referring to Figure 4.1, the pores that are connected to the surface of the aggregate are colored in blue and the pores that are isolated within the aggregate solid are colored in orange. Inspection of the 3D image and cross-sectional slices indicates the presence of small cracks located near the surface of the aggregate, as depicted in Figure 4.2. It is observed from the images that the pores within the virgin aggregate are irregularly shaped and have no apparent pattern.

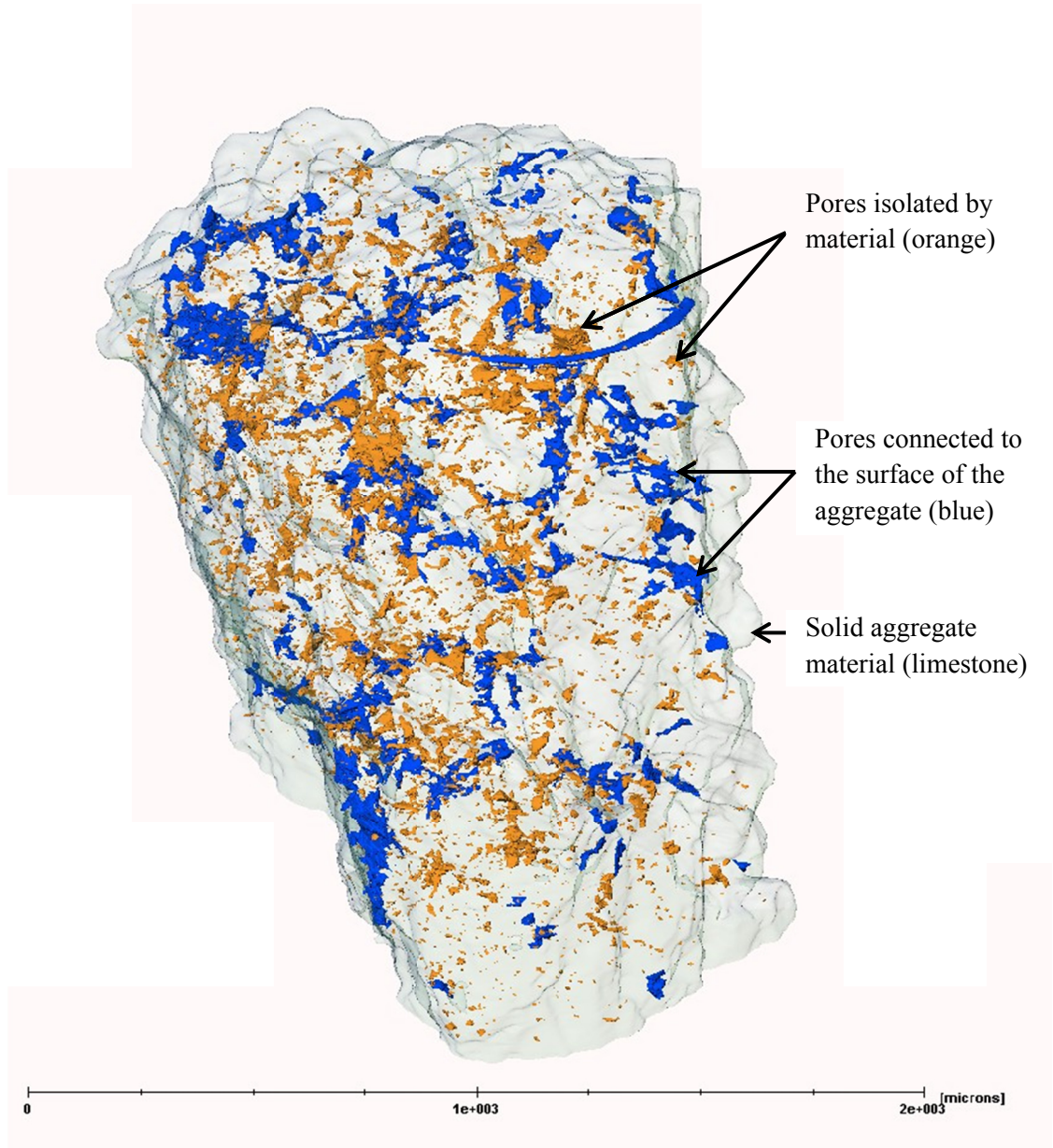


**Figure 4.1: CT constructed 3D image of the virgin Goldberg aggregate sample**

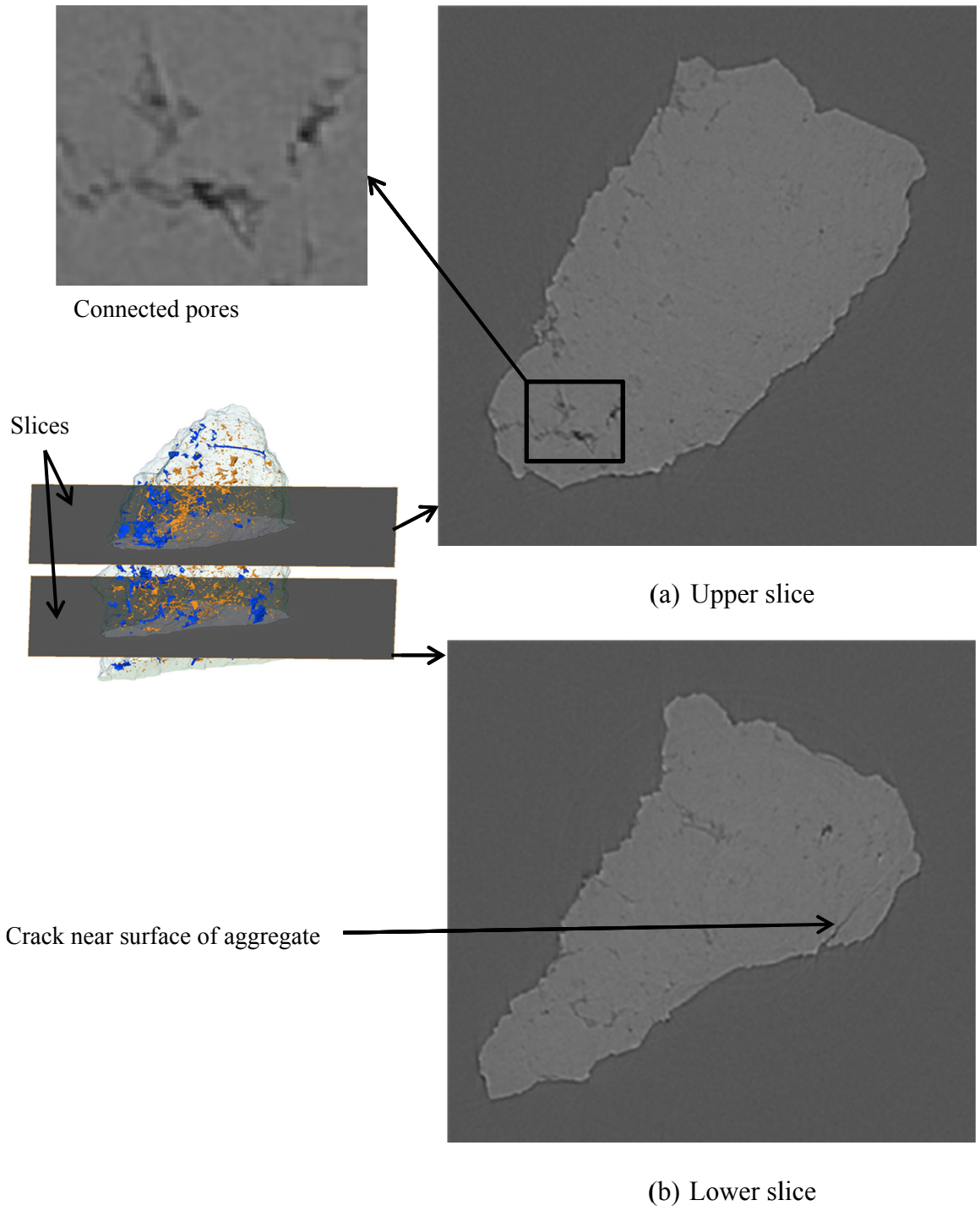


**Figure 4.2: Pore space and crack within cross-sections of Goldberg virgin aggregate**

As described in Chapter 3, the characteristics of pore space for the investigated Goldberg aggregate samples were measured. Each aggregate sample contains thousands of individual pores; therefore, pore space analysis was conducted using spreadsheets. The total volume of the solid material, volume of pores connected to the aggregate surface, and volume of isolated pores were measured and used to calculate the porosity of the investigated aggregate samples. The total porosity of the aggregate as well as the porosity of the aggregate in terms of the pores connected to the surface was calculated. The total porosity is calculated as:

$$n_T = \frac{V_V}{V_T} = \frac{V_V}{V_S + V_V} = \frac{V_{Vc} + V_{Vi}}{V_S + V_{Vc} + V_{Vi}} \quad (4.1)$$

Where  $n_T$  = the total porosity,  $V_V$  is the volume of all voids,  $V_T$  is the total volume of the sample, including solid material and voids,  $V_S$  is the volume of the solid material,  $V_{Vc}$  is the volume of the pores connected to the surface of the aggregate sample and  $V_{Vi}$  is the volume of the pores isolated within aggregate solid. The porosity of an aggregate particle considering pores connected to the surface ( $n_c$ ) is given by:

$$n_c = \frac{V_{Vc}}{V_S + V_{Vc} + V_{Vi}} \quad (4.2)$$

The porosity of the aggregate based on isolated pores ( $n_i$ ) is the difference between the total and connected porosities:

$$n_i = n_T - n_c \quad (4.3)$$

Equations 4.1 to 4.3 were used to calculate porosities of the investigated virgin and treated aggregate particles. Table 4.1 summarizes the results of aggregate solid and pore space volume measurements from 3D CT images and the corresponding porosities for all investigated aggregates. For Goldberg virgin aggregate particle, the total porosity of the sample is 1.0% and the porosity considering pores connected to the surface of the aggregate is 0.5%, as depicted in Table 4.1.

Figures 4.3 and 4.4 show a 3D CT constructed image of the Goldberg aggregate with one test cycle of sodium sulfate soundness (as described in Chapter 3). This sample possessed a significant number of pores near the surface, some of which are large. The increase in the number of pores and volume that is connected to the outside surface of the sample is the result of degrading material near the aggregate surface due to sodium sulfate treatment. The porosity of the aggregate considering the pores connected to the surface is 2.9% and the total porosity is 3.1% (Table 4.1). As depicted in Figure 4.3, pores that are connected to the surface of the aggregate are also highly connected to each other, indicating that thin solid barriers between pores may be degrading as the aggregate is subjected to wetting/drying sodium sulfate soundness test cycles. The connected (permeable) pores allow the penetration of the sodium sulfate during the wetting cycle. Internal expansion force develops due to re-hydration of the sodium sulfate upon re-wetting (after drying cycle) causing weathering/disintegration of solid material. Only 0.2% of the number of pores in this sample account for 90% of the total pore volume, which means there is a large number of small pores and a few very large-volume pores. The 3D image and slices show the aggregate has cracks near the surface, with a number of the cracks propagating within the aggregate. It was noticed the pores connected to the

**Table 4.1: Volume and porosity properties of the investigated aggregates**

Aggregate Type	Sodium Sulfate Soundness Cycle #	Volume ( $\mu\text{m}^3$ )				Porosity		
		Bulk Solid Particle	Total Pores	Connected Pores	Isolated Pores	Connected	Isolated	Total
Goldberg	Virgin	1,878,174,720	19,227,836	8,639,572	10,588,264	0.0046	0.0056	0.0101
Sodium Sulfate Soundness	1	4,432,906,240	143,069,771	133,372,502	9,697,270	0.0291	0.0021	0.0313
	2	14,628,932,608	431,051,936	151,046,880	280,005,056	0.0100	0.0186	0.0286
	3	4,548,087,296	165,165,040	83,682,104	81,482,936	0.0178	0.0173	0.0350
	4	9,901,642,728	1,401,499,604	1,347,489,536	54,010,068	0.1192	0.0048	0.1240
	5	9,193,993,216	1,180,359,968	1,062,797,760	117,562,208	0.1024	0.0113	0.1138
	2 on same	3,706,121,216	66,232,746	43,801,328	22,431,418	0.0116	0.0059	0.0176
	5 on same	2,860,262,912	90,479,169	74,604,472	15,874,697	0.0253	0.0307	0.0054
Kraemer	Virgin	2,585,366,528	25,751,780	18,279,748	7,472,032	0.0070	0.0029	0.0099
Sodium Sulfate Soundness	2 on same	36,207,220	445,958	338,599	107,359	0.0092	0.0029	0.0122
	4	35,265,540,096	1,100,607,641	405,885,380	694,722,261	0.0112	0.0191	0.0303
	5	7,370,570,340	960,383,832	901,352,064	59,031,768	0.1082	0.0071	0.1153
Larson	Virgin	7,504,349,184	509,997,112	410,523,776	99,473,336	0.0512	0.0124	0.0636
Sodium Sulfate Soundness	1 on same	6,435,641,344	495,835,344	412,333,280	83,502,064	0.0595	0.0120	0.0715
	2 on same	7,262,490,112	581,913,512	485,070,176	96,843,336	0.0618	0.0123	0.0742
	4	42,697,805,824	8,877,341,332	8,506,180,944	371,160,388	0.1649	0.0072	0.1721
	5	33,742,682,112	3,685,295,876	2,940,204,949	745,090,928	0.0786	0.0199	0.0985

**Table 4.1 (cont.): Volume and porosity properties of the investigated aggregates**

Aggregate Type	Sodium Sulfate Soundness Cycle #	Volume ( $\mu\text{m}^3$ )				Porosity		
		Bulk Solid Particle	Total Pores	Connected Pores	Isolated Pores	Connected	Isolated	Total
Ulland	Virgin	4,722,332,864	126,985,763	3,155,563	123,830,200	0.0007	0.0255	0.0262
Sodium Sulfate Soundness	2 on same	4,334,629,888	156,810,094	8,789,278	148,020,816	0.0020	0.0330	0.0349
	4	30,425,925,632	218,151,806	184,130,788	34,021,017	0.0060	0.0011	0.0071
Martin	virgin	4,972,979,200	50,915,025	45765263.3	5149761.279	0.0091	0.0010	0.0101
Sodium Sulfate Soundness	1 on same	7,950,942,720	157,484,114	150,548,456	6,935,658	0.0186	0.0009	0.0194
	2 on same	6,321,473,536	237,822,241	236,371,984	1,450,257	0.0360	0.0002	0.0363
Dane Lime	Virgin	85,932,072,960	1,794,968,335	527,251,126	1,267,717,209	0.0060	0.0145	0.0205
Sodium Sulfate Soundness	3	167,675,183,104	3,881,703,304	1,974,933,489	1,906,769,815	0.0115	0.0111	0.0226
	5	145,467,408,384	6,029,464,036	4,203,837,202	1,825,626,834	0.0277	0.0121	0.0398
Freeze-Thaw	30	132,142,784,512	11,694,446,604	10,503,694,723	1,190,751,881	0.0730	0.0083	0.0813
	45	127,043,305,472	9,936,707,871	8,506,180,944	1,430,526,927	0.0621	0.0104	0.0725
New Ulm	Virgin	3,060,306,688	114,412,532	95,181,260	19,231,272	0.0300	0.0061	0.0360
Sodium Sulfate Soundness	2 on same	3,156,571,136	122,351,283	103,663,727	18,687,557	0.0316	0.0057	0.0373
	4	66,438,393,856	4,467,674,899	4,223,308,907	244,365,992	0.0596	0.0034	0.0630

**Table 4.1 (cont.): Volume and porosity properties of the investigated aggregates**

Aggregate Type	Sodium Sulfate Soundness Cycle #	Volume ( $\mu\text{m}^3$ )				Porosity		
		Bulk Solid Particle	Total Pores	Connected Pores	Isolated Pores	Connected	Isolated	Total
Mich Light	Virgin	86,161,178,624	8,224,325,258	7,254,828,531	969,496,728	0.0769	0.0103	0.0871
	3	163,141,124,096	10,883,825,701	8,986,969,460	1,896,856,241	0.0516	0.0109	0.0625
	5	179,569,098,752	10,658,309,024	8,729,534,555	1,928,774,468	0.0459	0.0101	0.0560
Freeze Thaw	30	79,039,528,960	3,432,615,867	1,912,068,740	1,520,547,127	0.0232	0.0184	0.0416
	45	159,709,855,744	12,357,711,762	10,230,322,206	2,127,389,556	0.0595	0.0124	0.0718
Michigan	Virgin	7,741,865,472	340,719,872	241,422,992	99,296,880	0.0299	0.0123	0.0422
Sodium Sulfate Soundness	1 on same	9,502,771,200	523,031,568	346,138,240	176,893,328	0.0345	0.0176	0.0522
	2 on same	7,812,016,640	698,269,632	603,077,632	95,192,000	0.0709	0.0112	0.0821
	4	46,125,199,360	1,435,919,909	880,271,896	555,648,014	0.0185	0.0117	0.0302
	5	48,854,913,024	631,865,335	280,054,188	351,811,147.1	0.0057	0.0071	0.0128
Mich Dark	Virgin	92,781,764,608	325,494,837	212,961,860	112,532,976	0.0023	0.0012	0.0035
Sodium Sulfate Soundness	3	75,890,982,912	985,784,510	582,586,304	403,198,207	0.0076	0.0052	0.0128
	5	178,117,427,200	1,074,453,931	638,425,624	436,028,307	0.0036	0.0024	0.0060
Freeze Thaw	30	89,688,129,536	1,538,642,920	1,062,990,637	475,652,283	0.0117	0.0052	0.0169
	45	154,669,170,688	2,675,659,630	830,522,181	1,845,137,449	0.0053	0.0117	0.0170

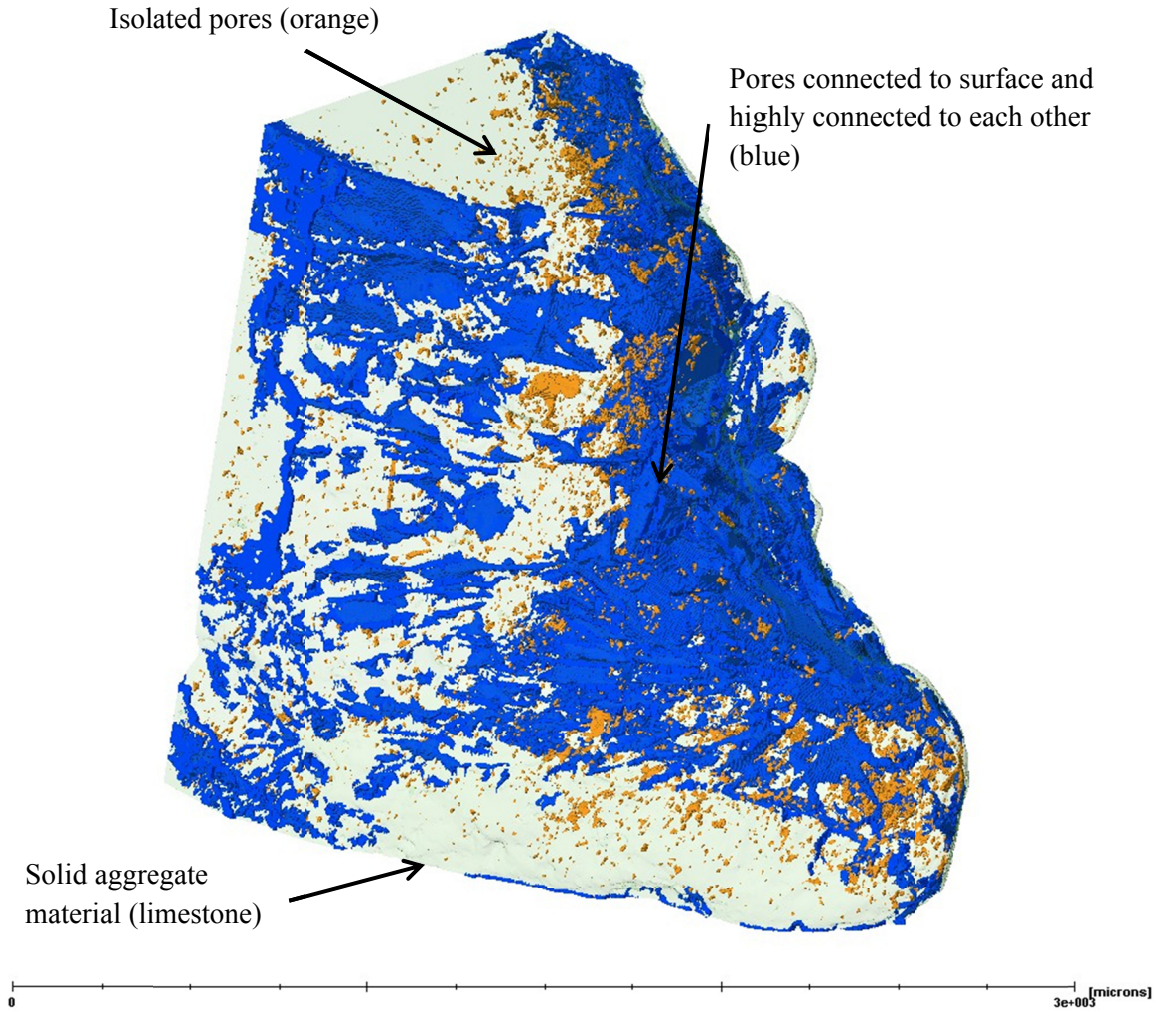


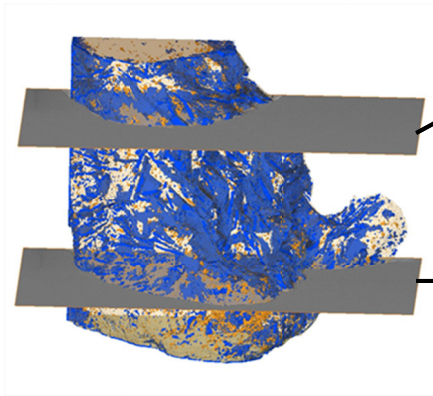
**Figure 4.3: CT constructed 3D image of Goldberg aggregate subjected to one test cycle of sodium sulfate soundness, 3.1% total porosity**



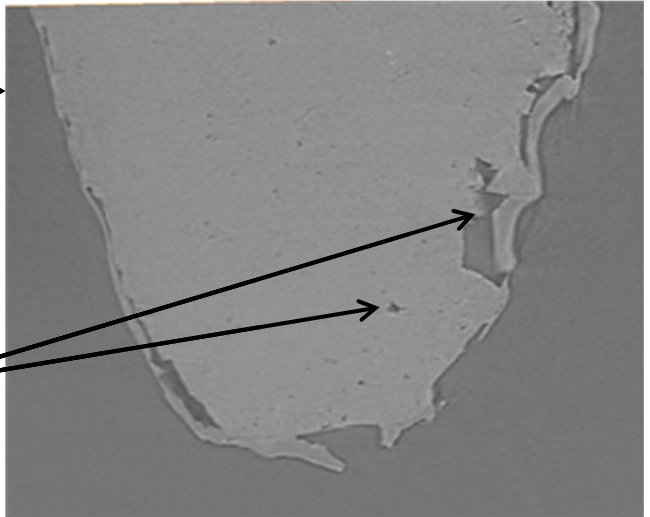
Propagating crack and angular pore connected to aggregate surface



(a) Upper slice



Angular shaped pores



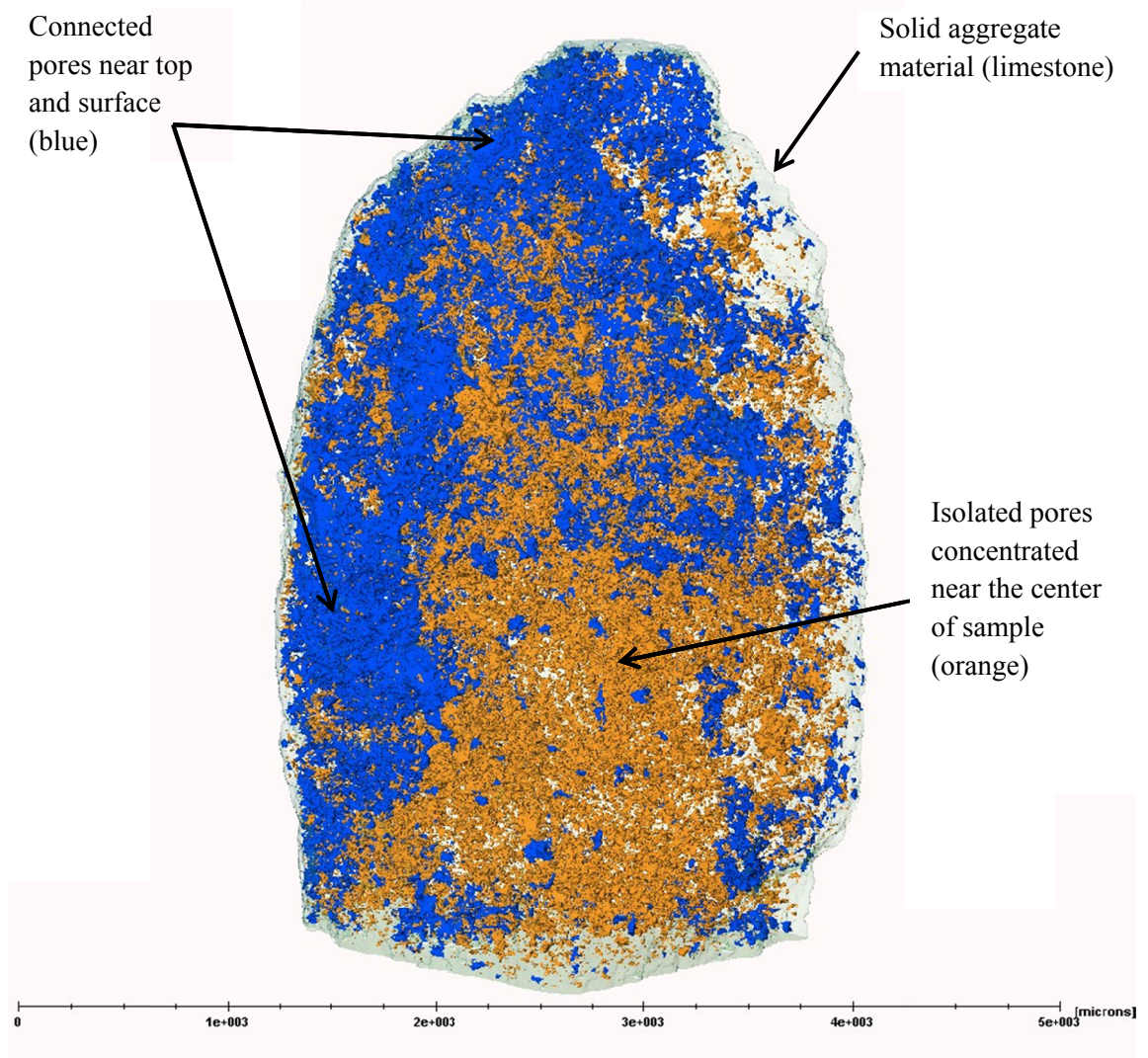
(b) Lower slice

**Figure 4.4: Crack and angular pores within cross-sections of Goldberg aggregate subjected to one test cycle of sodium sulfate soundness**

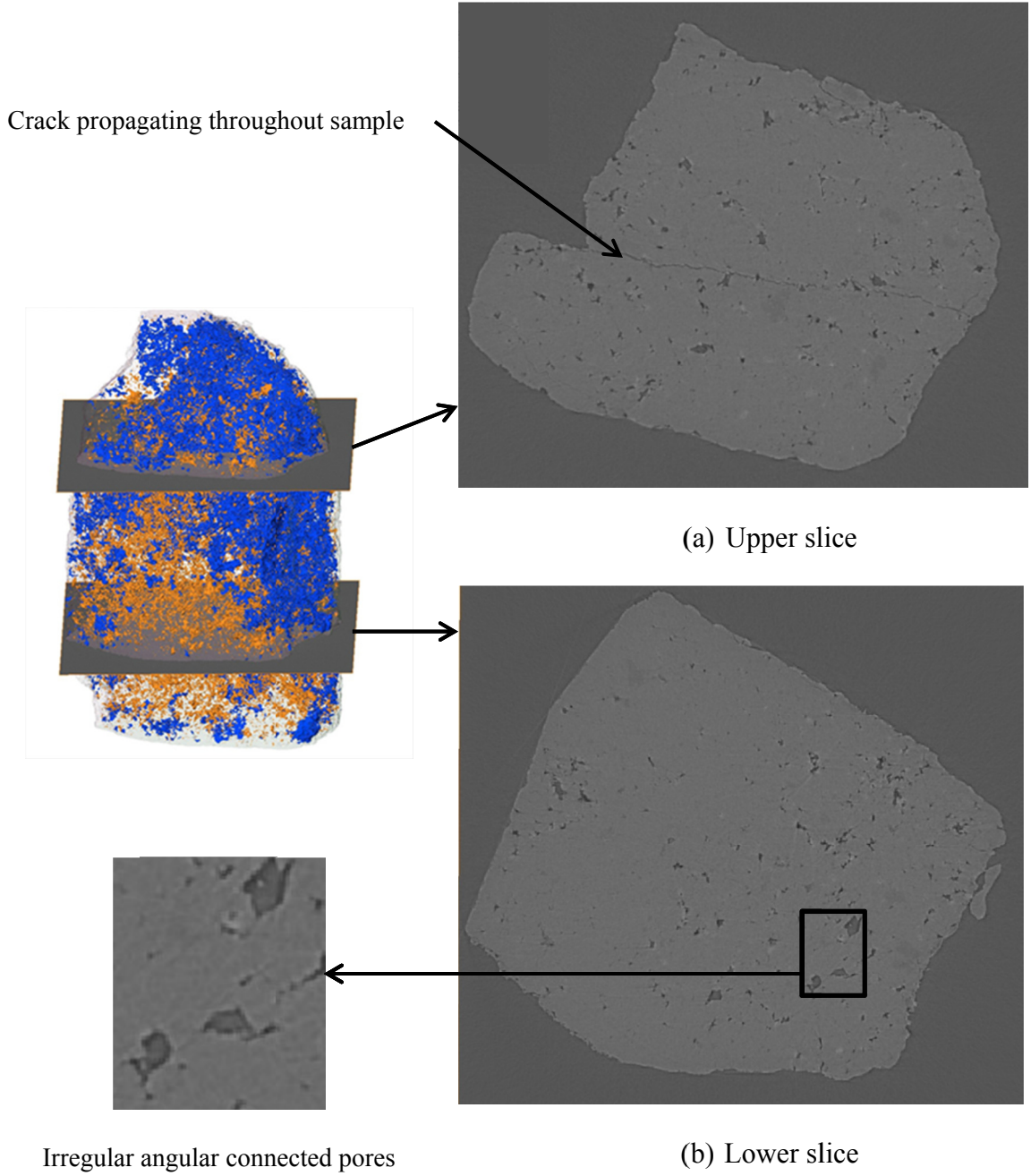
aggregate surface exhibit an angular shape, as shown in Figure 4.4 (b). In this aggregate particle, there is still a large number of small pores isolated within the aggregate, as depicted in Figure 4.3.

Figure 4.5 presents a 3D CT constructed image for an aggregate sample with two test cycles of sodium sulfate soundness, which has a connected porosity of 1.0% and total porosity of 2.9% (Table 4.1). As observed from the image, this specimen exhibited a larger number of pores connected to the surface and a few micro cracks that propagate throughout the entire particle, as depicted in the top slice of Figure 4.6. Inspection of Figure 4.5 illustrates how the pores connected to the surface after two test cycles reach farther into the center of the aggregate. This sample contains a higher concentration of isolated pores compared with the virgin sample and the sample with one test cycle of sodium sulfate soundness.

It should be noted these are different aggregate specimens within the same aggregate type (Goldberg); therefore, variability in pore space volumes and distributions is affected by the fact that specimens are different. The concentration of isolated pores near the center of the aggregate is greater than that near the top of the aggregate (Figure 4.5), while there are more pores connected to the aggregate surface at the top. This could be a result of the pores and cracks propagating near the top of the sample while it takes longer for the pores to propagate into the center. The cracks are more likely to propagate and connect pores near the surface of the sample with less effort because there is less confinement near the surface, while the center is well-confined all around.



**Figure 4.5: CT constructed 3D image of Goldberg aggregate with two test cycles of sodium sulfate soundness, 2.9% total porosity**



**Figure 4.6: Cross-sections of Goldberg aggregate with two test cycles of sodium sulfate soundness showing crack through entire sample and angular pores**

Quantitative porosity analysis is presented in Table 4.1 and discussed later in this Chapter to provide a rational measure for comparison. Some of the pores are irregularly shaped, similar to those observed in the virgin specimen. These irregular pores tend to be isolated within the aggregate solid. The pores connected to the surface exhibited irregular angular shape.

Referring to Figure 4.7, the aggregate with three test cycles of the sodium sulfate soundness exhibited a significant increase in the size of the cracks within the aggregate, but the number of pores connected to the surface was less than that in the sample with two test cycles of sodium sulfate soundness. The total porosity of 3.5% of the aggregate subjected to three sodium sulfate cycles was larger than the aggregate that was subjected to two sodium sulfate cycles of 2.9%. One large crack was observed throughout the specimen, as shown in Figures 4.7 and 4.8. There is an indication of pitting of localized regions within the aggregate near pores that are connected to the surface. Many of the pores connected to the surface are irregularly shaped, angular, and distributed more near the sample center. The isolated pores irregularly shaped are fairly evenly distributed where the connected pores have not yet reached.

The pores connected to the surface of the aggregate with four test cycles of sodium sulfate soundness dominate throughout the entire aggregate particle, as presented in Figure 4.9. The porosity of the aggregate particle considering pores connected to the surface is 11.9% and the total porosity of this aggregate is 12.4%. Very few distinct cracks were observed, while the pores connected to the surface exhibited a pattern of angular shape in a highly connected network; the slices in Figure 4.10 demonstrate the angularity of these pores.

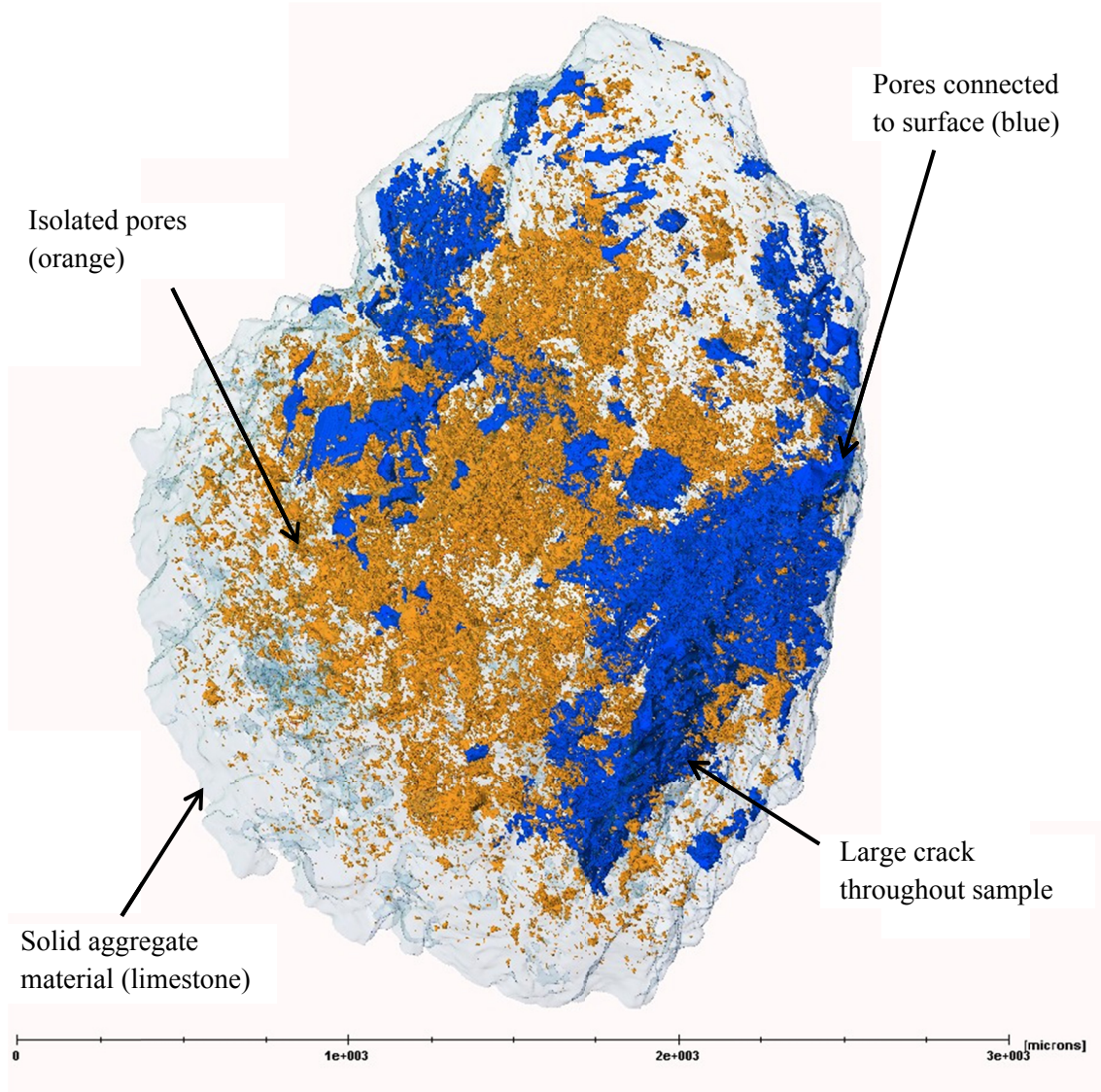


**Figure 4.7: CT constructed 3D image of Goldberg aggregate with three test cycles of sodium sulfate soundness, 3.5% total porosity**

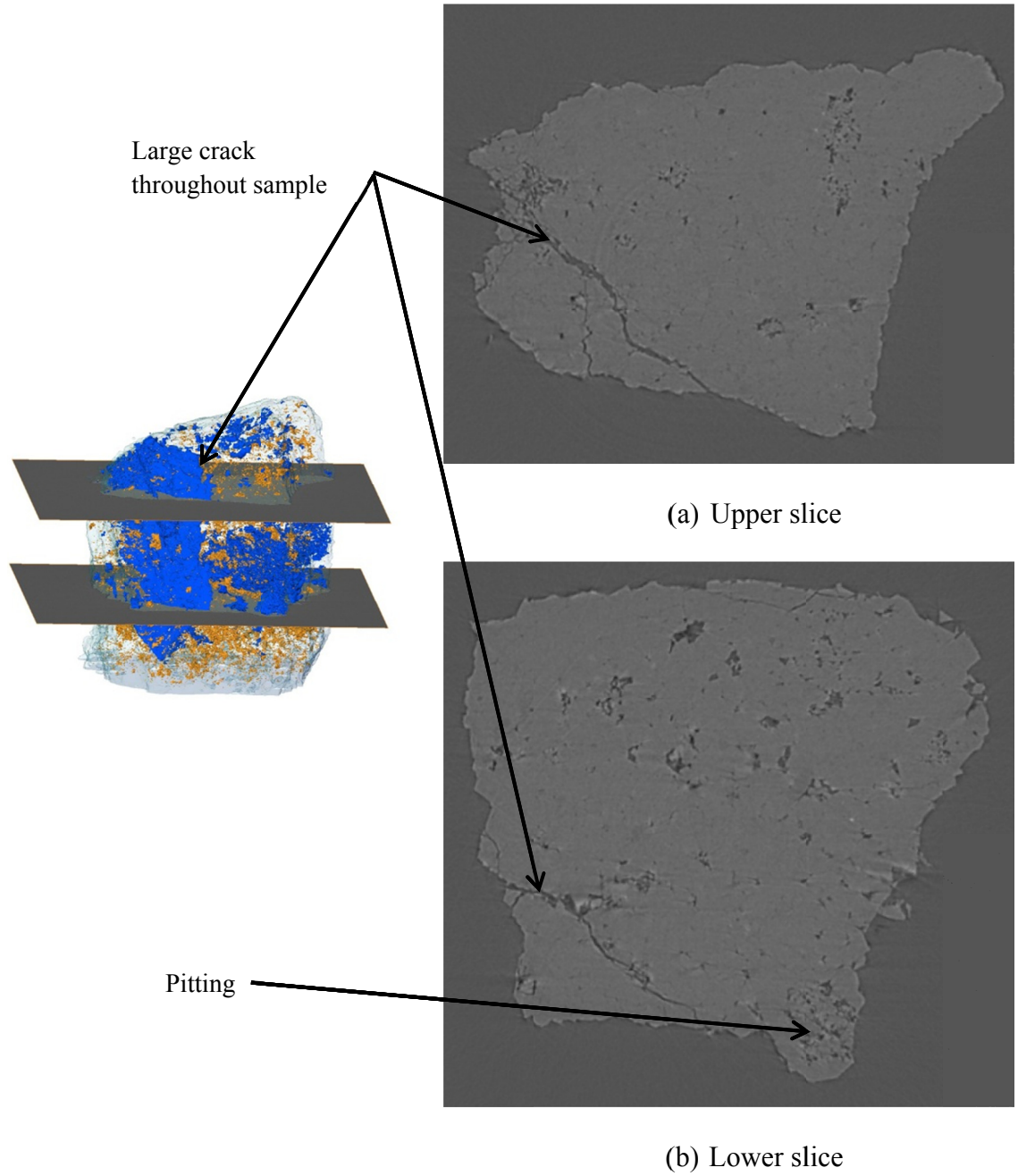


**Figure 4.8: Cross-sections of Goldberg aggregate specimen with three test cycles of sodium sulfate soundness showing crack throughout entire particle**

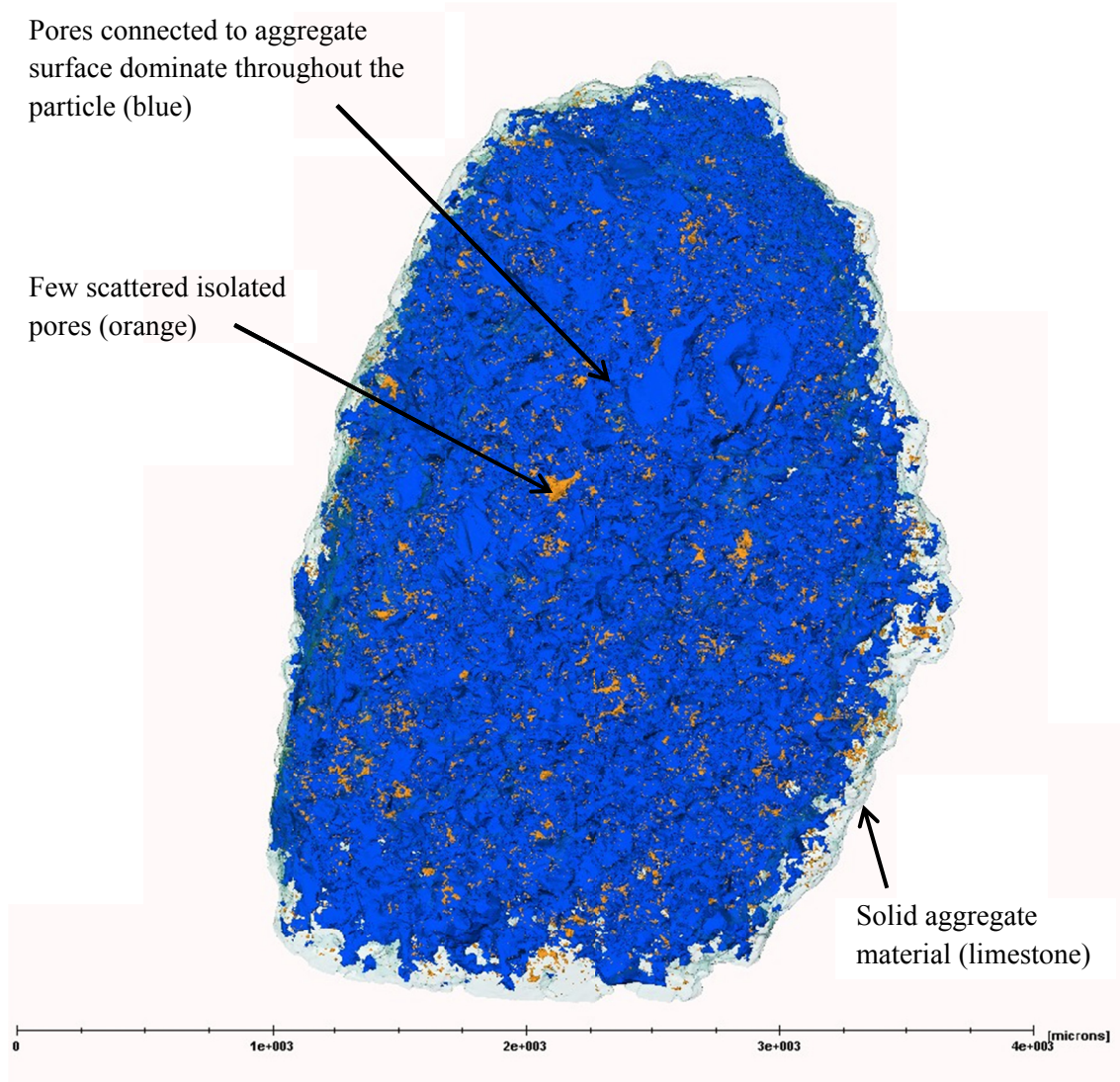


**Figure 4.9: CT constructed 3D image of Goldberg aggregate with four test cycles of sodium sulfate soundness, 12.4% total porosity**

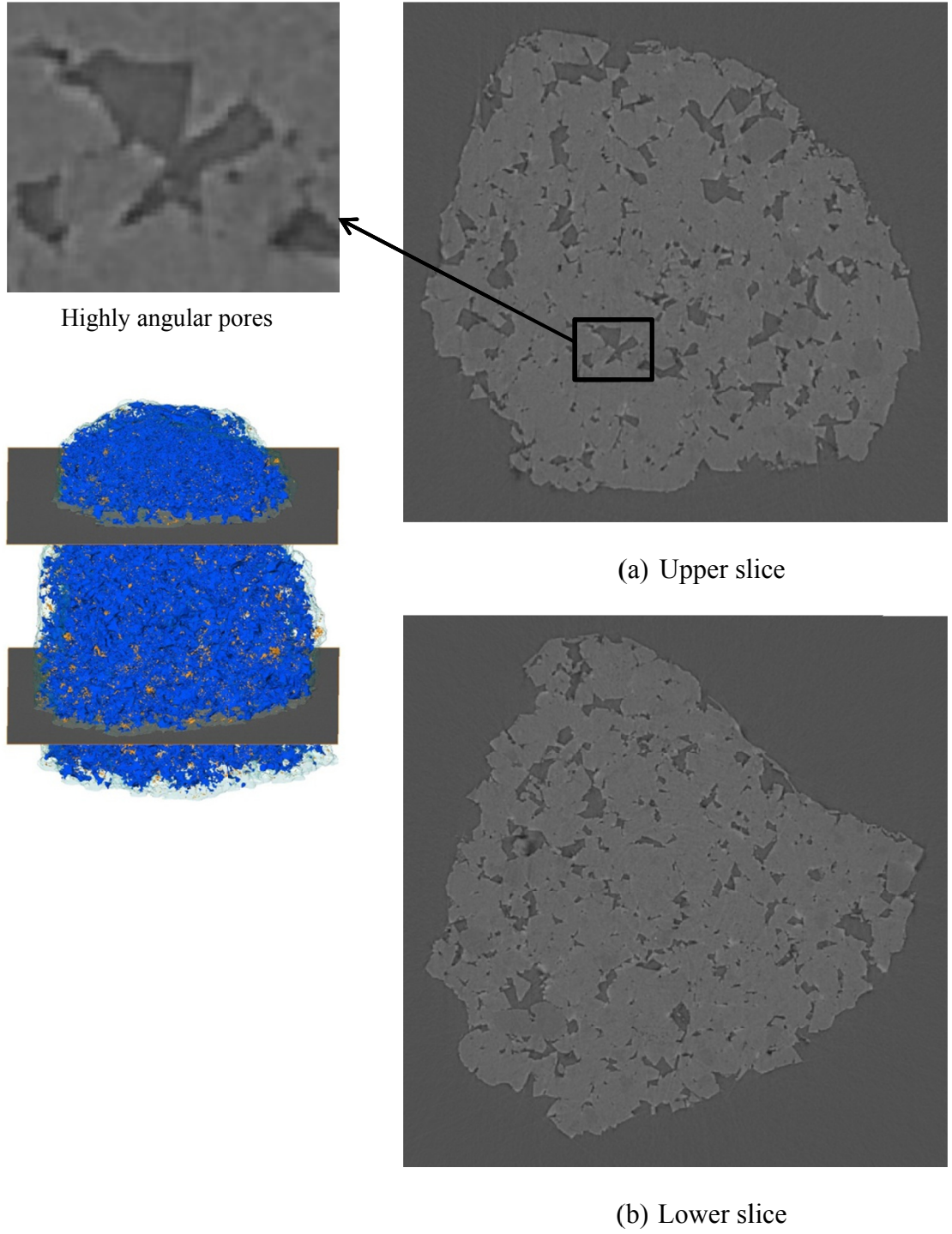


**Figure 4.10: Cross-sections of Goldberg aggregate with four test cycles of sodium sulfate soundness showing large highly angular pores**

The connected pores are evenly distributed throughout the entire sample and only a small percentage of the pores are isolated within the aggregate. Furthermore, the pores that are connected to the surface are highly connected to each other. One of the connected pores consists of 94% of the total volume of the pores within this sample, which means the majority of the connected pore space is considered a single connected, highly tortuous pore, as shown in Figure 4.9.

The aggregate sample with five test cycles of sodium sulfate soundness did not exhibit a significant pore space compared with the sample with four test cycles of sodium sulfate soundness. The total porosity of this sample is 11.4%, which is less than the 12.4% total porosity of the sample that experienced four sodium sulfate soundness cycles. However, there was significant pitting and many large pores within the sample, as depicted in Figure 4.11. This could be explained by the variability of individual aggregates within the same batch. Figure 4.11 shows some concentrated areas of isolated pores, but the pores connected to the surface dominate most of the sample. The pores are highly connected and tortuous. The pores in the aggregate sample with five test cycles of sodium sulfate soundness are much more irregularly shaped and smaller than the pores in the aggregate particle with four test cycles, but are still angular, as shown in Figure 4.12.

Inspection of these images demonstrates the aggregates exhibit increasing porosity with the increase in the number of sodium sulfate soundness test cycles due to degradation, disintegration and weathering within the aggregate solids from sodium sulfate treatment. The degradation of the investigated aggregates from the sodium sulfate soundness testing is described later in this Chapter.

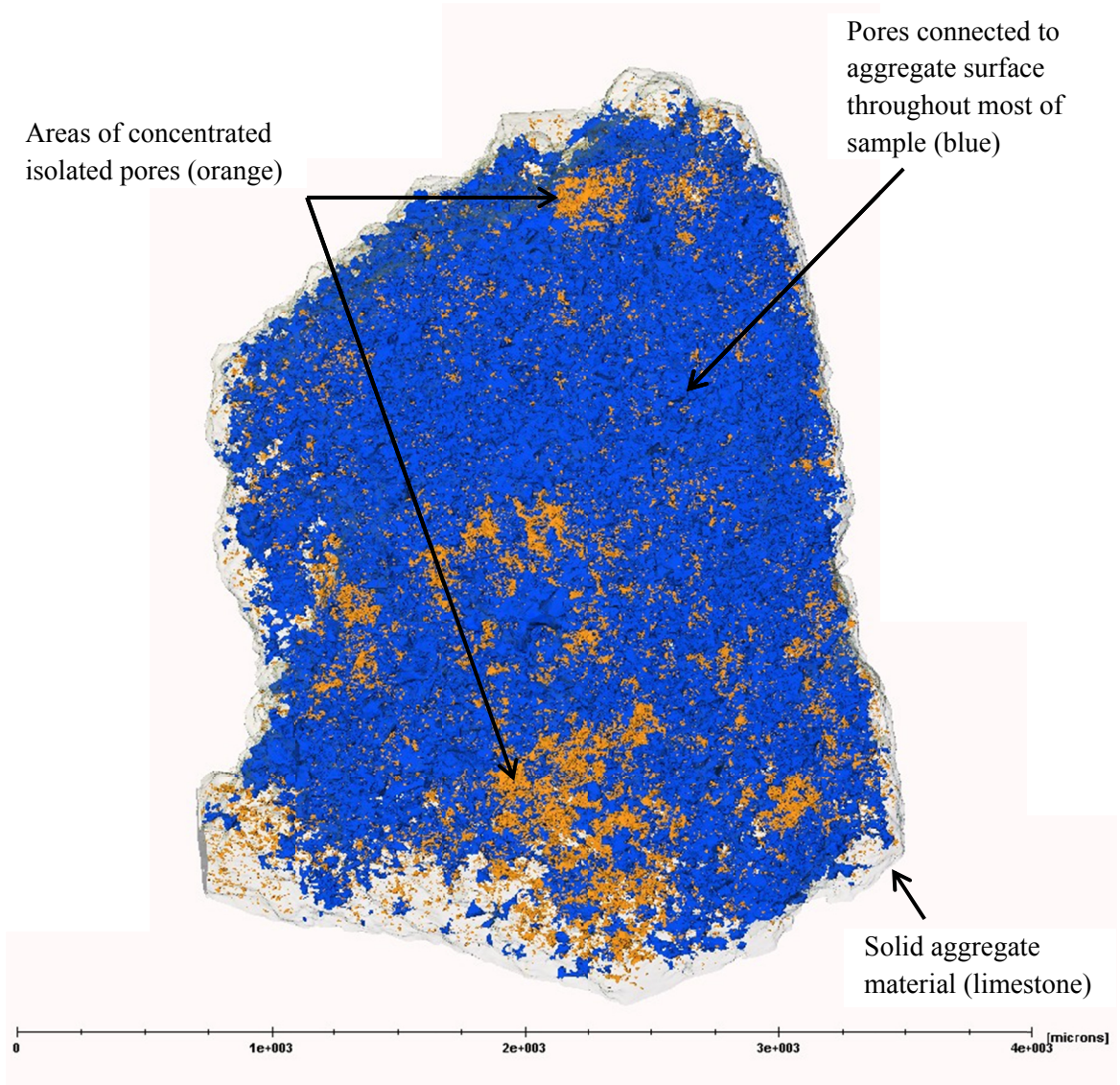


**Figure 4.11: CT constructed 3D image of Goldberg aggregate with five test cycles of sodium sulfate soundness, 11.4% total porosity**

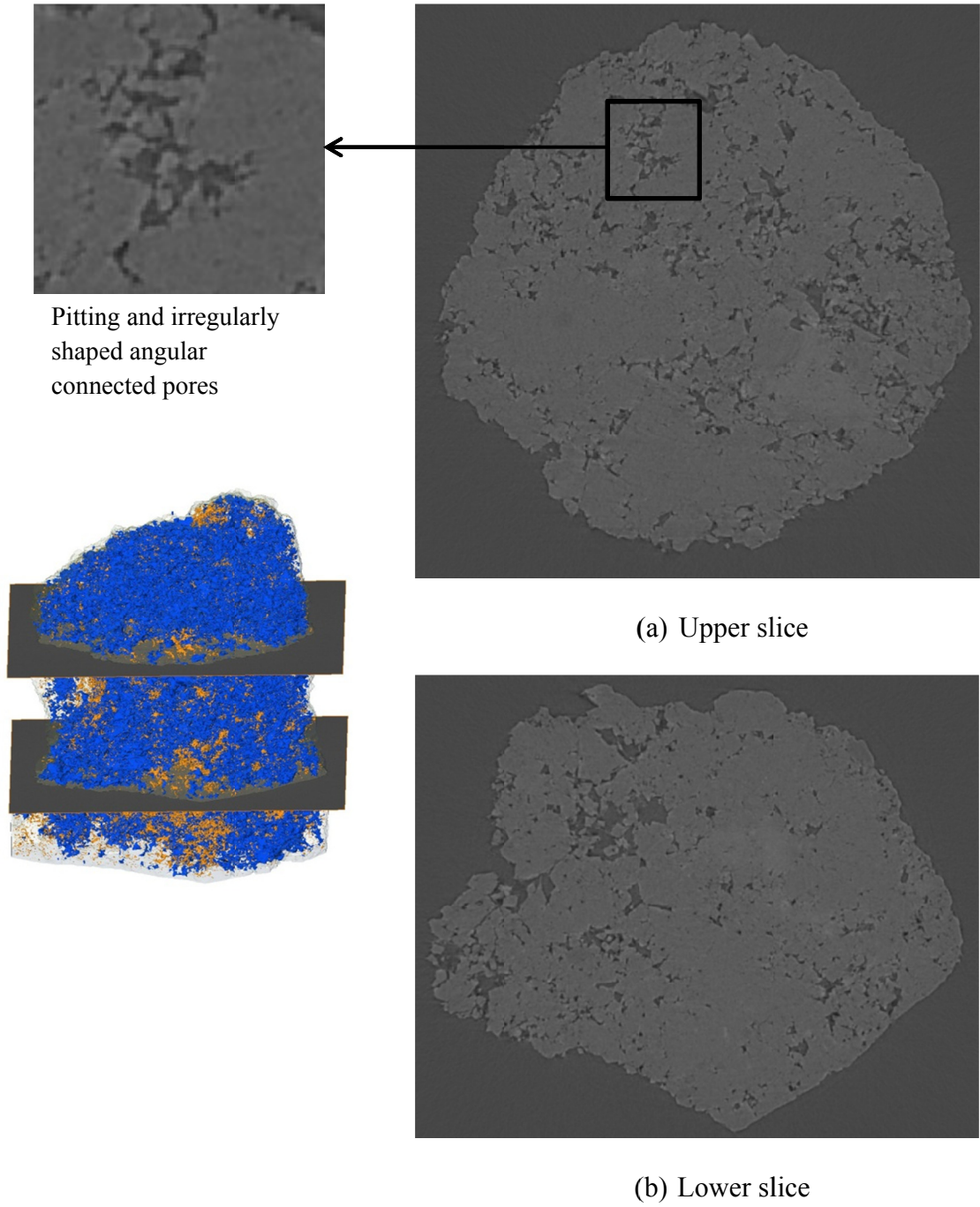


**Figure 4.12: Cross-sections of Goldberg aggregate particle subjected to five test cycles of sodium sulfate soundness showing irregularly shaped angular pores**

## 4.2 Pore Size Analyses

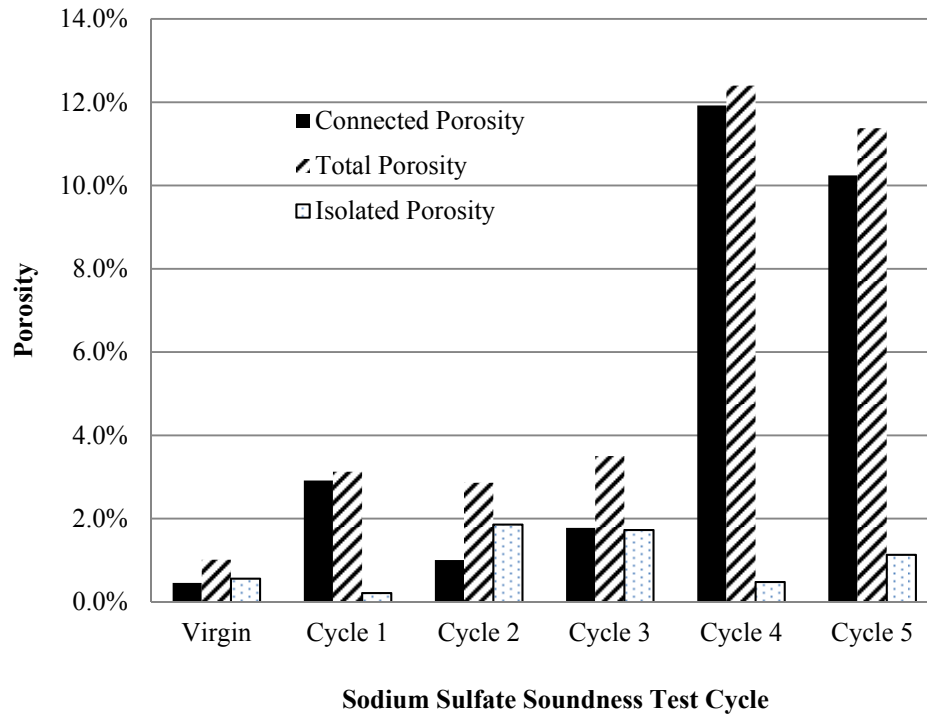
Volumes and porosities of the investigated Goldberg aggregate particles are summarized in Table 4.2. Figure 4.13 shows the variation of Goldberg aggregate porosities with the number of sodium sulfate test cycles. Figure 4.13 (a) presents the total porosity, porosity of aggregate particle with respect to pores connected to the surface and porosity of aggregate with respect to pores isolated within the particle solid of different aggregate samples at increasing test cycles of sodium sulfate soundness. On the other hand, Figure 4.13 (b) shows the increase in particle porosity with the increase in the number of sodium sulfate test cycles on the same aggregate. Test cycles of sodium sulfate soundness on the same aggregate demonstrate the increase of porosity of the particle with respect to pores connected to the surface of the aggregate, while the porosity of the particle with respect to the isolated pores remained unchanged.

Examination of Figure 4.13 (a and b) demonstrates that sodium sulfate soundness test has a significant influence on aggregate durability. Pores that are connected to the surface of the aggregate and also connected to each other (permeable pores) allow the penetration of the sodium sulfate during the wetting cycles. The internal expansion force, develops in pore space due to re-hydration of the sodium sulfate upon re-wetting (after drying cycle), causes weathering/disintegration of solid material such as the thin solid barriers between connected pores as illustrated in Figure 4.13 (c). This effect increases with the increase in the number of wetting/drying cycles. Therefore, the porosity when considering the connected pores (the total porosity also) increases with the increase of the wetting/drying cycles. Isolated pores will not be affected since sodium sulfate will not be able to penetrate these pores during the test time.

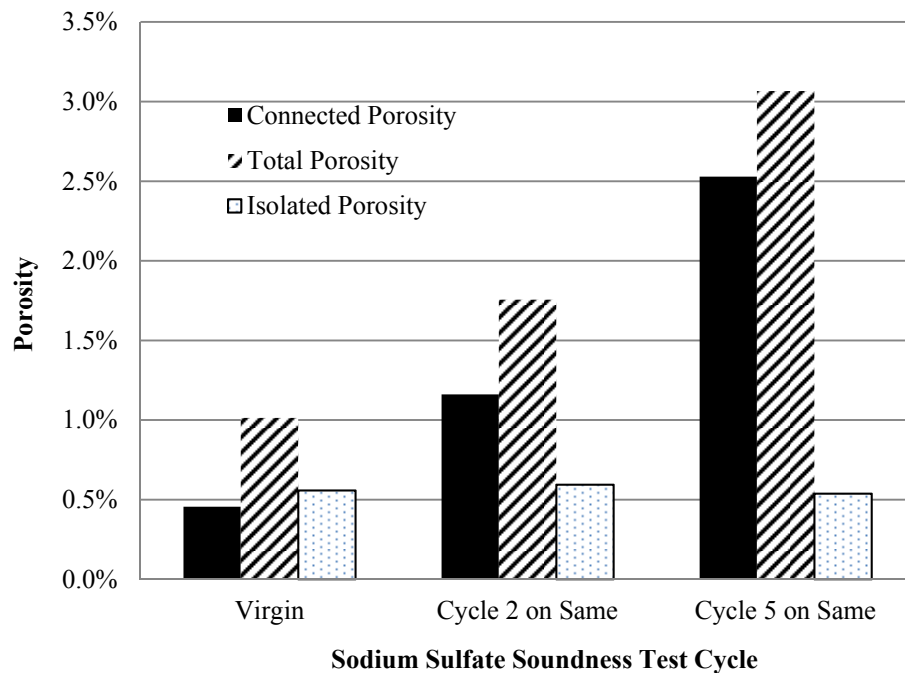
**Table 4.2: Volumes and porosities of Goldberg aggregates**

Description	Sodium Sulfate Soundness Treatment					
	Virgin	Cycle 1	Cycle 2	Cycle 3	Cycle 4	Cycle 5
Solid material (mm <sup>3</sup> ), $V_S$	1.87817	4.43291	14.62893	4.54809	9.90164	9.19399
Connected pores (mm <sup>3</sup> ), $V_{Vc}$	0.00864	0.13337	0.15105	0.08368	1.34749	1.06280
Isolated pores (mm <sup>3</sup> ), $V_{Vi}$	0.01059	0.00970	0.28001	0.08148	0.05401	0.11756
Connected Porosity, $n_c$	0.0046	0.0291	0.0100	0.0178	0.1192	0.1024
Total Porosity, $n_T$	0.0101	0.0313	0.0286	0.0350	0.1240	0.1138

The increase in aggregate porosity with the increase in sodium sulfate soundness test cycles is demonstrated in 2D slices, as presented in Figures 4.14 and 4.15. The slices in Figure 4.14 are nearly the same cross-sections of the same aggregate particle. The size of the aggregate pores connected to the surface of the aggregate in Figure 4.14 becomes larger with increasing sodium sulfate soundness cycles on the same aggregate. Figure 4.15 shows the degradation of the aggregate solid material with increasing sodium sulfate soundness test cycles for different aggregate particles. The wetting/drying sodium sulfate soundness test cycles on the same aggregate were time-constrained by the availability of the APS facility, and, therefore, do not show as much degradation as the aggregates subjected to the full wetting/drying sodium sulfate soundness test cycle, as shown in Figure 4.15. The slices in Figure 4.15, taken from different Goldberg aggregate particles, show the increase of the pore population and size as the number of test cycles increases.



(a) On different aggregate particles



(b) On the same aggregate particle

**Figure 4.13: Variation of Goldberg aggregate particle porosity with the number of sodium sulfate soundness test cycles**

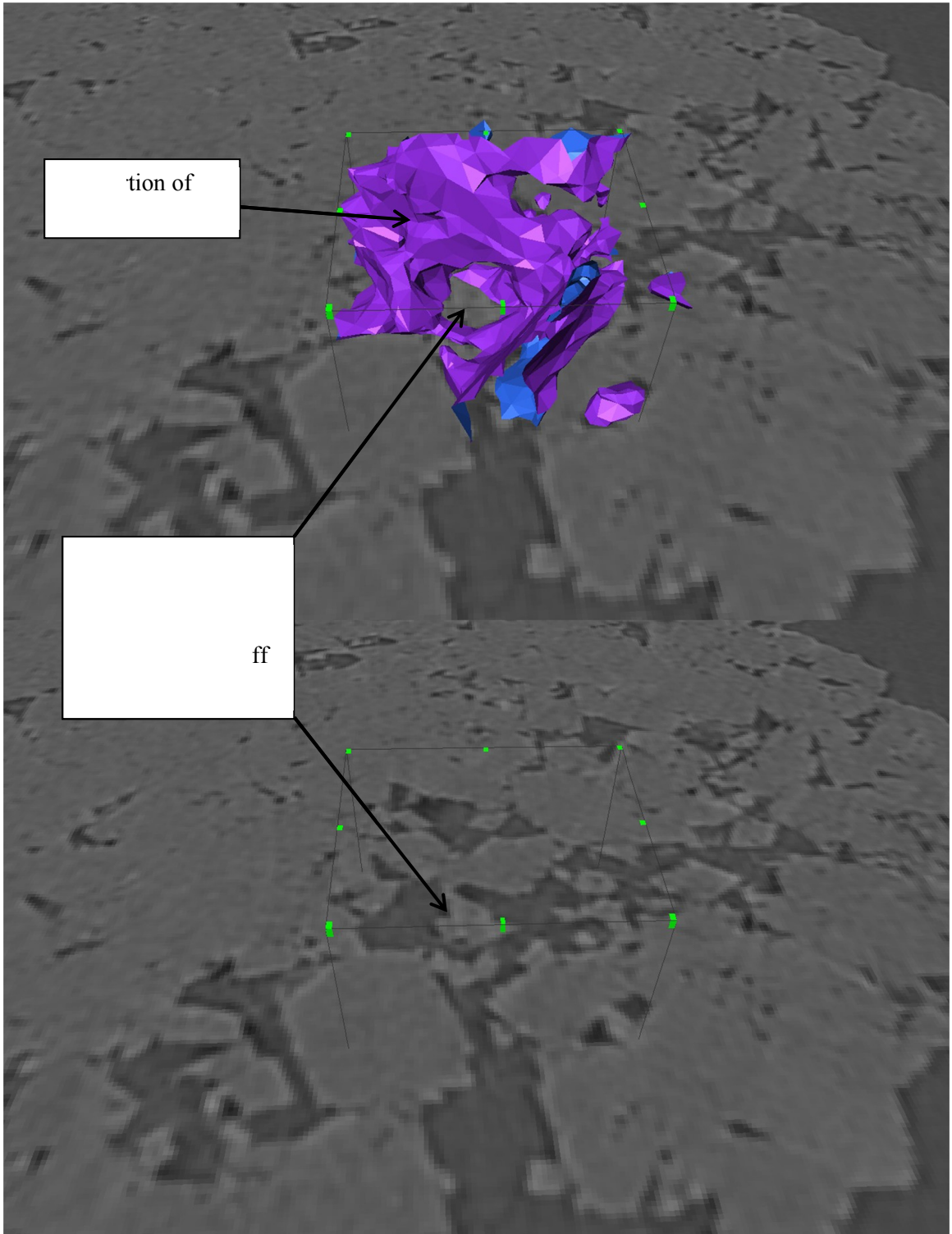
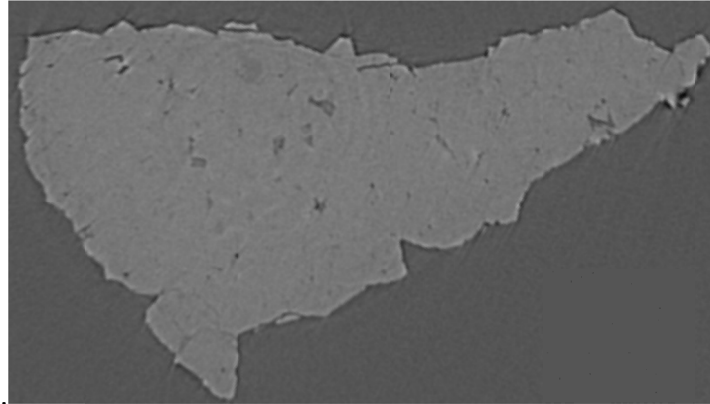
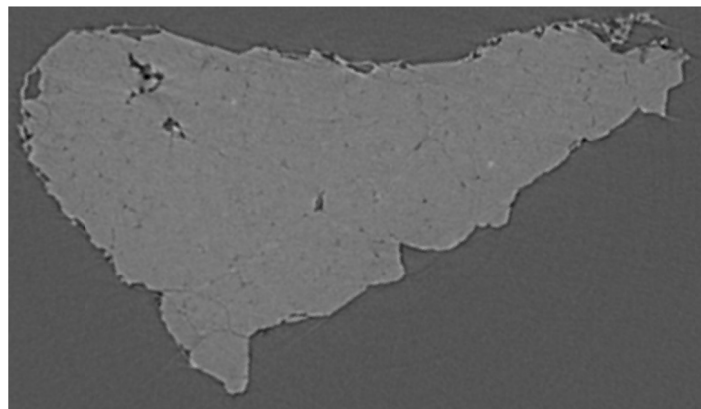


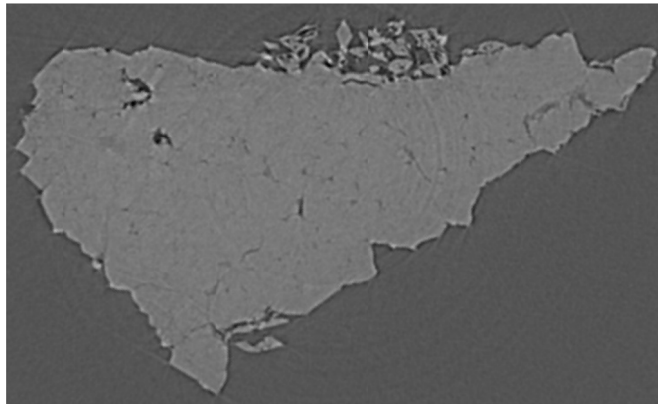
Figure 4.13 (c): 3D and 2D images of thin solid material between connected pores



(a) Goldberg virgin aggregate



(b) Goldberg aggregate after 2 sodium sulfate soundness cycles on the same aggregate



(c) Goldberg aggregate after 2 sodium sulfate soundness cycles on the same aggregate

**Figure 4.14: Cross-sectional tomographs demonstrating the degradation and increase in pore space near the surface of the aggregate due to wetting/drying test cycles from sodium sulfate soundness test on the same Goldberg aggregate particle**

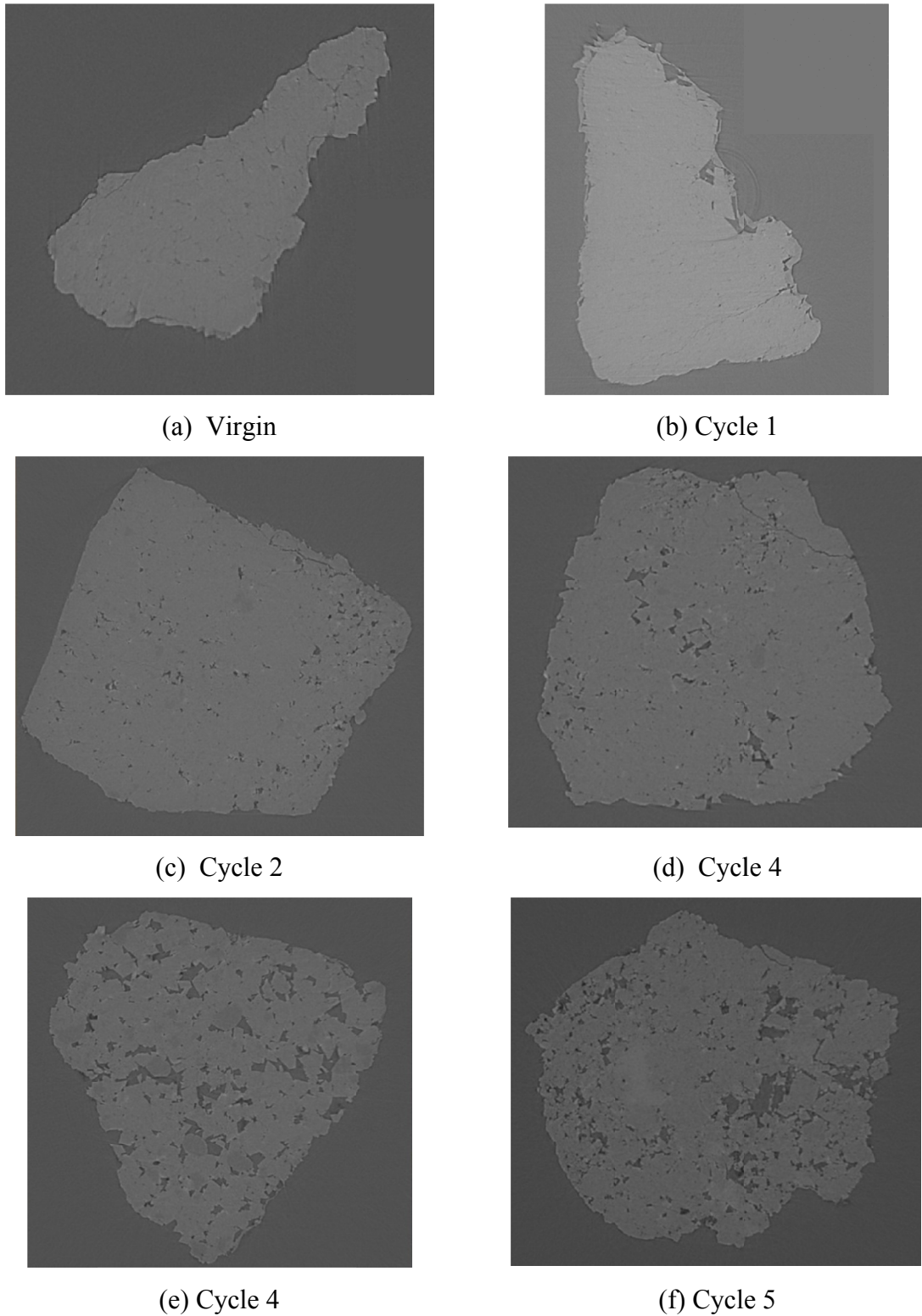


**Figure 4.15: Cross-sectional tomographs demonstrating the increase in pore space intensity and volume due to wetting/drying test cycles from sodium sulfate soundness test on different Goldberg aggregate particles**

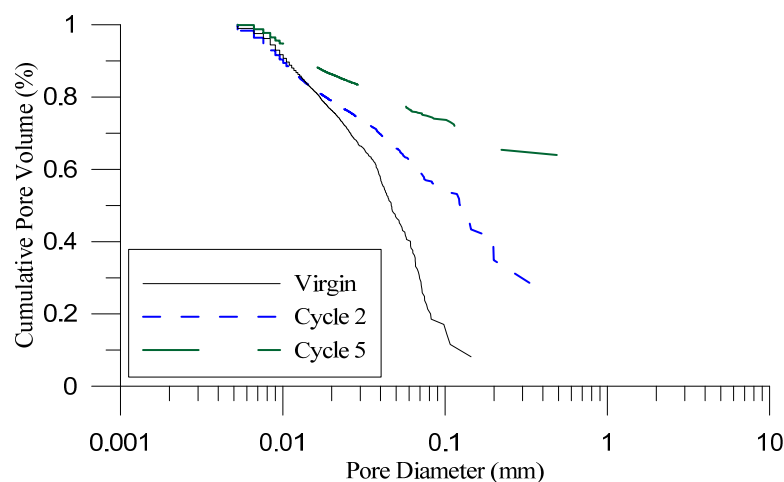
The volumes for pores both connected to the surface and isolated pores were analyzed. The general trend after each cycle indicated the most of the pore volume resulted from a smaller number of pores. This pattern shows that pores within the aggregate particles become more connected as the number of sodium sulfate soundness test cycles increase. During wetting/drying of the sodium sulfate soundness test cycles, the aggregates experience internal pressures and forces that lead to breakdown of thin solid barriers between pores; therefore, pore space volume increases. Micro-cracks also form within the aggregate and other degradation mechanisms such as pitting induced by the sodium sulfate soundness test, thereby creating more connectivity between the pores.

To further demonstrate the impact of wetting/drying cycles on the internal structure of aggregates, pore size distribution was analyzed by assuming all pores are spherical. Pore diameter corresponding with the pore size of a sphere was calculated for each pore detected by CT constructed images. Distribution of cumulative pore volume percent versus pore diameter was obtained for the aggregate particles subjected to cycles of sodium sulfate soundness test.

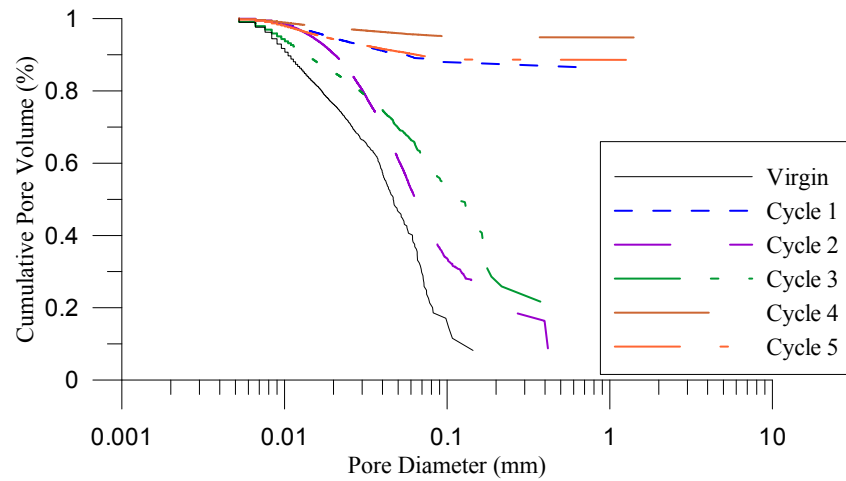
Figure 4.16 presents the pore size distribution curves for Goldberg aggregate subjected to different number of sodium sulfate soundness test cycles (0, 2 and 5). The graph shows that 100% of the pores have a diameter larger than 0.005 mm, which is the smallest pore detectable at the image resolution of the Goldberg aggregates. Inspection of the figure shows that pore space increases with the increase in wetting/drying cycles. As an example, for the aggregate particle under virgin condition, 70% of the pore volume is occupied by pores with a diameter greater than or equal to 0.023 mm ( $D \geq 0.023$  mm), while this pore diameter increases to greater than or equal to 0.039 mm ( $D \geq 0.039$  mm)

for the same aggregate particle when subjected to two cycles of sodium sulfate soundness test. In addition, when the same aggregate particle is subjected to five cycles of the sodium sulfate soundness test, the pore diameter corresponding with 70% of the total cumulative volume of pore space increases greater than or equal to 0.12 mm ( $D \geq 0.12$  mm).

Figure 4.17 presents the pore size distribution curves for discrete Goldberg aggregates at different cycles of sodium sulfate soundness testing. The same behavior/trend observed in Figure 4.16 occurs in Figure 4.17. It should be noted that for a high number of sodium sulfate soundness wetting/drying cycles, the deterioration of aggregate particles is significant. For example, 0.1 mm and larger pore diameter (i.e.,  $D \geq 0.1$  mm) corresponds with 17% of the cumulative pore volume of the virgin Goldberg aggregate, while the same pore diameter range ( $D \geq 0.12$  mm) corresponds with 98% of the cumulative pore volume for the Goldberg aggregated subjected to five test cycles of sodium sulfate soundness (Figure 4.16).

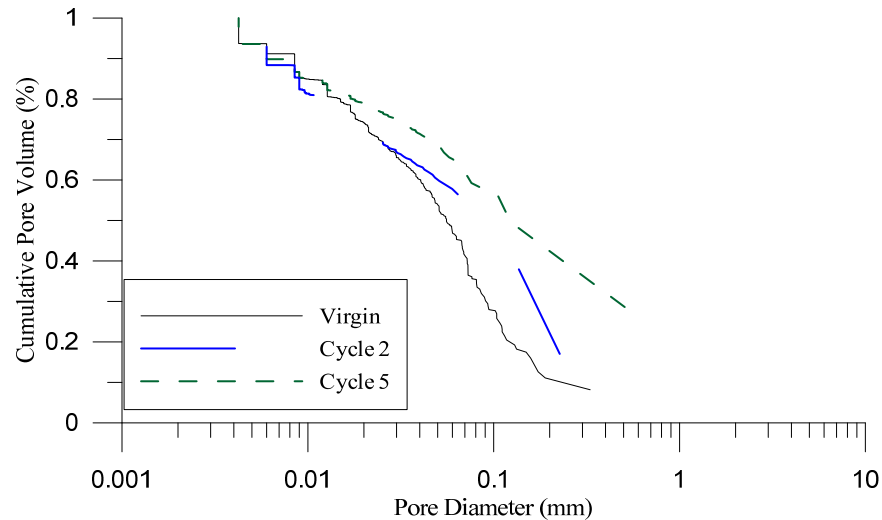


**Figure 4.16: The variation of pore size distribution with the number of wetting/drying cycles from sodium sulfate soundness tests on the same Goldberg aggregate particle**



**Figure 4.17: The variation of pore size distribution with the number of wetting/drying cycles from sodium sulfate soundness tests on different Goldberg aggregate particle using equivalent spherical diameter**

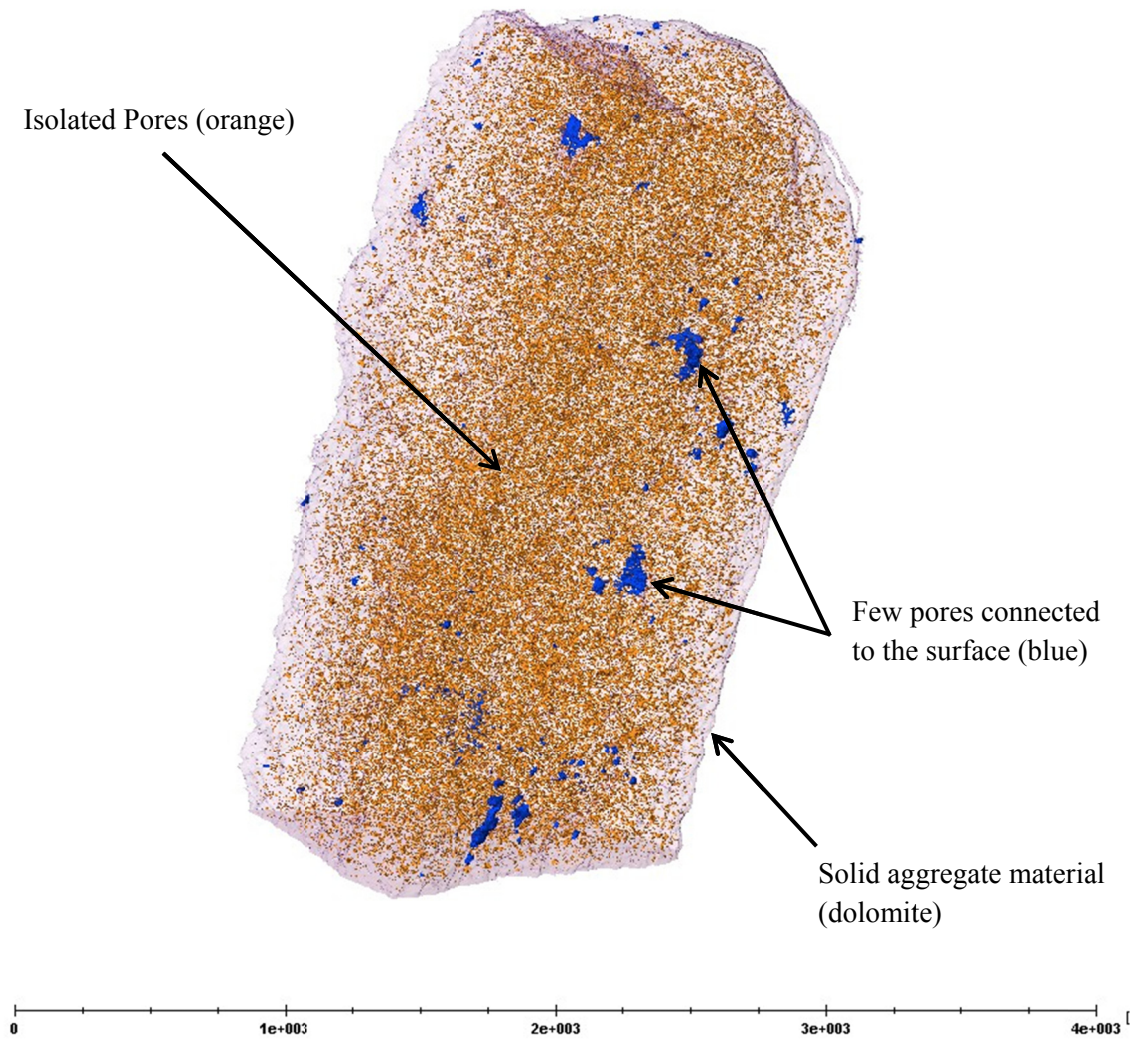
The width and length of all pores were also measured from the 3D CT images, as described in Chapter 3. The average aspect ratio (width/length) of the pores for all Goldberg aggregates was 0.64, which shows deviation from the spherical pore shape assumption. Therefore, the pore size distribution using the width was plotted as shown in Figure 4.18 to compare it with the pore size distribution using an equivalent spherical diameter. The pore size distribution, with the number of wetting/drying cycles from the sodium sulfate soundness test on the same Goldberg aggregate using pore width, displayed similar distributions to using equivalent spherical diameters.



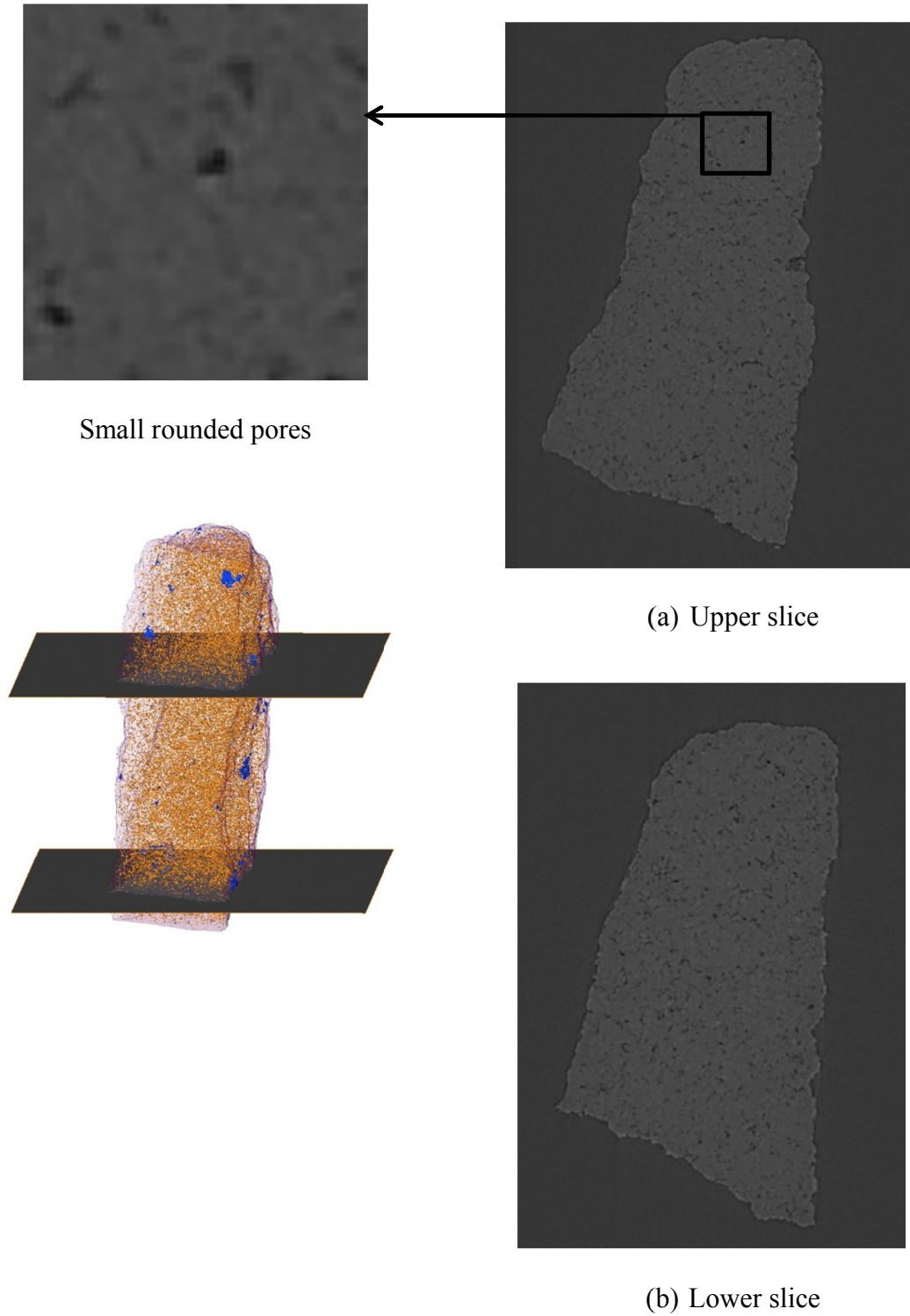
**Figure 4.18: The variation of pore size distribution with the number of wetting/drying cycles from sodium sulfate soundness tests on the same Goldberg aggregate particle using pore width measured from 3D CT images**

### 4.3 Ulland Aggregate – Dolomite

The Ulland aggregate is a dolomitic limestone and has pore characteristics unlike Goldberg limestone. The total porosity of the investigated virgin Ulland aggregate particle is 2.6% and the porosity of the particle when considering pores connected to the surface of the aggregate is 0.1% (Table 4.1). Most of the pore volume in the Ulland virgin aggregate is isolated by material. Figure 4.19 presents a 3D view of the distribution of pores in Ulland virgin aggregate and displays the dominance of the isolated pores. The Ulland dolomite consists of many small pores that are isolated from the surface and from each other. Unlike the Goldberg limestone, most of the pores are spherical in shape, as depicted in Figure 4.20.



**Figure 4.19: CT constructed 3D image of virgin Ulland aggregate, 2.6% total porosity**



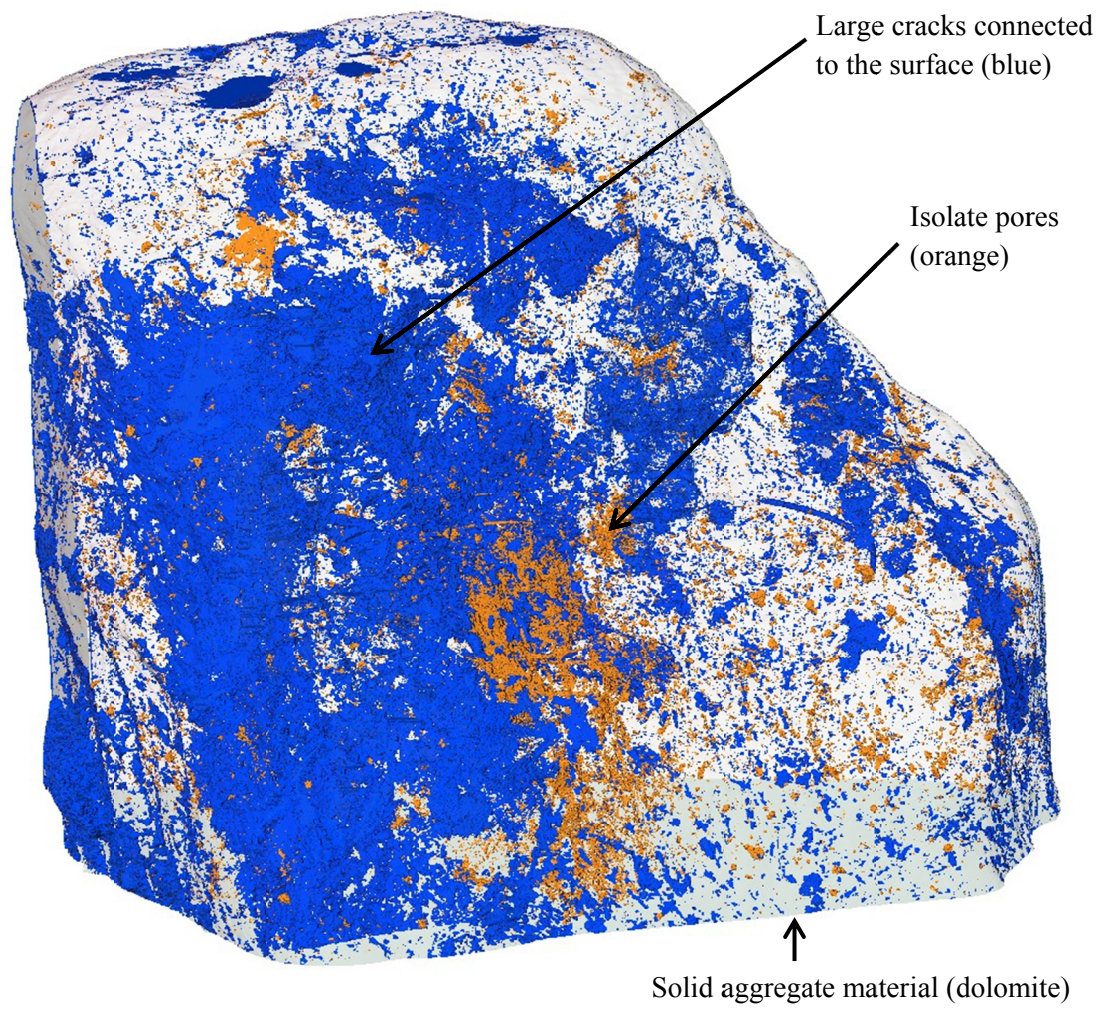
**Figure 4.20: Cross-sections of Ulland virgin aggregate showing small rounded pores**

Figure 4.21 depicts a 3D view of the pore space observed in an Ulland aggregate particle after four cycles of sodium sulfate soundness. Unlike the virgin Ulland aggregate, this treated aggregate exhibited more pores connected to the surface of the aggregate, with a connected porosity of 0.6% and a total porosity of 0.7%. The pores connected to the surface are larger compared with the virgin aggregate and there are cracks within the aggregate, as shown in Figures 4.21 and 4.22. The isolated voids in this Ulland aggregate particle are not as visibly concentrated compared with the virgin aggregate and are larger than the isolated voids within the Ulland virgin aggregate particle.

The aggregate porosity considering pores connected to the surface increases between the virgin Ulland aggregate and the same particle after it was subjected to two more test cycles of sodium sulfate soundness at APS. The increase in porosity is displayed in Figure 4.23.

#### **4.4 New Ulm Aggregate – Quartzite**

The virgin New Ulm quartzite aggregate contains individual grains (crystals) that are cemented/bonded together with another material. Pores occur between the grains where there is no cementation or bonding. Where not cemented, the grain boundary exhibits a complex pore structure, as depicted in Figure 4.24. The total porosity of the virgin New Ulm aggregate is 3.6% and the porosity considering the pores connected to the aggregate surface is 3.0%. The grain boundaries are clearly visualized in the slices shown in Figure 4.25. The higher intensity (brighter) material between the grains is the cementitious material. The slices in Figure 4.25 also show the grains are not completely cemented and pores exist between them.



**Figure 4.21: CT constructed 3D image of Ulland aggregate with four test cycles of sodium sulfate soundness, 0.7% total porosity**

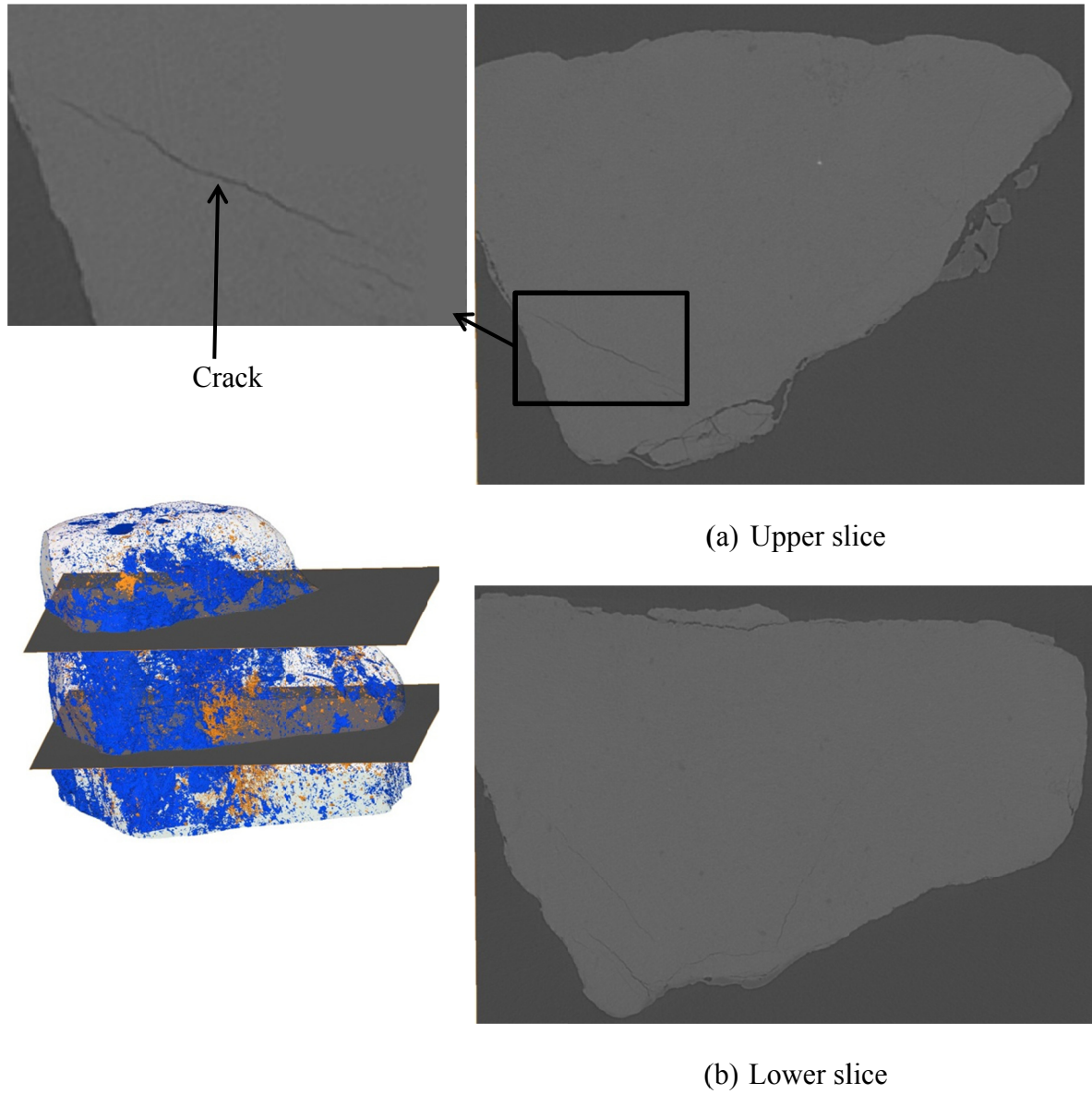


**Figure 4.22: Cross-sections of Ulland aggregate particle subjected to four test cycles of sodium sulfate soundness showing cracks within aggregate solid**

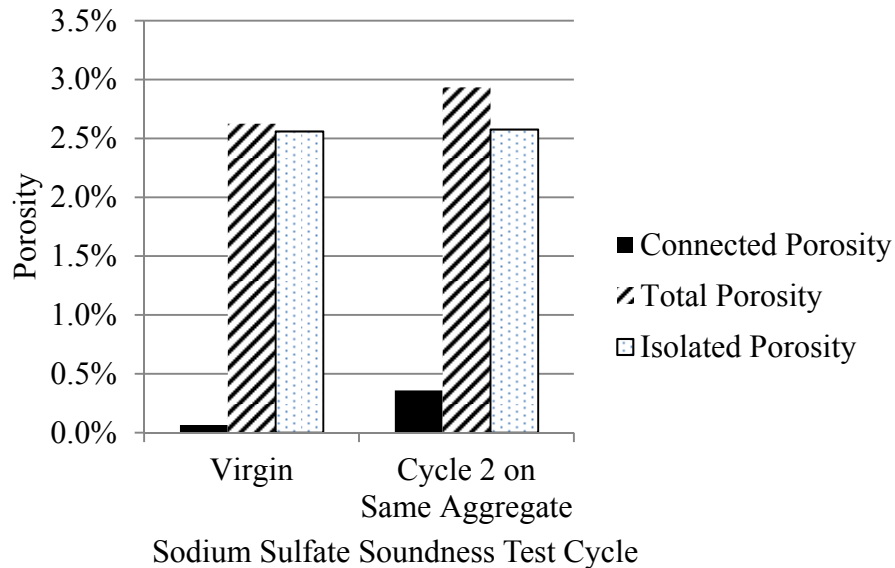


**Figure 4.23: Variation of Ulland aggregate particle porosity with the number of sodium sulfate soundness test cycles on the same aggregate particle**

The New Ulm aggregate subjected to four test cycles of sodium sulfate soundness exhibited an internal structure similar to that of the virgin New Ulm aggregate. However, the aggregate subjected to four test cycles of sodium sulfate soundness did not have the cementation between the grains; instead, only pores exist. The pores are highly connected to each other and to the aggregate surface, as visualized in Figure 4.26. The porosity of this particle in terms of pores connected to the surface is 6.0% and the total porosity is 6.3%. Some isolated voids exist within the aggregate. Figure 4.27 demonstrates the grains are not cemented together as they were in the virgin New Ulm aggregate.

The 3D CT results of the New Ulm quartzite indicate an increase in porosity after cycling with the sodium sulfate soundness test. Figure 4.28 displays the porosities of New Ulm aggregates after treatment with sodium sulfate soundness. After testing, a larger

percentage of the particle pore volume is from the pores connected to the aggregate particle.

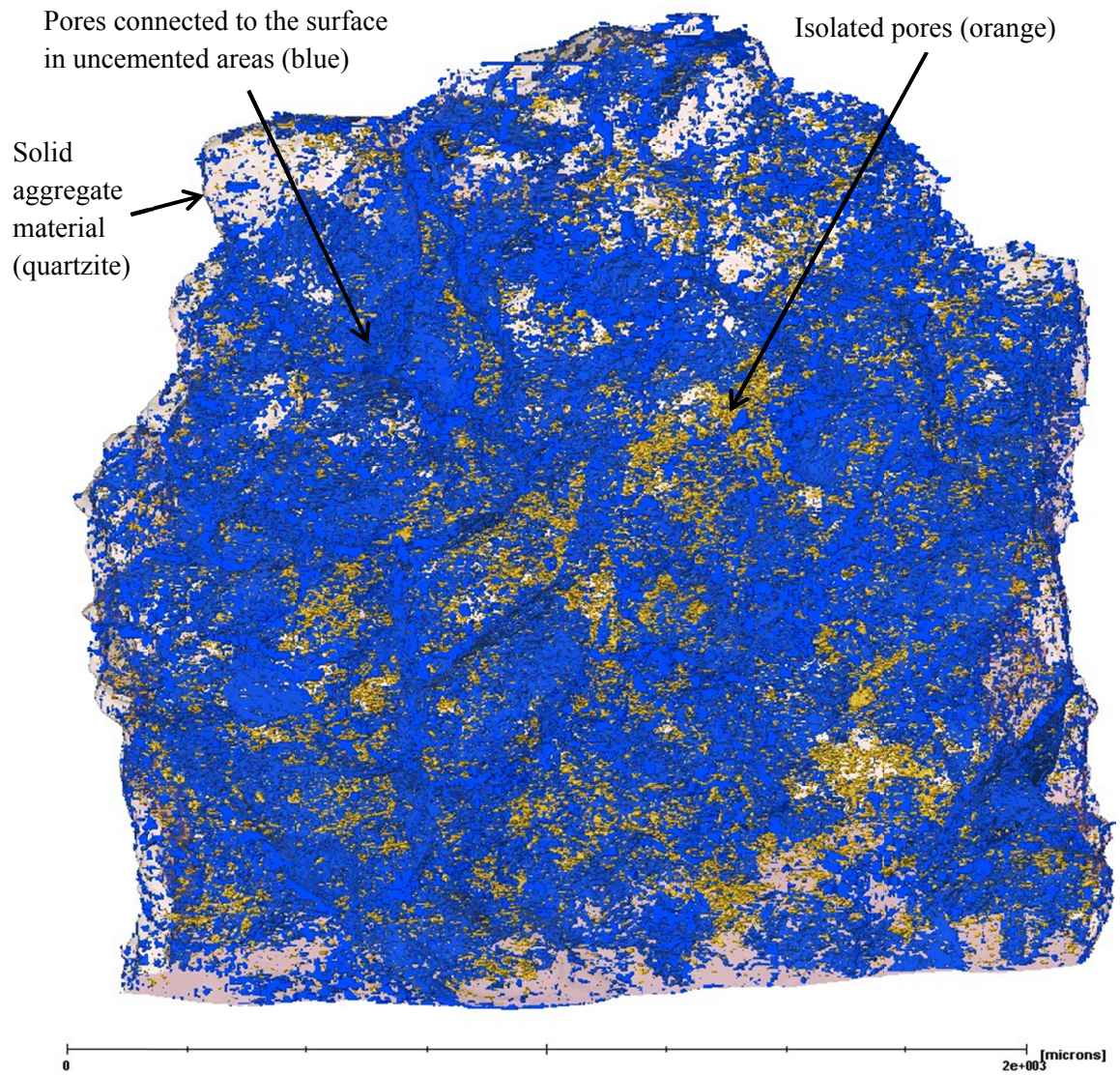


**Figure 4.24: CT constructed 3D image of virgin New Ulm aggregate, 3.6% total porosity**

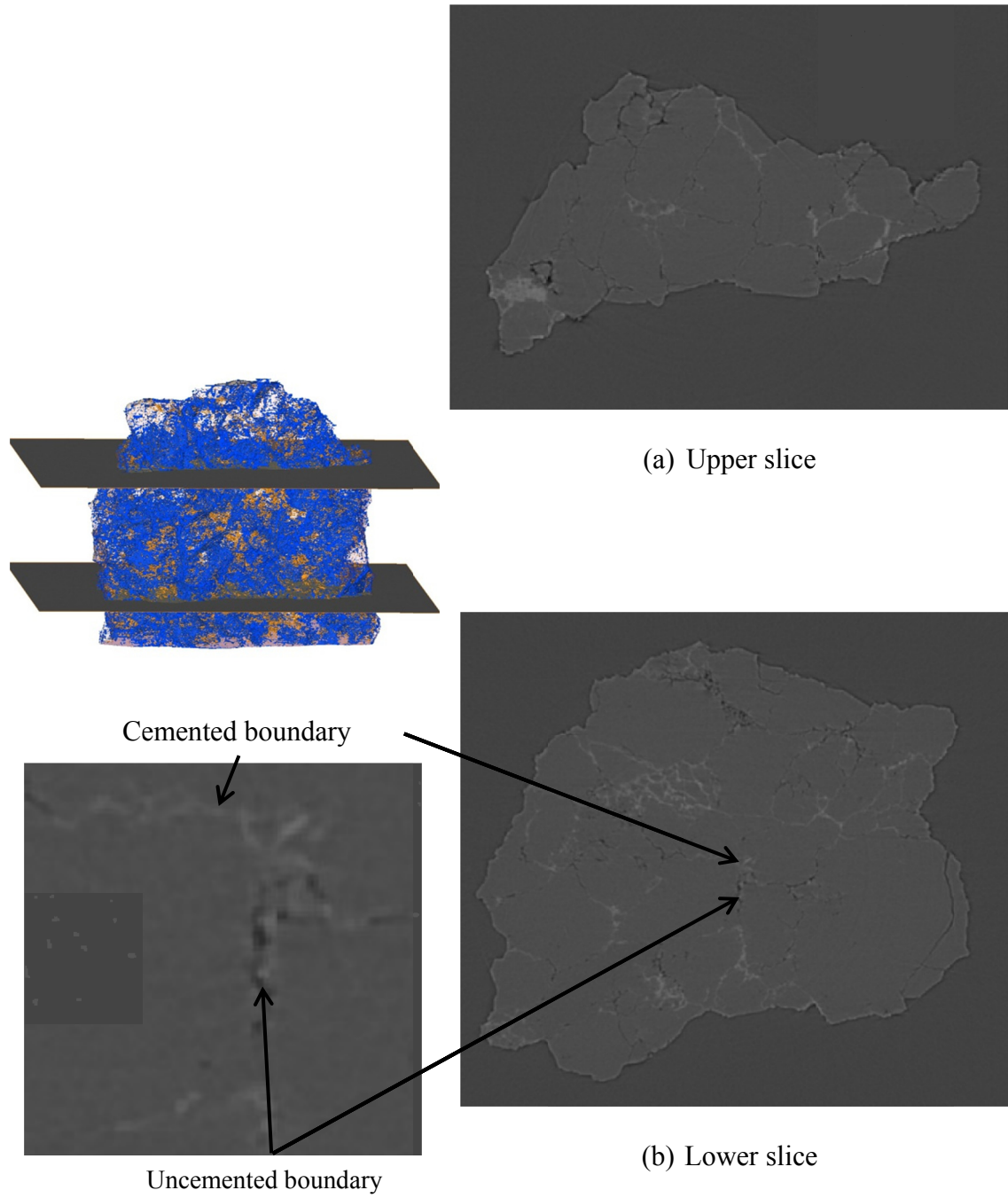


**Figure 4.25: Cross-sections of New Ulm virgin aggregate particle showing cemented and uncemented grain boundaries**

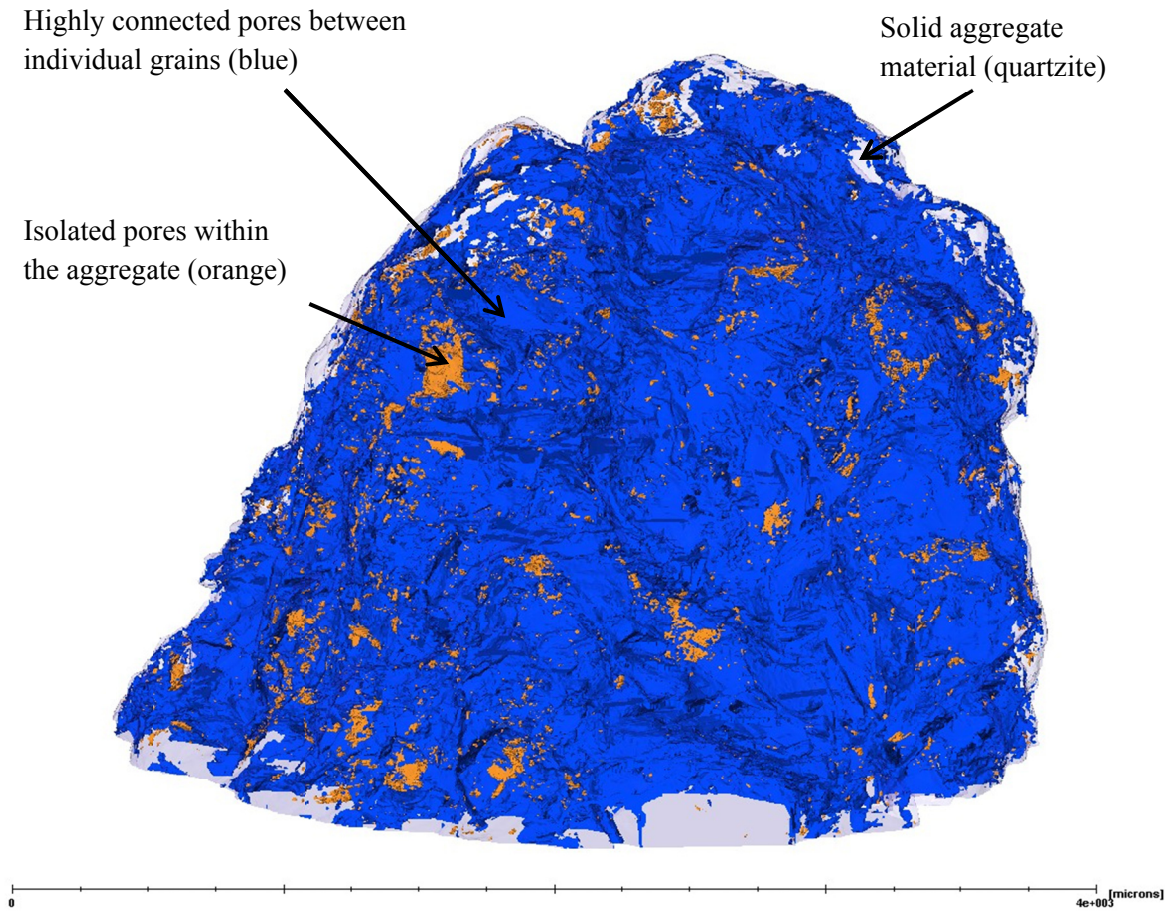


**Figure 4.26: CT constructed 3D image of New Ulm aggregate with four test cycles of sodium sulfate soundness, 6.3% total porosity**

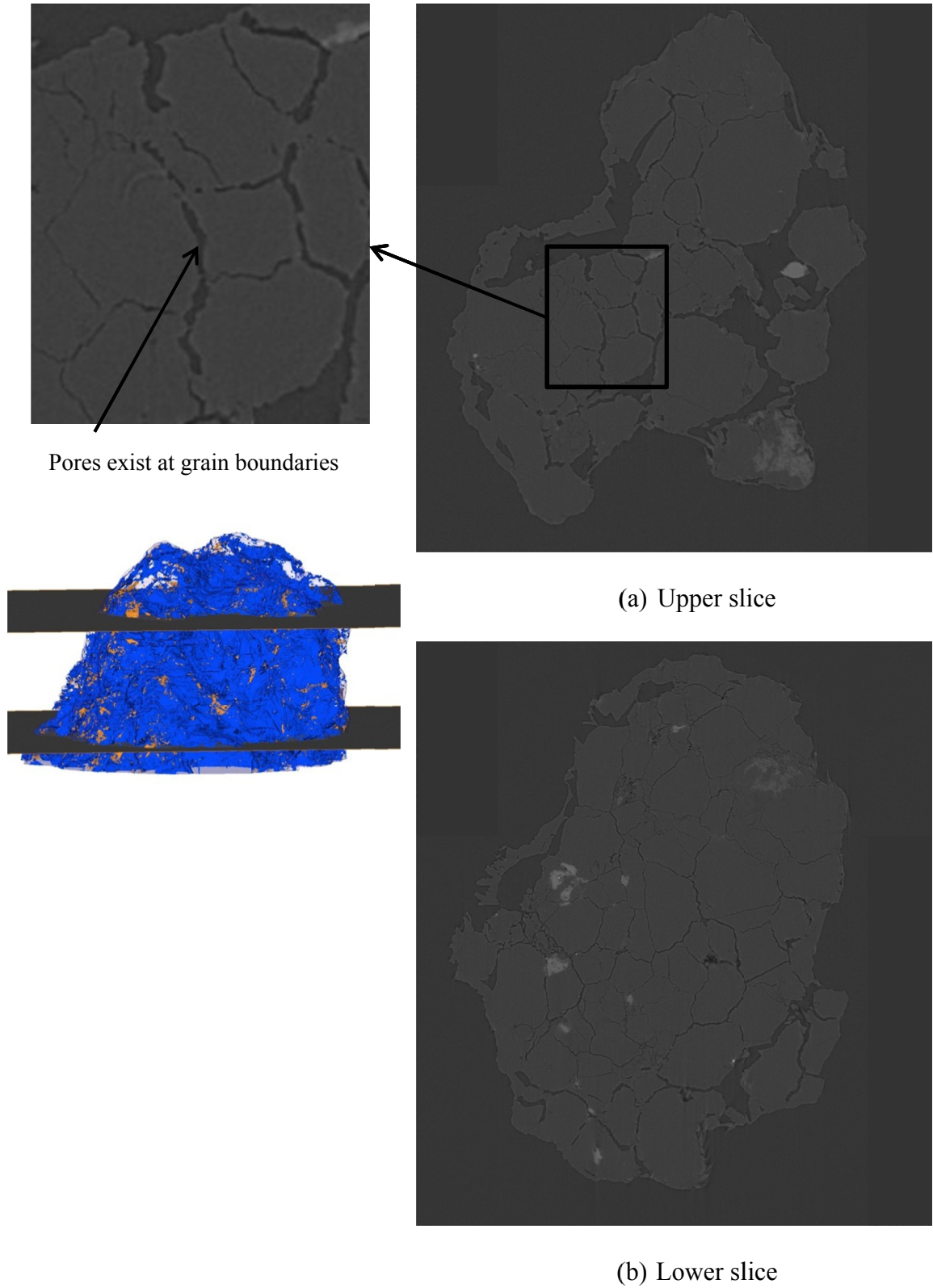
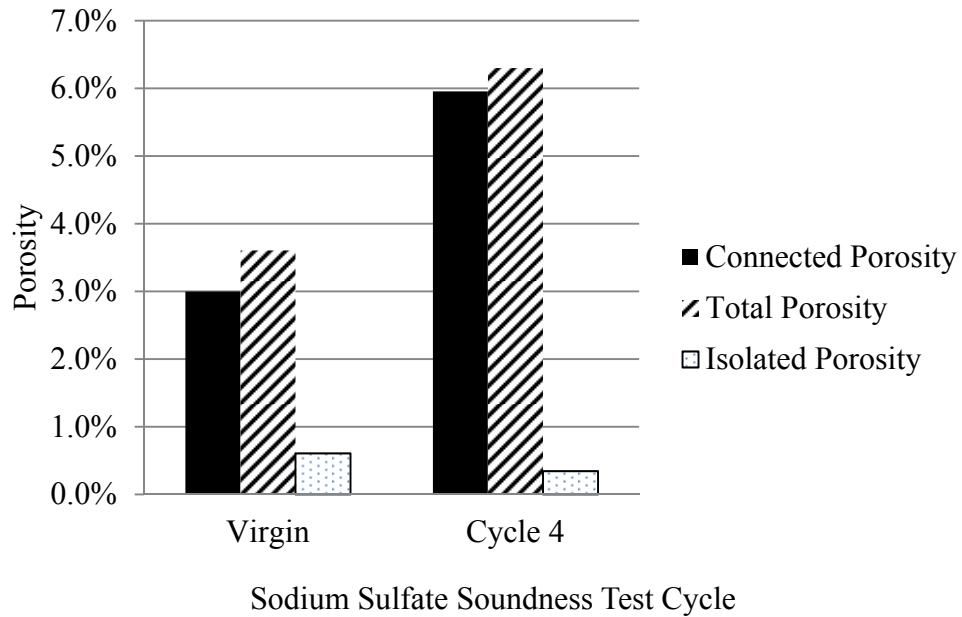
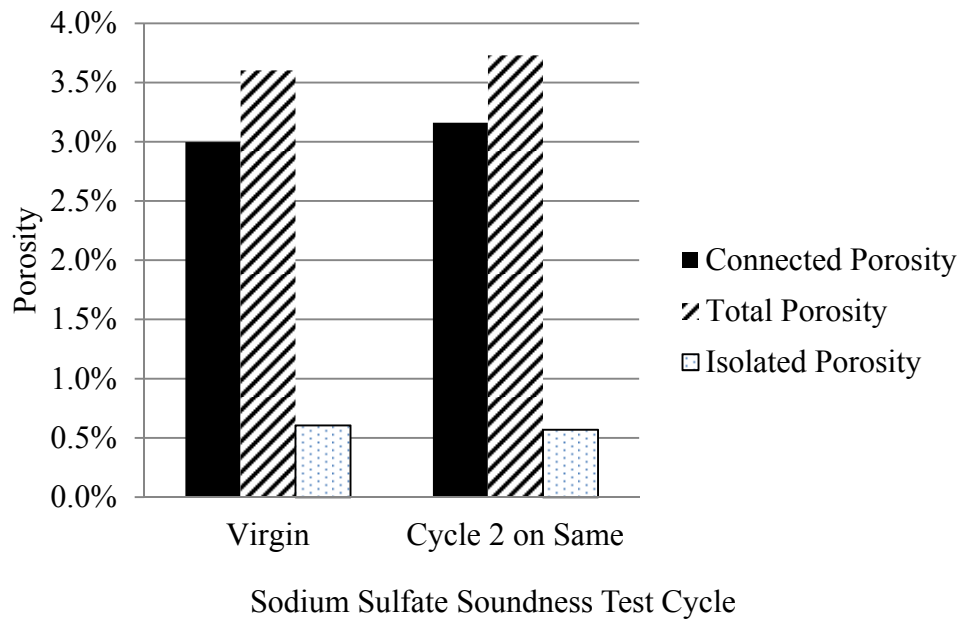


**Figure 4.27: Cross-sections of New Ulm aggregate subjected to four test cycles of sodium sulfate displaying grain boundaries that are not cemented**



(a) On different aggregate particles



(b) On the same aggregate particle

**Figure 4.28: Variation of New Ulm aggregate particle porosity with the number of sodium sulfate soundness test cycles**

#### 4.5 Martin Aggregate – Granite

Analysis of the virgin Martin aggregate sample indicates that it contains few pores. The total porosity of the investigated sample is 1.0% and the porosity when considering the pores connected to the surface of the aggregate is 0.9%, indicating most of the pore volume is connected to the surface of the aggregate. The pores connected to the surface of the aggregate are located near the surface and do not propagate into the aggregate sample, with the exception of one crack shown in Figures 4.29 and 4.30. Isolated pores are small and grouped together near the surface of the aggregate.

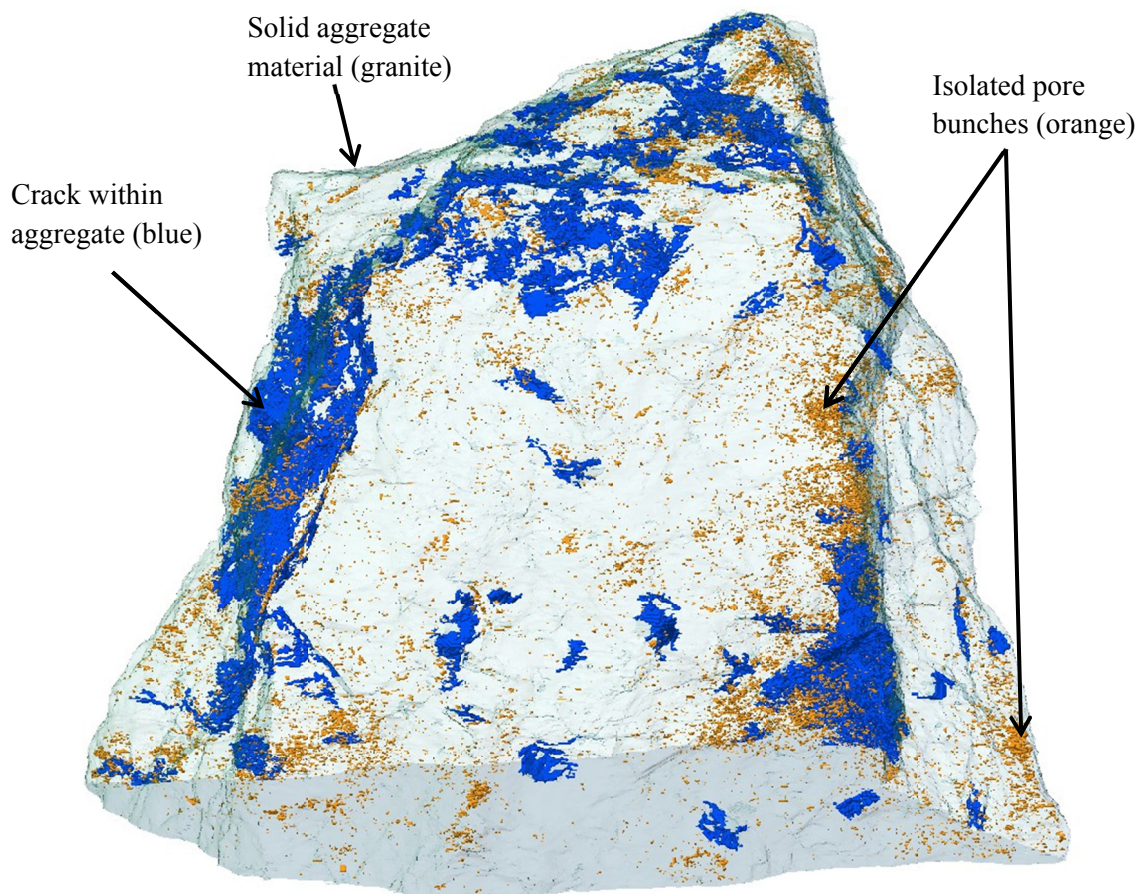


**Figure 4.29: CT constructed 3D image of Martin virgin aggregate, 1.0% total porosity**

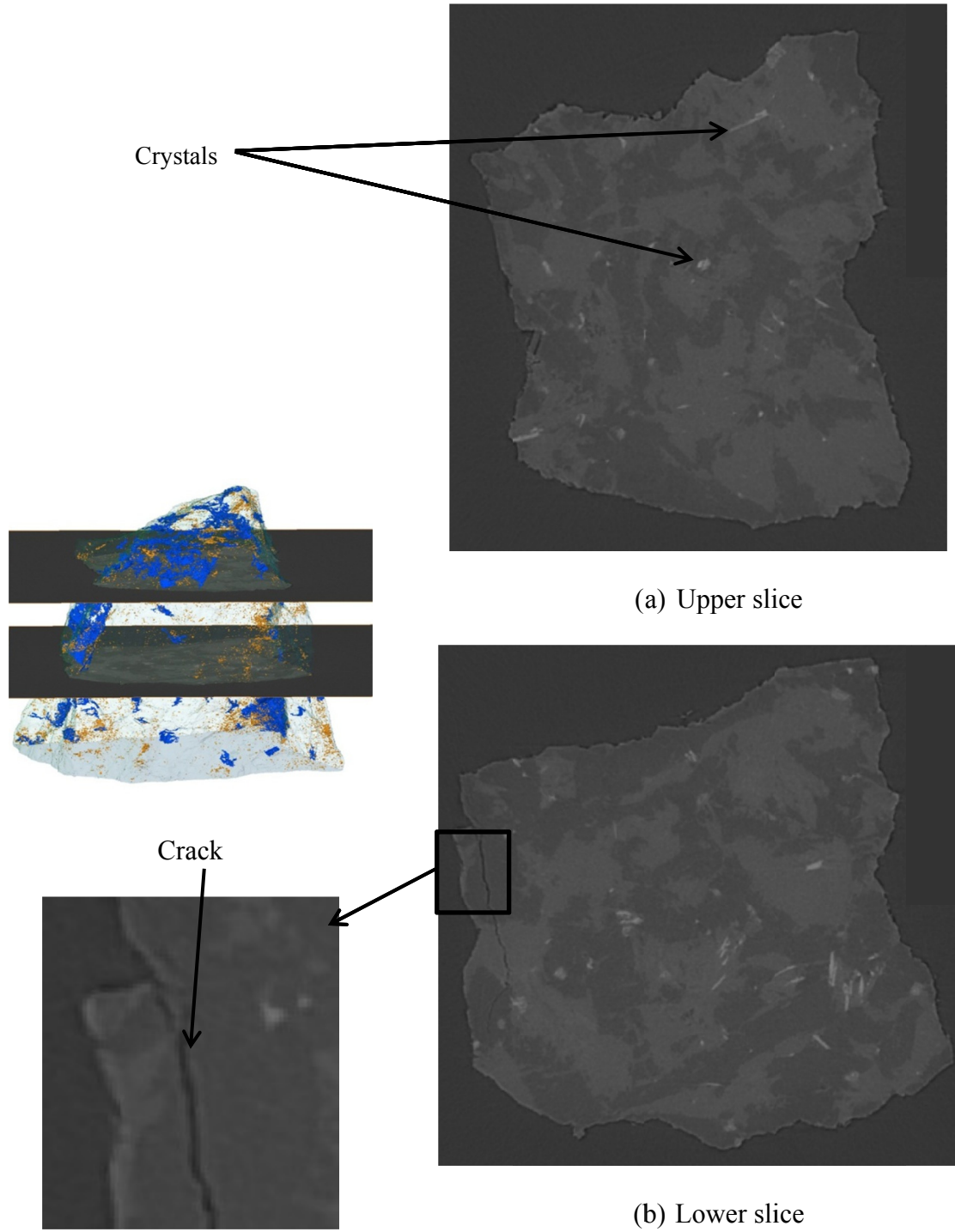


**Figure 4.30: Cross-sections of Martin virgin aggregate particle showing crack**

The Virgin Martin aggregate was subjected to two wetting/drying cycles of the sodium sulfate soundness at APS and scanned again. Figure 4.31 shows the 3D pore structure after the second cycle of sodium sulfate soundness test. The porosity when considering the pores connected to the surface increased to 3.6%, in turn increasing the total porosity to 3.6%. The pores connected to the surface of the aggregate do not propagate into the aggregate to a great extent, but are close to the surface. Figure 4.32 shows a thin layer of solid material that separates the pores from the exterior. The Martin aggregate displayed an increase in porosity, as shown in Figure 4.33.

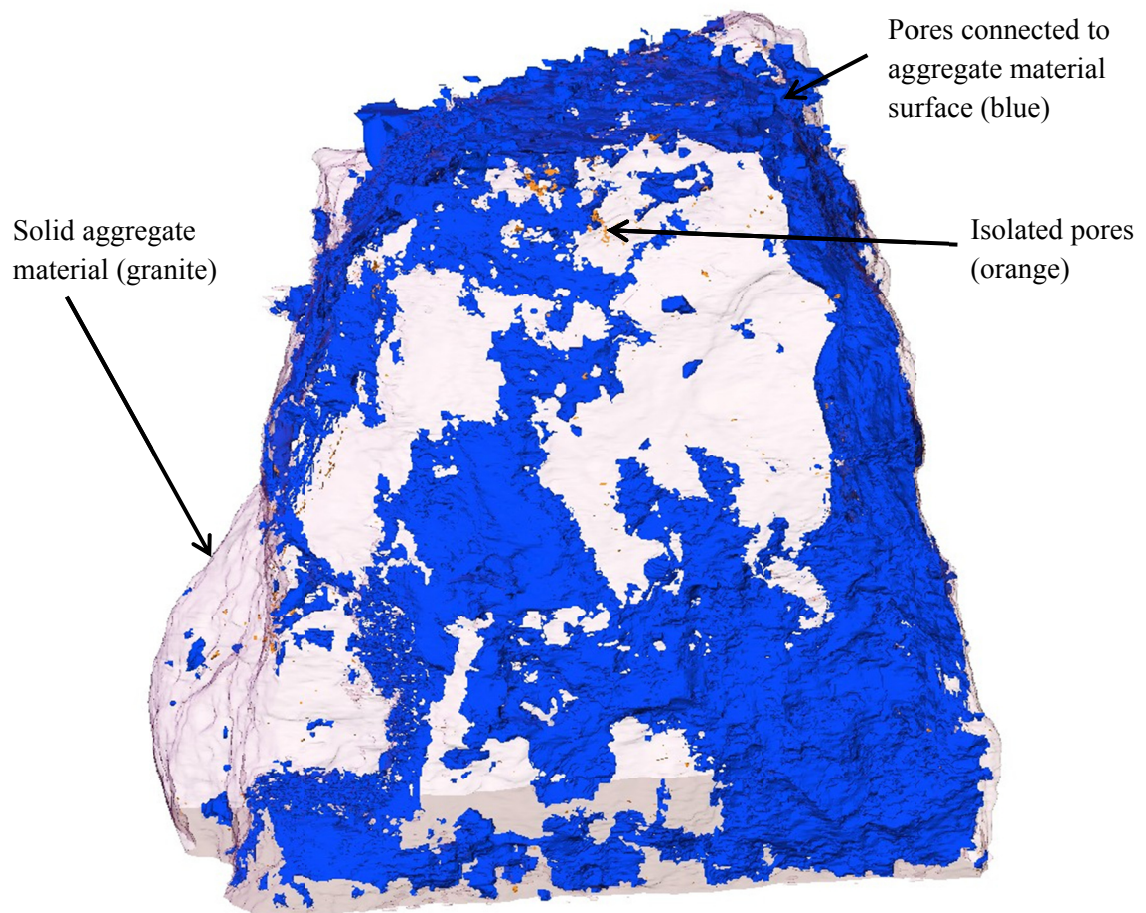


**Figure 4.31: CT constructed 3D image of Martin aggregate with two test cycles of sodium sulfate soundness on the same sample, 3.6% total porosity**

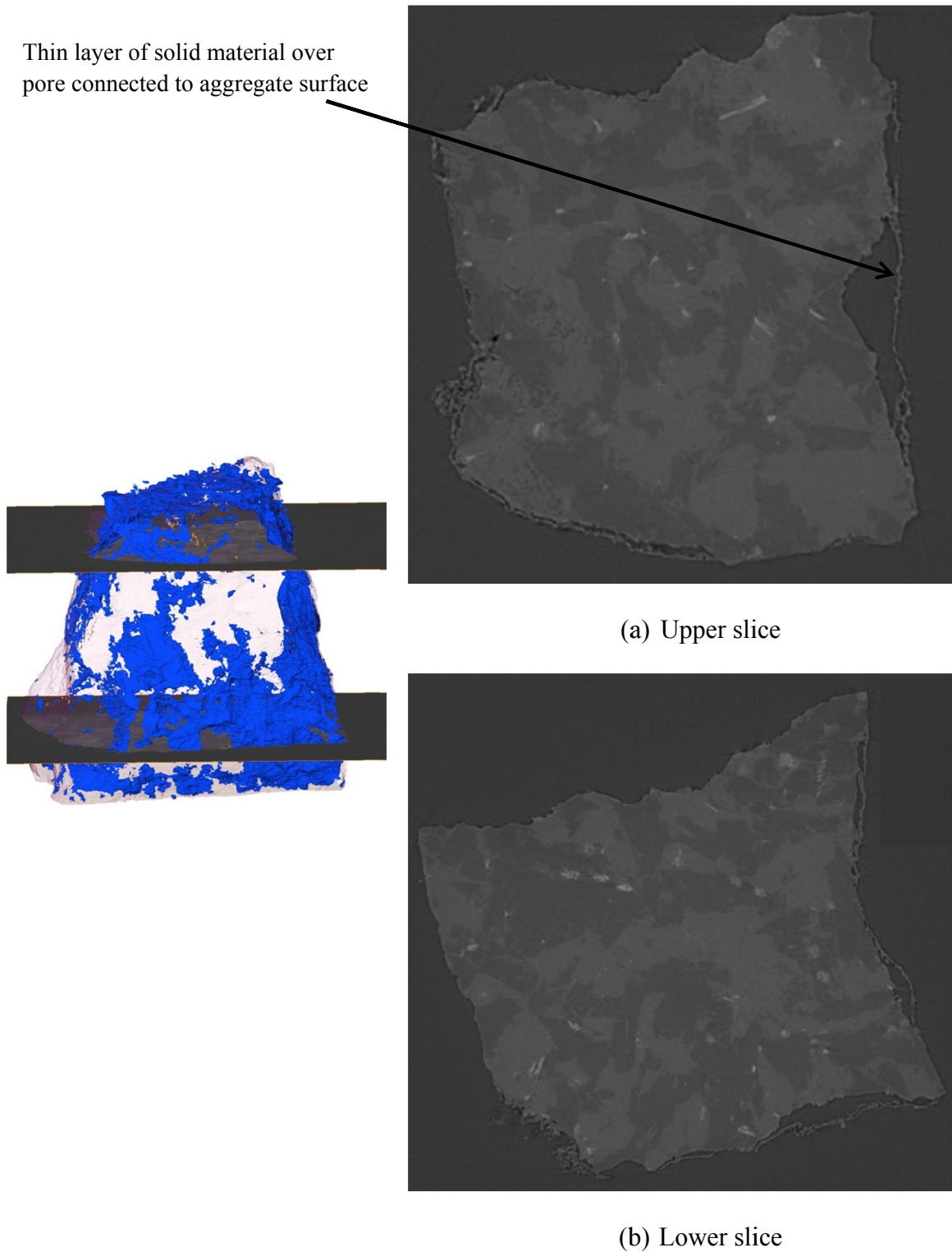


**Figure 4.32: Cross-sections in Martin aggregate with two cycles of sodium sulfate soundness test showing thin layer of solid over pores connected to the surface of the aggregate**

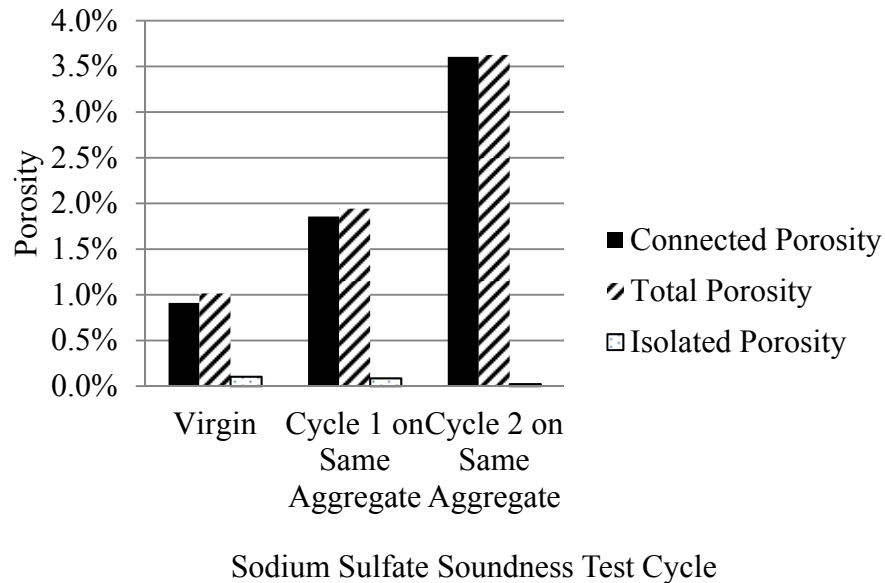
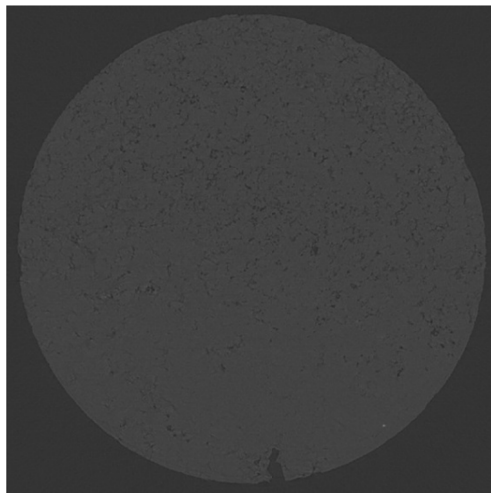


**Figure 4.33: Variation of Martin aggregate particle porosity with the number of sodium sulfate soundness test cycles**

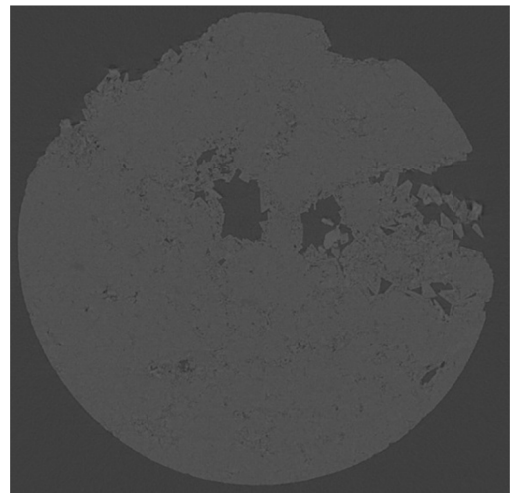
#### 4.6 Aggregates Subjected to Freeze/Thaw Cycles

In addition to sodium sulfate soundness testing, Michigan and Dane County limestone aggregates were subjected to unconfined freezing and thawing cycles according to AASHTO T103 standard test procedure. A light rock and a dark rock from the Michigan source were obtained, and one rock from a quarry in Dane County, WI. Cores were extracted from three aggregate source rocks, as described in Chapter 3. Aggregate samples were subjected to freezing and thawing and sodium sulfate soundness testing, and 3D CT quantification was conducted. Slices from freeze-thaw and sodium sulfate soundness testing are presented in Figures 4.34-4.36. Figure 4.34 shows the pores in the Dane County limestone increased in size and angularity, and Figure 4.37 (a) shows the porosity of the Dane County limestone increased with an increase in the number of test cycles of sodium sulfate soundness and unconfined freezing and thawing. Figure 4.35 and

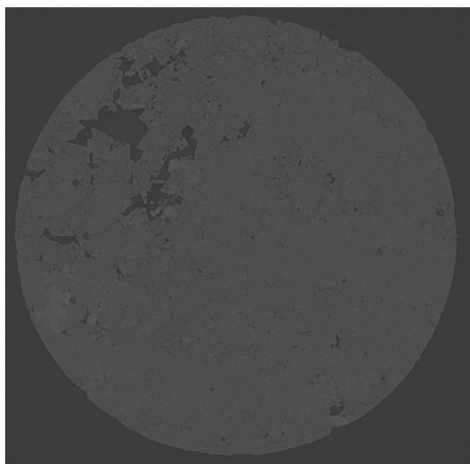
Figure 4.37 (b) show the pores in the light Michigan limestone did not display an increase in volume or significant change in structure after test cycles of sodium sulfate soundness, or unconfined freezing and thawing. Figures 4.36 and 4.37 (c), respectively, show the dark Michigan limestone increased in pore size and volume.



(a) Virgin

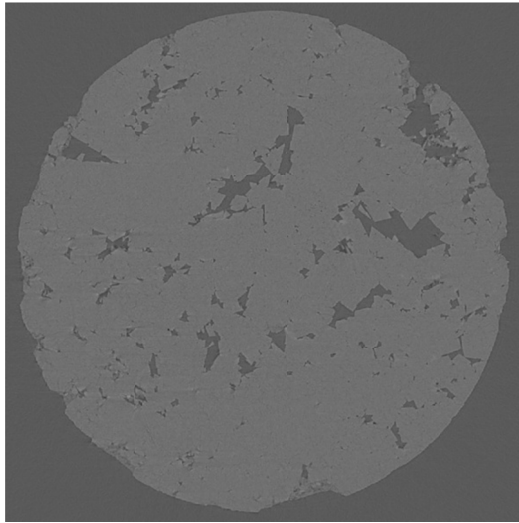


(b) 45 freeze/thaw cycles

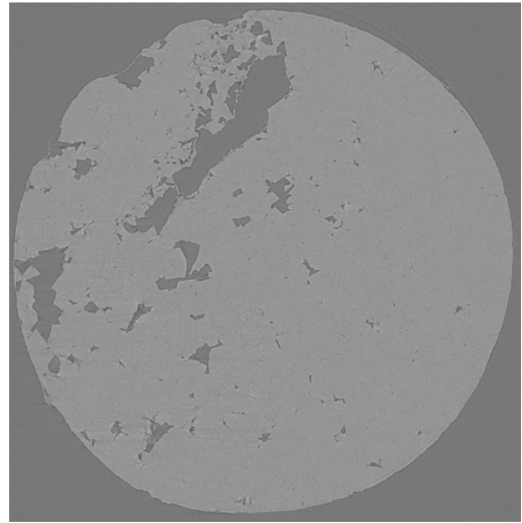


(c) Five test cycles of sodium sulfate soundness

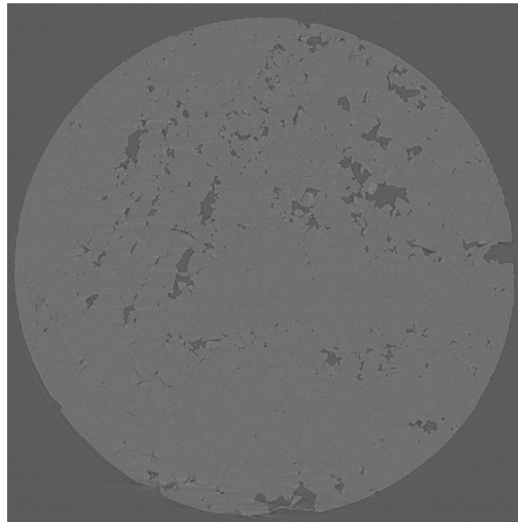
**Figure 4.34: Cross-sections of Dane County limestone with 45 freeze/thaw cycles and five test cycles of sodium sulfate soundness**



(a) Virgin

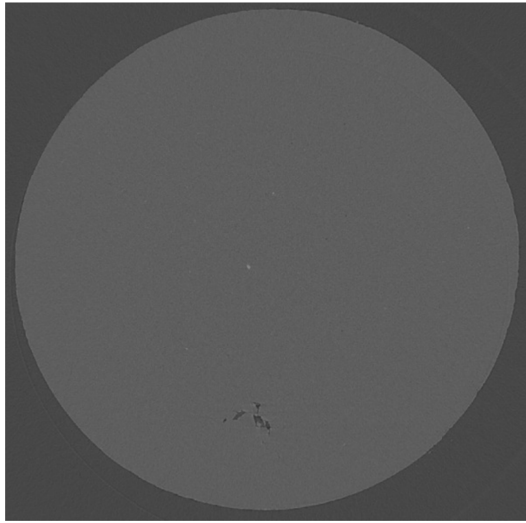


(b) 45 freeze/thaw cycles

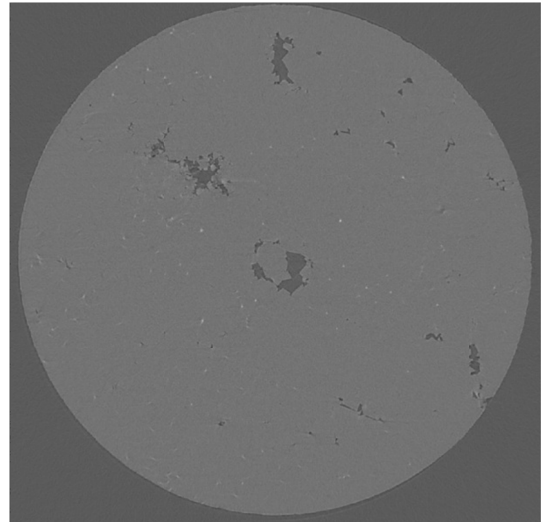


(c) Five test cycles of sodium sulfate soundness

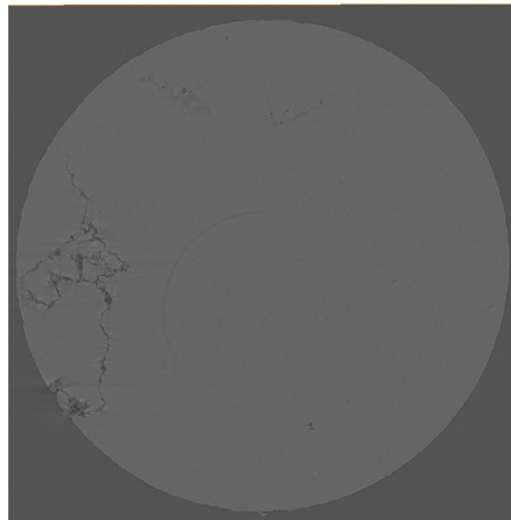
**Figure 4.35: Cross-sections of Michigan (light) limestone with 45 freeze/thaw cycles and five test cycles of sodium sulfate soundness**



(a) Virgin



(b) 45 freeze/thaw cycles



(c) Five test cycles of sodium sulfate soundness

**Figure 4.36: Cross-sections of Michigan (dark) limestone with 45 freeze/thaw cycles and five test cycles of sodium sulfate soundness**

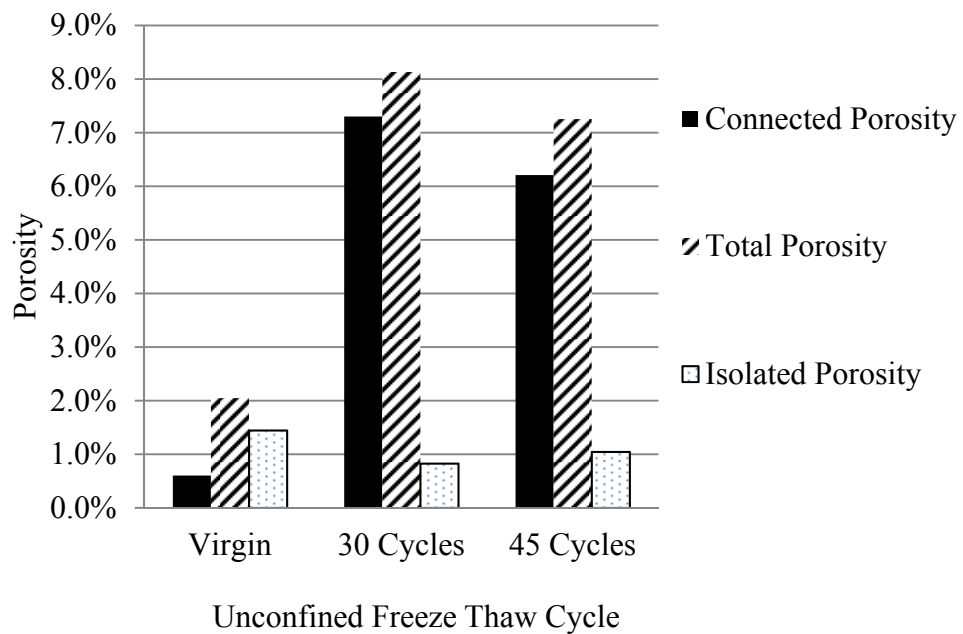
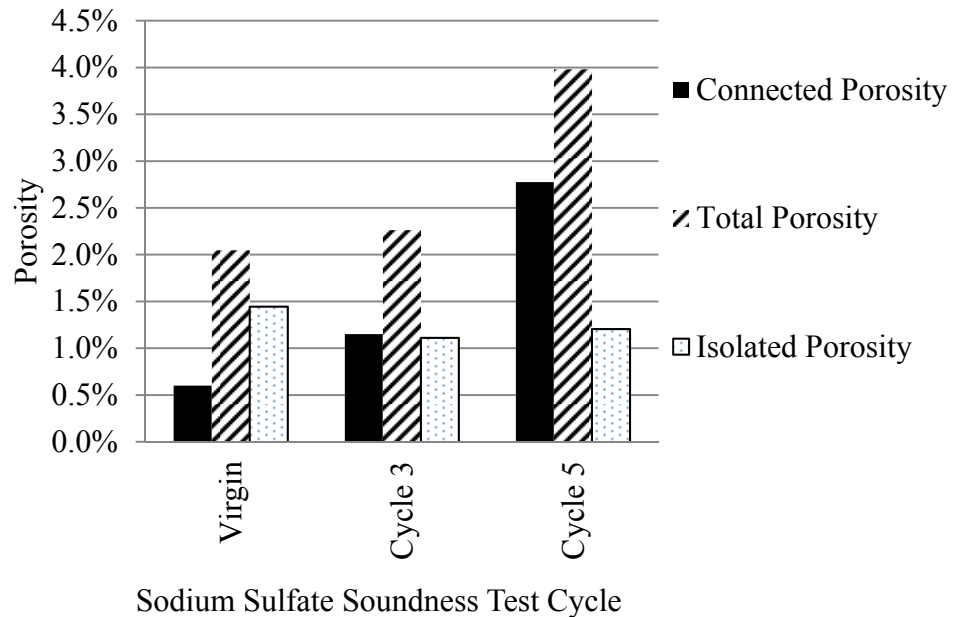


**Figure 4.37 (a): Variation of Dane County limestone aggregate particle porosity with the number of sodium sulfate soundness and unconfined freeze thaw test cycles**

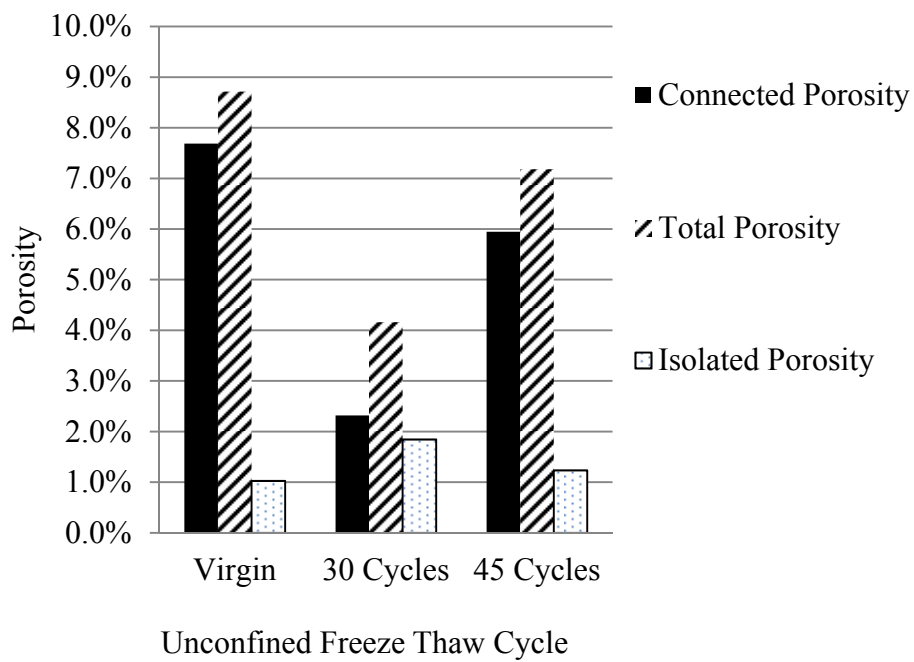
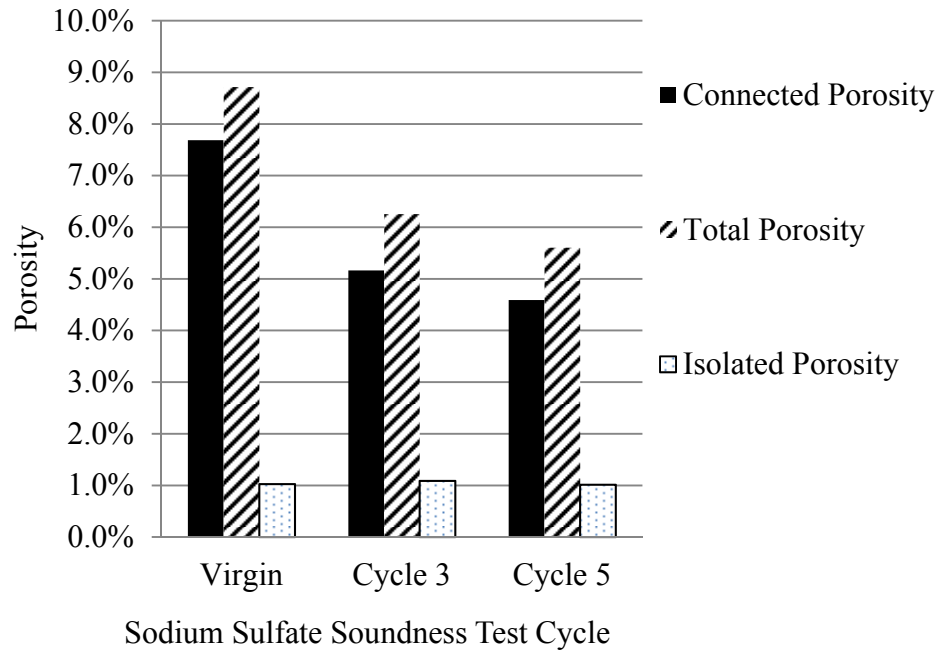


**Figure 4.37 (b): Variation of light Michigan limestone aggregate particle porosity with the number of sodium sulfate soundness and unconfined freeze thaw test cycles**

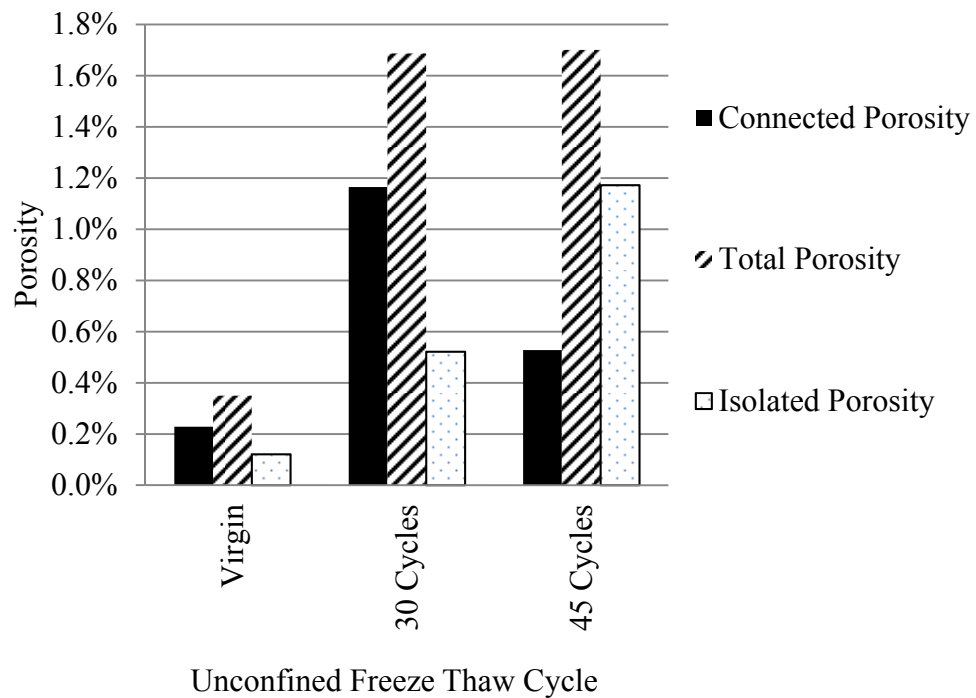
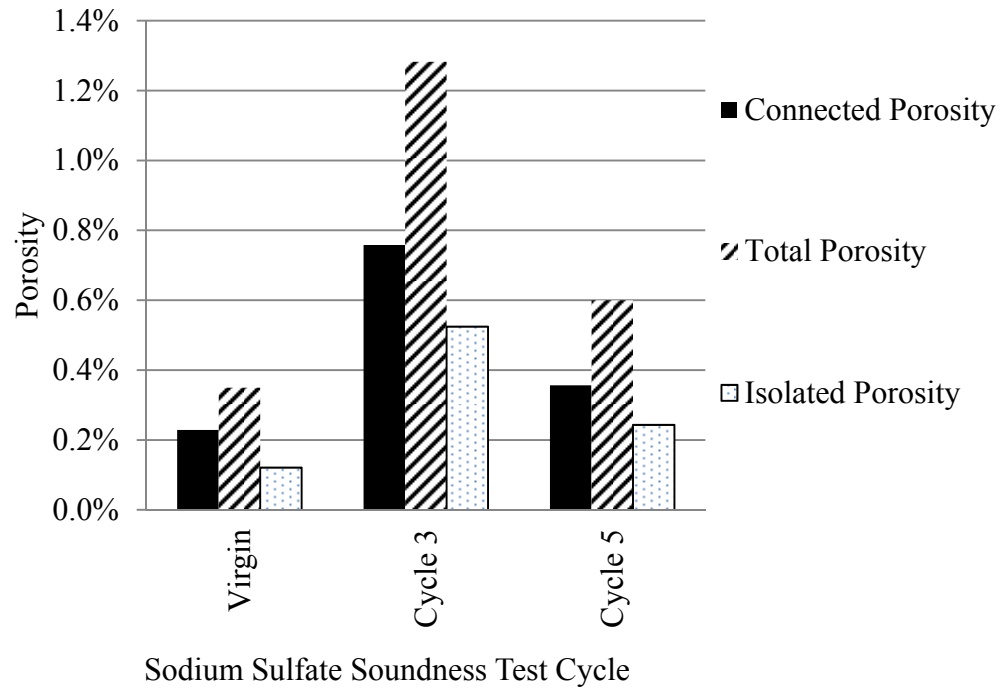
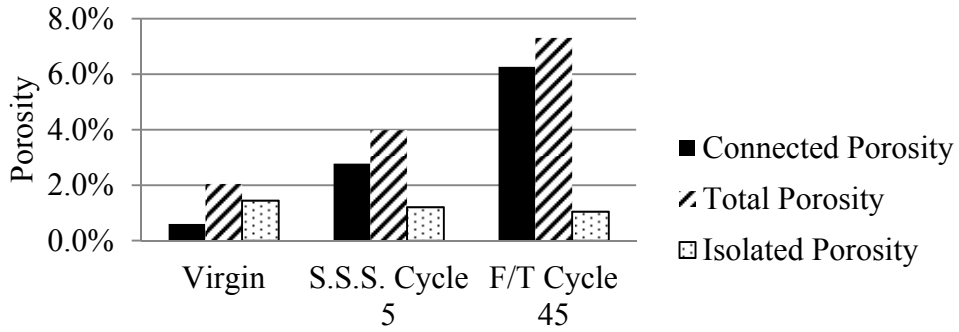


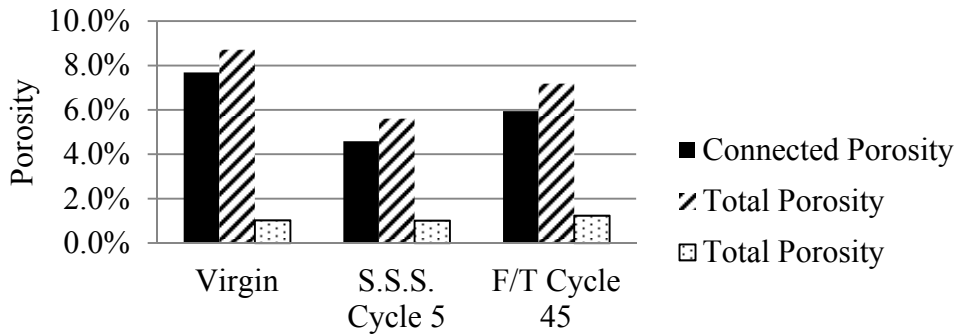
**Figure 4.37 (c): Variation of dark Michigan limestone aggregate particle porosity with the number of sodium sulfate soundness and unconfined freeze thaw test cycles**

The porosities of the aggregates subjected to freeze-thaw and sodium sulfate soundness were compared at extreme cycles (five test cycles of sodium sulfate soundness and 45 test cycles of freezing and thawing), as shown in Figure 4.38. All three aggregates subjected to both types of testing have higher porosities at 45 cycles of freezing and thawing than five test cycles of sodium sulfate soundness. This coincides with higher degradation and deterioration of aggregates at 45 cycles of freezing and thawing than five test cycles of sodium sulfate soundness. Even though the aggregate cores were obtained from the same area of each rock, the virgin light Michigan core has a higher porosity than the core subjected to five test cycles of sodium sulfate soundness, as well as the core subjected to 45 cycles of freezing and thawing, as shown in Figure 4.38 (b). The light Michigan limestone did show a higher porosity in the core subjected to 45 freeze-thaw cycles than the core subjected to five test cycles of sodium sulfate soundness. The Dane County limestone and dark Michigan limestone demonstrated an increase in porosity over the virgin aggregate, as demonstrated in Figure 3.38 (a) and (c).



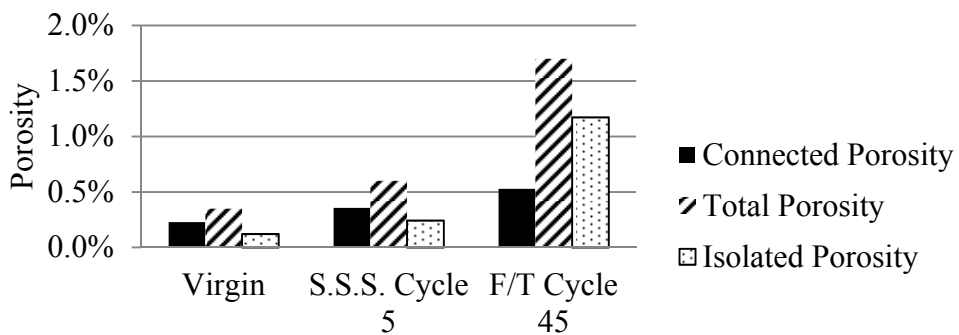
Test cycle of Sodium Sulfate Soundness or Freeze/Thaw

(a) Dane County Limestone



Test cycle of Sodium Sulfate Soundness or Freeze/Thaw

(b) Light Michigan Limestone



Test Cycle of Sodium Sulfate Soundness or Freeze/Thaw

(c) Dark Michigan Limestone

**Figure 4.38: Comparison of sodium sulfate soundness with unconfined freezing and thawing**

#### 4.7 Kraemer and Larson Aggregates - Limestone

Inspection of the 3D CT constructed images of a virgin Kraemer limestone indicated some connected pores and isolated pores evenly distributed throughout the aggregate as shown in Figure 4.39. Five test cycles of sodium sulfate soundness on a Kraemer aggregate induced a highly connected pore structure throughout the aggregate with scattered isolated pores as shown in Figure 4.40. Larson limestone displayed characteristics similar to Kraemer. Porosity analysis based on CT images for these aggregates is summarized in Table 4.1

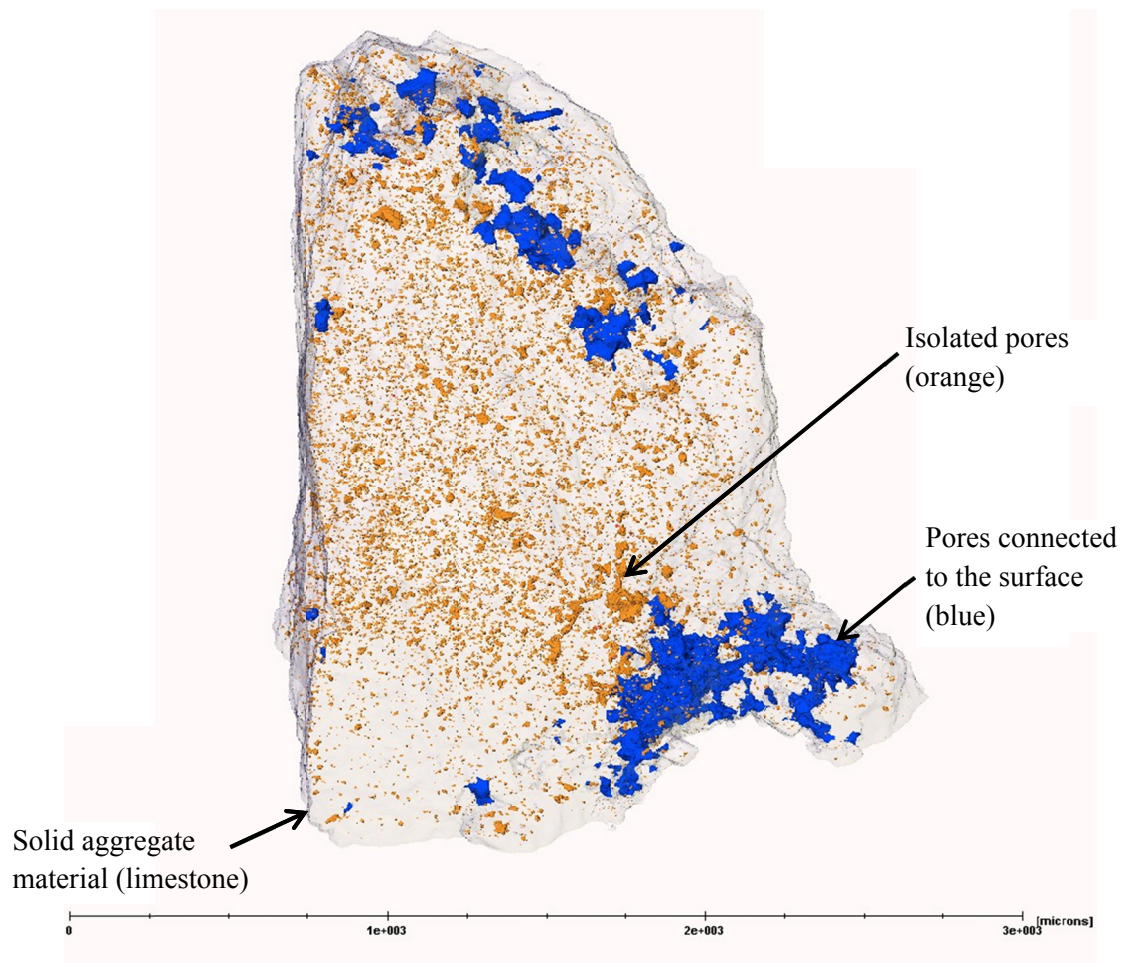


**Figure 4.39: CT constructed 3D image of Kraemer virgin aggregate, 3.6% total porosity**

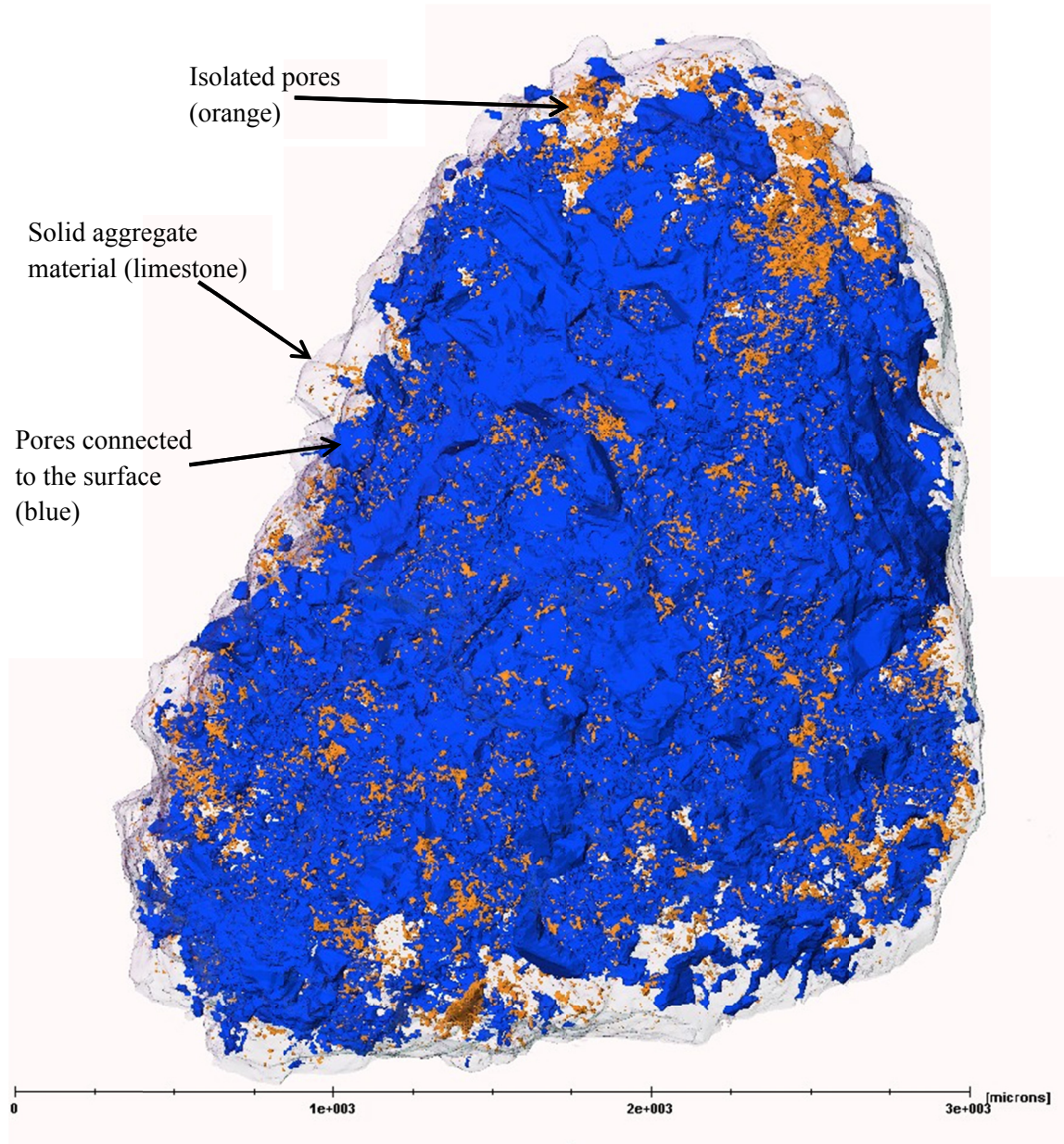
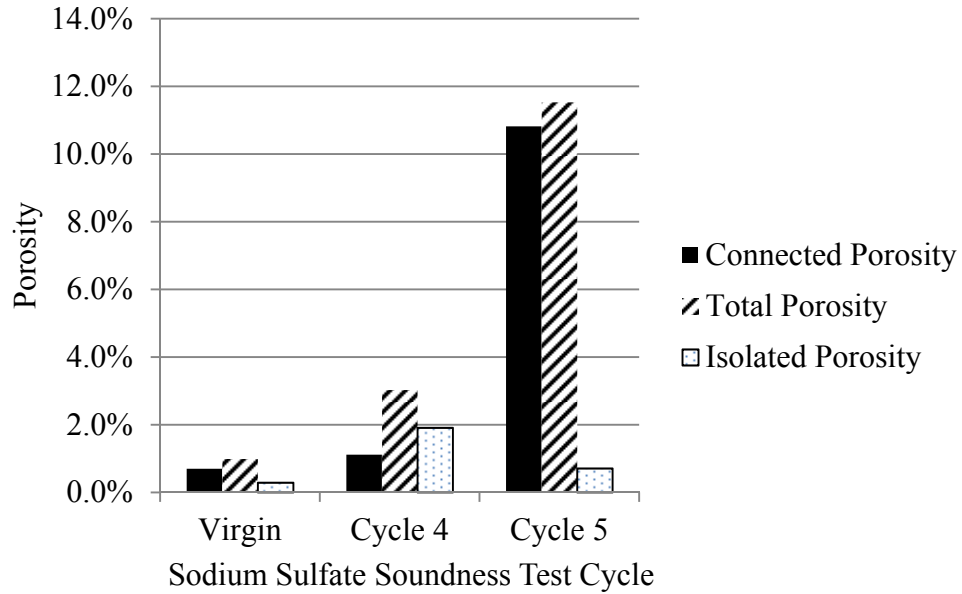
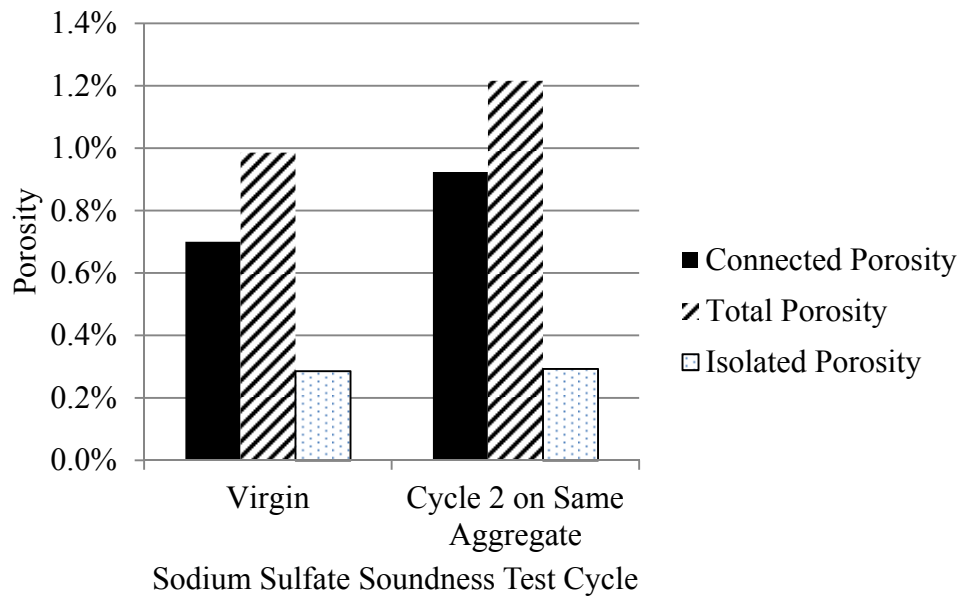


**Figure 4.40: CT constructed 3D image of Kraemer aggregate with five cycles of sodium sulfate soundness, 11.5% total porosity**

Figures 4.41 and 4.42 display the porosity of test cycles of sodium sulfate soundness on Kraemer and Larson aggregate samples, respectively.

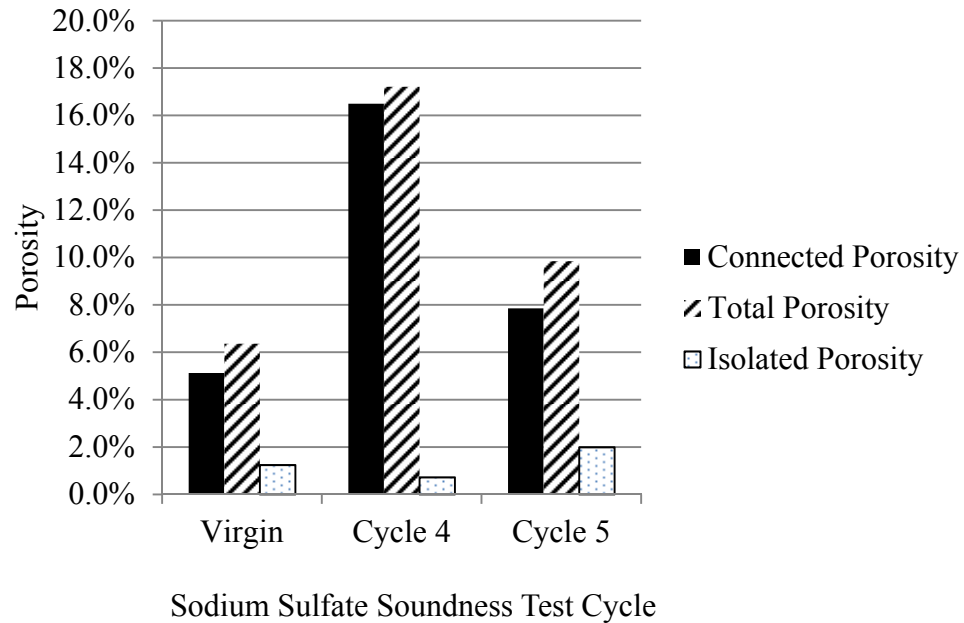


(a) On different aggregate particles

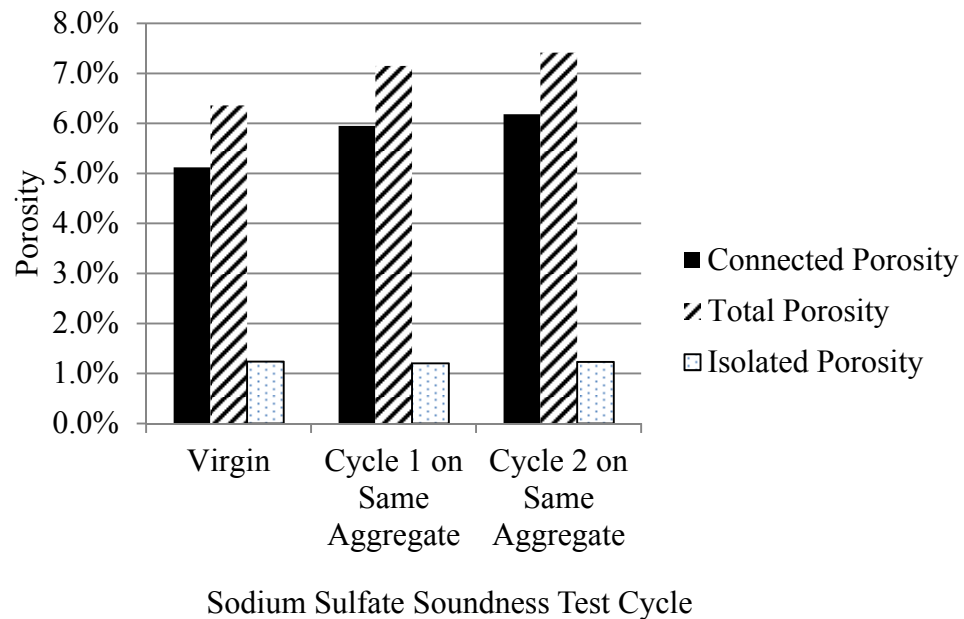


(b) On the same aggregate particle

**Figure 4.41: Variation of Kraemer aggregate particle porosity with the number of sodium sulfate soundness and unconfined freeze thaw test cycles**



(a) On different aggregate particles



(b) On the same aggregate particle

**Figure 4.42: Variation of Larson aggregate particle porosity with the number of sodium sulfate soundness and unconfined freeze thaw test cycles**

## Chapter 5

### Conclusions and Recommendations

The objective of this research study is to use X-ray CT technology to investigate the internal structure and porosity of various types of aggregate particles such as limestone, granite, and quartzite. Characterizing the internal structure of aggregate particles, and quantifying porosity, pore space distribution, and connectivity within the particles is essential to understanding and predicting the material behavior when it is subjected to various loading conditions. Aggregate particles are important components of Portland cement concrete and other materials that are used to build infrastructure. These materials, with aggregate particles as the main components, are subjected to various internal and external loading. One of the internal loading mechanisms that is detrimental to the aggregate structure comes from harsh environmental conditions due to low temperatures. Water freezing and thawing within the aggregate internal structure deteriorates and degrades aggregate particles, thereby affecting the structural integrity and performance of infrastructure. Characterization of the internal structure of aggregate particles and pore space will help further understanding of aggregate durability and its connection with pore space, pore space distribution, and pore space connectivity.

Virgin and treated aggregate particles of different origins were subjected to X-ray CT scanning to obtain high-resolution 3D images. Aggregate treatments consisted of wetting/drying cycles conducted using the sodium sulfate soundness test, and actual freeze-thaw cycles via the freeze-thaw test to simulate the impact of the environment on aggregate durability. The CT scans were carried out using a sector 13-BMD synchrotron

microtomography beamline at the Advanced Photon Source of the Argonne National Laboratory, Illinois. The acquired CT scan images were subjected to post-processing analysis to construct 3D rendering of the aggregate particles, which display the aggregate solid material and pore space. Furthermore, the acquired 3D high-resolution images were analyzed to investigate the pore structure and micro-cracks of these aggregate types. Aggregate durability and strength is greatly influenced by size, distribution, and connectivity of pore spaces within aggregate particles. Quantitative analysis was conducted on these images to identify parameters pertaining to aggregate durability.

Based on the results of this study, the following conclusions have been reached:

1. The X-ray CT technology was useful for visualizing the internal structure of aggregate particles with high resolution. This visual inspection provided information on pore space characteristics such as pore shape, connectivity, and distribution. In addition, volumetric quantities, such as the volume of aggregate particles and the volume of pore space, were identified and measured. These measured quantities were used to calculate porosities of the investigated aggregates, which provided properties of these aggregates using the constructed 3D CT images (non-conventional method). As an example, the calculated total porosity of the investigated virgin aggregates ranges between 0.4% for the dark Michigan limestone and 8.7% for the light Michigan limestone.
2. The sodium sulfate soundness test effects on the treated aggregates (degradation, disintegration and weathering) were significant, as observed in the 3D CT images of treated aggregate particles. Pore space volume increased as the aggregate

particles were treated with wetting/drying cycles of sodium sulfate solution. The total porosity for one of the virgin Michigan limestone particles is 4.2%, which increased to 5.2% after one wetting/drying sodium sulfate soundness cycle, and to 8.21% after two wetting/drying sodium sulfate soundness cycles on the same particle.

3. The sodium sulfate soundness test significantly affected the permeable (connected) pore space and induced degradation/disintegration, which increased the volume of connected pore space with the increase of the number of wetting/drying test cycles. The connected porosity for one of the virgin Michigan limestone particles is 3.0%. This connected porosity increased to 3.5% after one wetting/drying sodium sulfate soundness cycle, and to 7.1% after two wetting/drying sodium sulfate soundness cycles on the same particle.
4. Isolated pore space remained unchanged with the number of sodium sulfate test cycles, since the salt could not penetrate these pores to induce internal force of expansion, which degraded and disintegrated the aggregate structure.
5. The freeze-thaw test induced changes to pore space of the treated aggregates with the noticeable impact on connected pore space of the aggregate particle.

Based on the results of this study, the following is recommended for future work:

1. Physical tests such as mercury intrusion porosimetry should be conducted and compared with CT porosity.
2. Finite element analysis and physical compression tests could be conducted on aggregate scans with increasing test cycles to determine the effect of testing the strength of the particles.

3. More samples should be scanned to increase the confidence of the testing effect.
4. More tests on the same aggregate should be conducted.

## References

- Avizo (R) 6 User's Guide. (2010). *User's Guide*. Konrad-Zuse-Zentrum fur Informationstechnik Berlin and Visualization Sciences Group.
- Advanced Photon Source. (2011). *Insertion Devices & Brilliance*. Retrieved November 8, 2011, from Argonne National Laboratory: <http://www.aps.anl.gov/>
- Aguilar, A. (n.d.). *Undulator Beamline 10.0.1*. Retrieved October 20, 2011, from <http://ssg.als.lbl.gov/ssgdirectory/aguilar/BL10homepage.html>
- Alaknanda, R., & Kumar, P. (2009). Flaw detection in radiographic weldment images using morphological watershed segmentation technique. *NDT&E International*, 2-8.
- Albee, P. B., Stockman, G. C., & Smucker, A. J. (2000). Extraction of pores from microtomographic reconstructions of intact soil aggregates. *Computer Vision and Pattern Recognition 2000*. Hilton Head, SC.
- Alshibli, K. A., & Hasan, A. (2010). 3D Characterization of Particle Interaction Using Synchrotron Microtomography. In K. A. Alshibli, & A. H. Reed (Ed.), *Advances in Computed Tomography for Geomaterials GeoX 2010* (pp. 26-33). New Orleans: ISTE Ltd and John Wiley & Sons, Inc.
- Baruchel, J., Cloetens, P., Hartwig, J., & Schlenker, M. (2002). Imaging with Third-Generation Synchrotron X-rays. In *Third-Generation Hard X-ray Synchrotron Radiation Sources* (pp. 181-202). New York: John Wiley & Sons, Inc.
- Birgul, R. (2008). Monitoring macro voids in mortar by X-ray computed tomography. *Nuclear Instruments and Methods in Physics Research*, A596, 459-466.
- Borland, M., Decker, G., Emery, L., Guo, W., Harkay, K., Sajaev, V., & Yao, C.-Y. (2010, September 8). *APS Storage Ring Parameters*. Retrieved November 5, 2011, from [http://www.aps.anl.gov/Accelerator\\_Systems\\_Division/Accelerator\\_Operations\\_Physics/SRparameters/](http://www.aps.anl.gov/Accelerator_Systems_Division/Accelerator_Operations_Physics/SRparameters/)
- Bunker, G. (n.d.). *Synchrotron Radiation Sources and Optics*. Retrieved November 2011, from [acaschool.iit.edu/lectures07/Howard\\_SynchrRad.ppt](http://acaschool.iit.edu/lectures07/Howard_SynchrRad.ppt)
- Cnuddle, V., Cwirzen, A., Masschaele, B., & Jacobs, P. (2009). Porosity and microstructure characterization of building stones and concretes. *Engineering Geology* 103, 76-83.

- Elliot, T. R., & Heck, R. J. (2007). A comparison of optical and X-ray CT technique for void analysis in soil thin section. *Geoderma*, *141*, 60-70.
- HASYLAB. (2009, 02 03). *Photon Science-Storage Rings & Beamlines*. (Helmholtz Association) Retrieved November 1, 2011, from [http://hasylab.desy.de/science/studentsteaching/primers/storage\\_rings\\_\\_beamlines/index\\_eng.html](http://hasylab.desy.de/science/studentsteaching/primers/storage_rings__beamlines/index_eng.html)
- Hsieh, J. (2009). *Computed Tomography: Principles, Design, Artifacts, and Recent Advances - 2nd ed.* Bellingham, WA and Hoboken, NK: Society of Photo-Optical Instrumentation Engineers and John Wiley & Sons, Inc.
- Jenkins, R. (2000). X-ray Techniques: Overview. *Encyclopedia of Analytical Chemistry*, 13269-13288.
- Kaneuji, M. (1978). *Correlation Between Pore Size Distribution and Freeze Thaw Durability of Coarse Aggregate in Concrete*. Joint Highway Research Project Investigation, Purdue University, IN State Highway Commission and USDOT FHWA, West Lafayette.
- Ketcham, R. A., & Carlson, W. D. (2001). Acquisition, optimization and interpretation of X-ray computed tomographic imagery: applications to the geosciences. *Computers & Geosciences*, *27*, 381-400.
- Kim, J., Kwon, N., Chang, S., Kim, K.-T., Lee, D., Kim, S., . . . Rhyu, I. (2011, October 18). Altered branching patterns of Purkinje cells in mouse model for cortical development disorder. *Scientific Reports*, *1*, article # 122.
- Landis, E. N., Zhang, T., Nagy, E. N., Nagy, G., & Franklin, W. R. (2007). Cracking, damage and fracture in four dimensions. *Materials and Structures*, *40*, 357-364.
- Margaritondo, G. (1988). *Introduction to Synchrotron Radiation*. New York: Oxford University Press.
- Oh, W., & Lindquist, W. (1999). Image Thresholding by Indicator Kriging. *IEEE Transactions on Pattern Analysis and Machine Intelligence*, *21*(7), 590-602.
- Peth, S., Horn, R., Beckmann, F., Donath, T., Fischer, J., & Smucker, A. (2008). Three-Dimensional Quantification of Intra-Aggregate Pore-Space Features using Synchrotron-Radiation-Based Microtomography. *Soil Science Society of America Journal*, 897-907.

- Prowell, B. D., Zhang, J., & Brown, E. (2005). *Aggregate Properties and the Performance of Superpave-Designed Hot Mix Asphalt*. Washington D.C.: Transportation Research Board.
- Rivers, M. (2010, February 28). Potential and Limitations of CT as a Technology to Study Properties of Geomaterials. *Power Point Presentation*. New Orleans, LA.
- Roerdink, J., & Meijster, A. (2001). The Watershed Transform: Definitions, Algorithms and Parallelization Strategies. *Fundamenta Informaticae*, 4, 187-228.
- Taina, I. A., Heck, R. J., & Elliot, T. R. (2007). Application of X-ray computed tomography to soil science: A literature review. *Canadian Journal of Soil Science*.
- Titi, H., Tabatabai, H., Ghorbanpoor, A., Lamichhane, K., & Elias, M. (2005). *The Effect of Minnesota Aggregates on Rapid Chloride Permeability Tests*. St. Paul: Minnesota Department of Transportation.
- Williamson, G. S., Weyers, R. E., Mokarem, D. W., & Lane, D. S. (2005, April 14). Investigation of Testing Methods to Determine Long-Term Durability of Wisconsin Natural Aggregate Resources. Blacksburg, Virginia.